

**CHARACTERISTICS OF GRAPHITE FILMS ON  
SILICON- AND CARBON- TERMINATED FACES OF  
SILICON CARBIDE**

A Thesis  
Presented to  
The Academic Faculty

by

Tianbo Li

In Partial Fulfillment  
of the Requirements for the Degree  
Doctor of Philosophy in the  
School of Physics

Georgia Institute of Technology  
December 2006

# CHARACTERISTICS OF GRAPHITE FILMS ON SILICON- AND CARBON- TERMINATED FACES OF SILICON CARBIDE

Approved by:

Dr. Phillip First, Advisor  
School of Physics  
*Georgia Institute of Technology*

Dr. Edward Conrad  
School of Physics  
*Georgia Institute of Technology*

Dr. Walt de Heer  
School of Physics  
*Georgia Institute of Technology*

Dr. Andrew Zangwill  
School of Physics  
*Georgia Institute of Technology*

Dr. Thomas Orlando  
School of Chemistry  
*Georgia Institute of Technology*

Date Approved: October 5 2006

*To my wife and my parents,*

*Haiying Cao, Yuxiang Li and Genmei Xu*

## ACKNOWLEDGEMENTS

I want to express my heartfelt gratitude to my advisor Dr. Phillip First, who offers me not only comprehensive academic guidance and enlightening but consistent regards and supports on every aspect of my growth. It is my great fortune and honor of being his student. I have also learnt serious scientific research attitudes and endless innovation spirits through his leading through example. I would like thank Dr. Edward Conrad for his indispensable collaboration, many insightful discussions and ideas, and warmhearted regards. I would also like to thank Dr. Walt de Heer for his outstanding leadership in navigating this patterned graphite nanoelectronics project and many instructive suggestions to my research. Next, I would thank the rest of my thesis committee members, Dr. Thomas Orlando and Dr. Andrew Zangwill and for thoroughly reading my thesis and giving instructive advices on it. The insightful questions from all the professors made my defense more interesting and very memorable.

I also want to thank all the colleagues working with me on this patterned graphite nanoelectronics project in our STM lab. Dr. Asmerom Y. Ogbazghi led me into this fantastic UHV STM system and gave me direct instructions on how to initial the work. Joanna Hass and Nickil Sharma joined me and helped me to setup and conduct many experiments. Their efforts significantly make the work much more effective and infinitely more fun. Dr. Jianfei Shao and Dr. Sameh Dardona shared a lot of experience on the low temperature STM system in our lab, which is very helpful for enriching my undertaking on the STM system. Greg Rutter obtained very exciting results from NIST, which supports many results in my thesis and upgrade our understanding on graphite films to a higher level. His effort of ordering our lab really made our work more effective and enjoyable. I also appreciate helps from the Kevin Kubista, William Knouse, David Miller, who joined our lab recently and worked very hard the graphite project.

The supports from our collaborated labs are extremely important for my thesis work. It



is not enough no matter how I express my gratitude. Hydrogen etching SiC and graphitizing SiC in RF furnace are the two most important techniques of preparing samples for my experiments. Xuebin Li contributed most on developing these two methods and supported most samples for my experiments. Dr. Zhimin Song gave me lots of helps on analyzing samples and preparing patterned sample with the E-beam lithography process. Berger Claire conducted many important experiments on transport properties measurement, which yielded important results and upgraded my understanding of the whole graphite/SiC system. Dr. Rui Feng shared many X-ray results and much constructive discussions. Kristin Shepperd cooperated desirably with me on the SiC/Si project. Dr. Xiaosong Wu, Nathaniel Brown, Michael Sprinkle also gave me assistance on AFM experiments and sample preparations.

I highly appreciate the help and support from all the colleagues working with me during this five-year PhD program. Every episode we share together will be kept in my mind as sweetest memories.

Finally, I also want to thank my whole family for always standing with me and sharing every challenging moment.

# TABLE OF CONTENTS

<b>DEDICATION</b> . . . . .	<b>iii</b>
<b>ACKNOWLEDGEMENTS</b> . . . . .	<b>iv</b>
<b>LIST OF TABLES</b> . . . . .	<b>ix</b>
<b>LIST OF FIGURES</b> . . . . .	<b>x</b>
<b>SUMMARY</b> . . . . .	<b>xix</b>
<b>I INTRODUCTION</b> . . . . .	<b>1</b>
1.1 Patterned Graphite Nanoelectronics . . . . .	1
1.2 Silicon Carbide . . . . .	2
1.2.1 Physical Properties of SiC . . . . .	2
1.2.2 CVD Growth of SiC Wafer . . . . .	4
1.2.3 Electronics Application of SiC . . . . .	5
1.3 Graphite Films and Graphene . . . . .	6
1.3.1 Quantum Hall Effect and Landau Levels . . . . .	9
1.3.2 Graphite Films/SiC system . . . . .	11
1.4 Work in This Thesis . . . . .	13
<b>II EXPERIMENTAL APPARATUS AND TECHNIQUES</b> . . . . .	<b>14</b>
2.1 Low Energy Electron Diffraction . . . . .	14
2.1.1 Four-grid LEED System . . . . .	14
2.1.2 LEED Pattern Interpretation . . . . .	16
2.2 Auger Electron Spectroscopy: Single-pass CMA . . . . .	18
2.2.1 Auger Process . . . . .	18
2.2.2 Modulation Technique for Auger Spectra . . . . .	18
2.3 Scanning Tunneling Microscopy Techniques and Equipments . . . . .	22
2.3.1 STM Techniques . . . . .	22
2.3.2 Room Temperature STM . . . . .	24
2.3.3 Low Temperature STM . . . . .	25
2.3.4 Tip Preparation . . . . .	26

<b>III CHARACTERISTICS OF GRAPHITE FILMS ON SiC (0001) SURFACE . . . . .</b>	<b>27</b>
3.1 Sample Preparation . . . . .	27
3.1.1 Hydrogen Etching and Chemical Vapor Deposition Growth . . . . .	27
3.2 Graphitization Process . . . . .	30
3.2.1 SiC $\sqrt{3}\times\sqrt{3}$ R30° and $3\times 3$ Reconstruction . . . . .	32
3.2.2 SiC $6\sqrt{3}\times 6\sqrt{3}$ R30° and the Conventional Explanations . . . . .	33
3.3 Graphite Thickness Estimation with Auger Peak-To-Peak Ratio . . . . .	35
3.3.1 Auger Attenuation Model . . . . .	35
3.3.2 Auger Peak-to-peak Ratio Calculation . . . . .	36
3.4 On-axis SiC Samples . . . . .	41
3.4.1 LEED Results and Discussion . . . . .	41
3.4.2 STM Results and Discussion . . . . .	44
3.5 Interpretation of LEED Patterns and STM Images . . . . .	55
3.5.1 SiC, Graphite & Double Scattering Spots . . . . .	55
3.5.2 $6\sqrt{3}\times 6\sqrt{3}$ R30° Reconstruction Layer . . . . .	56
3.5.3 Satellite Spots . . . . .	62
<b>IV CHARACTERISTICS OF GRAPHITE RIBBONS ON SiC (0001) SURFACE . . . . .</b>	<b>64</b>
4.1 Vicinal Cut SiC Samples . . . . .	64
4.2 Patterned Samples & Graphite Ribbons . . . . .	66
4.2.1 E-beam Lithography Process for Graphite/SiC(0001) . . . . .	66
4.2.2 STM on the Patterned Sample . . . . .	67
<b>V CHARACTERISTICS OF GRAPHENE FILMS ON SiC C-FACE . . . . .</b>	<b>71</b>
5.1 Sample Preparation . . . . .	72
5.2 LEED Results . . . . .	72
5.3 STM Results . . . . .	75
5.3.1 On Thick Graphite Films . . . . .	75
5.3.2 On Thin Graphite Films . . . . .	79
<b>VI CONCLUSION . . . . .</b>	<b>83</b>
6.1 Summary of Results . . . . .	83

6.2 Suggested Future Work . . . . .	85
<b>REFERENCES . . . . .</b>	<b>86</b>
<b>VITA . . . . .</b>	<b>93</b>

# LIST OF TABLES

3.1	Mean free paths of electrons at different layers. . . . .	36
-----	---	----

# LIST OF FIGURES

- 1.1 The crystal structure of commonly used SiC polytypes. The stacking sequence of Si-C bilayers along the c-axis (0001) determine the properties of each SiC polytype. (a) In SiC, each Si atom is bonded tetrahedrally with four C atoms and each C atom is also bonded tetrahedrally with four silicon atoms. Each bilayer plane is perpendicular to the [0001] direction. Six bilayers of each polytype are plotted: (b) 3C-SiC has ABC stacking sequence as common fcc structure. (c) 4H-SiC has ABCB stacking sequence with hexagonal structure, , which is displayed parallel to SiC  $\{11\bar{2}0\}$  plane. (d) 6H-SiC(hexagonal) has ABCACB stacking sequence with structure. This figure is after Ref. [1]. . . . . 3
- 1.2 Four possible bulk-terminated surface layer stacking sequences on 4H-SiC (0001). S1 and S2 are different configurations according to different orientated bilayers. S1\* and S2\* have the same configuration as S1 and S2 respectively, after a  $60^\circ$  rotation along [0001] axis. This figure is after Ref. [2]. 4
- 1.3 The crystal structure of graphite **ABAB** (Bernal Structure) and its Brillouin zone. (a) The primitive unit cell with dimensions  $a = 2.46 \text{ \AA}$  and  $c = 6.71 \text{ \AA}$ . The bonding in plane length is  $1.42 \text{ \AA}$ . There are four atoms per unit cell, labeled as  $A$ ,  $A'$ ,  $B$  and  $B'$ . The difference between  $A$  atoms and  $B$  atoms lies in that  $A$  atoms (solid circles) have neighbors directly above and below in the adjacent layer planes but  $B$  atoms (hollow circles) do not have such neighbors in adjacent planes. (b) The Brillouin zone of graphite. The electron and hole Fermi surfaces are located in the vicinity of the edges HKH and H'K'H', where  $KH = \frac{\pi}{c}$ . . . . . 8
- 1.4 Representations of graphene in real space and momentum space. (a) Graphene's honeycomb lattice. Each carbon atom (black solid ball) has three covalent  $\sigma$ -bond electrons bonding tightly with three other carbon atoms in plane and one  $\pi$ -bond electron having high mobility.  $\pi$ -bond electrons wander across the plane and forming 2D electron gas. Hydrogen atoms (representing with the small blue balls) are often used to passivate the dangling bonds hanging on the edge of graphene. This figure is after Ref. [3]. (b) Band structure of the graphene film. The energy-momentum dispersion is linear,  $E = \hbar k|v_F|$  near the Dirac points representing as the vertices of the blue hexagon. . . . 10
- 1.5 Quantum Hall Effect in graphene. The green line is the longitudinal resistivity  $\rho_{xx}$  of the graphene 2D electron gas in high magnetic field.  $\rho_{xx}$  goes to zero at the values where the transverse conductivity  $\sigma_{xy}$  is quantized in units of  $e^2/h$ . The factor 4 is due to the spin and band-structure degeneracy in graphene. The inset plot shows that the 1/2-integer phase shift disappears and the band symmetry changed when one of the systems has more than one graphene sheet. This figure is after Ref. [4]. . . . . 12

2.1	A picture of the room temperature, ultra high vacuum scanning tunneling microscopy system. The chamber includes capabilities for scanning tunneling microscopy, low-energy electron diffraction, Auger electron spectroscopy, ion beam sputtering, a field ion/field emission microscope, metal deposition, residual gas analysis, and a load-lock for tip/sample exchange. . . . .	15
2.2	The diagram of the four-grid reverse view LEED system optics. This figure is from the manual of the LEED system [5]. . . . .	16
2.3	(a) 2D LEED diffraction interpreted with Ewald sphere. Surface diffraction rods (01), (02), and ... are normal to the 2D crystalline plane and intercepted by the Ewald sphere at the constructive diffraction spots. (b) Diffraction beams and LEED spots in real LEED system. The blue triangles in two figures are analogous, which determines a direct mapping from the diffraction spots on camera photos and reciprocal lattices through a simple formalism. . . . .	17
2.4	(a) A schematic drawing of the KLL Auger process. (b) Universal curve of the inelastic mean free path vs. electron energy. The solid line is the theory result. This figure is after Ref. [6, 7]. . . . .	19
2.5	Modulations techniques used for AES analysis. (a) Electron and current distribution of signals are the same in CMA method ( $I(E) \propto E \cdot N(E)$ ). (b) Adding modulation to the Auger electrons distribution $N(E)$ . (c) The first derivative of current distribution gives the AES spectrum. This figure is after Ref.[8]. . . . .	20
2.6	A schematic diagram of the single pass cylindrical mirror analyzer. This figure is after Ref. [8]. . . . .	21
2.7	A schematic diagram of STM tunneling. . . . .	22
3.1	SiC surface preparation before growing graphite films. (a) AFM image on 6H-SiC Si-face of an as-received sample, full of scratches and defects. (b) After $H_2$ etching at $1500^\circ\text{C}$ for 30 minutes in the home built RF furnace, the surface on SiC (0001) or (000 $\bar{1}$ ) face becomes atomic flat with ordered terraces and step of one unit cell height ( $1.5\text{ nm}$ for 6H-SiC and for $1.0\text{ nm}$ for 4H-SiC). (c) NASA samples have been further processed with CVD growth to remove terraces and develop atomically flat surfaces on some mesas. The mesas on the surface are used to prevent the spread of intrinsic screw dislocations in SiC substrates. The image size is in $1\text{ mm} \times 1\text{ mm}$ . (d) Profile of on terraces in Fig. (b) shows the height between terrace is half the unit cell of 6H-SiC. . . . .	28
3.2	The LEED patterns on SiC (0001) surface after $H_2$ etching before any further treatment in the UHV chamber. (a) SiC $\sqrt{3} \times \sqrt{3}$ R $30^\circ$ reconstruction is always the dominant feature of $H_2$ etched samples. A diffuse ring around the third order $\sqrt{3} \times \sqrt{3}$ R $30^\circ$ spots are visible at this E-beam energy, $E_p=169\text{eV}$ . (b) Three fold symmetry $\sqrt{3} \times \sqrt{3}$ R $30^\circ$ LEED pattern, which is the evidence of uniform termination on SiC surface after $H_2$ etching, $E_p=197\text{eV}$ . . . . .	29

3.3	The schematic drawing of the SiC sample mounting. The sample holder is made of molybdenum. The hole in the center of the sample holder is drilled for E-beam bombardment heating. The SiC sample (red rectangle) is mounted over two tantalum sheets as a bridge. Another two tantalum sheets are spot-welded on top pinching tightly on the two diagonal corners of the sample. . . . .	31
3.4	Top and side views Si adatom model of the $\sqrt{3}\times\sqrt{3}$ R30° reconstruction for $T_4$ and $H_3$ positions. This figure is after Ref. [9]. . . . .	33
3.5	The schematic drawing of the Auger attenuation model on graphitized SiC(0001) surface. The atom number on each layer is drawn to be proportional to real number of atoms on each layer. The reconstruction layer can be all carbon or silicon atoms, or a mixture of them. The sum of the attenuation factors of Si and C are calculated with the Matlab code. The attenuation induced by both incident E-beam and outgoing Auger electron beam is considered. The incident beam is normal to the surface and the CMA Auger electron collecting angle is 42.2° from the normal of the surface, therefore an extra angle factor $\cos(42.2^\circ)$ is considered for the IMFP in Tab. 3.1. . . . .	37
3.6	Graphite film thickness estimation and Auger evolution of annealing SiC(0001) in UHV. The solid line represents the estimation with the model that one layer carbon $6\sqrt{3}\times 6\sqrt{3}$ R30° atoms exist between graphite films and the Si-face of SiC (note: the attenuation of the $6\sqrt{3}\times 6\sqrt{3}$ R30° layer is the same to a $\sqrt{3}\times\sqrt{3}$ R30° layer). The dash line represents the estimation with the model that the graphite films are grown directly on the Si-face of SiC, i.e. no reconstruction layer between the top layer of SiC and the bottom layer of graphite. The dotted line represents the estimation with the model that one layer silicon $6\sqrt{3}\times 6\sqrt{3}$ R30° atoms exist between graphite films and the Si-face of SiC. The solid line represents the estimation with the model that one layer carbon $6\sqrt{3}\times 6\sqrt{3}$ R30° atoms exist between graphite films and the Si-face of SiC. The inset figure show Auger curves corresponding to different SiC(0001) surface reconstructions when annealing SiC in UHV. (a) SiC(0001) surface after $H_2$ etching. (b) SiC(0001) surface annealed up to 1150° C with SiC $\sqrt{3}\times\sqrt{3}$ R30° reconstruction on surface. (c) Graphitized SiC(0001) surface annealed up to 1350° C with SiC $6\sqrt{3}\times 6\sqrt{3}$ R30° reconstruction on surface. . . . .	40
3.7	The evolution of the LEED patterns on SiC(0001) surface. (a) SiC $\sqrt{3}\times\sqrt{3}$ R30° $E_p=180\text{ eV}$ . The first phase acquired after annealing in UHV above 1100 ° C. (b) Monolayer graphite on SiC(0001), $6\sqrt{3}\times 6\sqrt{3}$ R30°, $E_p=49\text{ eV}$ . The $\sqrt{3}\times\sqrt{3}$ R30° spots are labeled with R3 in the figure and coexist with the $6\sqrt{3}\times 6\sqrt{3}$ R30° spots at this phase. (c) Monolayer graphite on SiC(0001), $6\sqrt{3}\times 6\sqrt{3}$ R30°, $E_p=109\text{ eV}$ . The diffraction spots show that the graphene sheets register epitaxially with the underlying SiC(0001) surface and have 30° rotation. (d) Thick graphite on SiC(0001), graphite $1\times 1$ . Graphite spots with their satellites are observable. SiC spots are very weak. $E_p=78\text{ eV}$ . . . . .	42
3.8	Expanded view of the lower-left corner of Fig. 3.7d. Arrow A points to the graphite diffraction spot and arrow B points at a $\sqrt{3}\times\sqrt{3}$ R30° spot. The fine diffraction pattern around the 4th-order $\sqrt{3}\times\sqrt{3}$ R30° is visible. . . . .	43



- 3.9 The SiC  $6\sqrt{3}\times 6\sqrt{3}$  R30° reconstruction LEED patterns of monolayer graphene growth on the SiC(0001) surface. At this phase, the LEED pattern exhibits maximum number diffraction spots, which was traditionally regarded as the consequence of double scattering. However our results show that it is more related to a  $6\sqrt{3}\times 6\sqrt{3}$  R30° reconstruction layer between graphite and SiC. Additionally,  $\sqrt{3}\times\sqrt{3}$  R30° spots are already extinguished, which is a sign we often assume as the beginning of the initial graphene layer growth. (a) The pattern around  $\sqrt{3}\times\sqrt{3}$  R30° {01} diffraction spots. Graphite diffraction spots are out of LEED phosphor scree at this E-beam energy. Three red arrows point at 3 “A3” spots, which are obvious much brighter than other non-primary SiC spots,  $E_p=41\text{ eV}$ . (b) A higher energy photo for the pattern around SiC {01} and graphite {01}. A spot outside SiC almost has the equivalent intensity of SiC spots. The origin of this spot is not clear and we tend to think it is a also  $6\sqrt{3}\times 6\sqrt{3}$  R30° structure factor effect,  $E_p=95\text{ eV}$ . (c) Higher order diffraction spots, many of which can be reproduced by the kinematic scattering model,  $E_p=212\text{ eV}$ . (d) LEED pattern around (00) spots obtained by titled sample 12°,  $E_p=49\text{ eV}$ . . . . . 45
- 3.10 The SiC  $6\times 6$  Moiré pattern formed by putting one layer of graphene atoms (in red) on one layer of SiC atoms (in blue). The axis units are angstroms. The periodicity follows SiC  $6\sqrt{3}\times 6\sqrt{3}$  R30° reconstruction due to the geometric relationship between the lattice constants of SiC and graphite that  $6\sqrt{3}a_{\text{SiC}} = 13a_{\text{Graphite}}$ . The unit cell of graphite rotates 30° relatively to the SiC substrate unit cell. The  $6\sqrt{3}\times 6\sqrt{3}$  R30° unit cell is depicted as the big black rhombus and the SiC unitcell is presented by the small black rhombus. . . . . 47
- 3.11 A STM image and its STS spectra of more than three graphene layers on SiC(0001) surface of a NASA sample. (a) STM image of a surface region of the graphitized SiC(0001) surface. Three domains in the figure all show SiC  $6\times 6$  corrugation. The tip voltages was  $-0.6\text{ V}$ . The constant tunneling current was  $100\text{ pA}$  (b) dI/dV spectra (log scale) acquired from upper and lower regions marked with corresponding color line in the image at top. The black line is an average of 396 spectra at different positions, the red line an average of 105. With a few “glitchy” exceptions, individual spectra in each region showed negligible variation from the average dI/dV shown. Inset: Atomically resolved region (different sample, similar preparation). (c) dI/dV spectra comparatione between the upper region and its boundary. Almost overlapping curves indicate that the graphite is continuous over the domain boundaries. . . . . 48
- 3.12 STM images of some graphitized area on the same NASA sample show vacancy defects of  $6\times 6$  structure. It is still not clear whether graphite films on these defects are completed or not. The tip voltages of both figures were  $-2.0\text{ V}$ . The constant tunneling current was  $200\text{ pA}$ . . . . . 50

3.13	STM images of monolayer graphene on SiC(0001). The tip voltage were $-1.0\text{ V}$ for the top image and $-0.8\text{ V}$ for the bottom image. The constant tunneling current for both scanning was $100\text{ pA}$ . The $6 \times 6$ corrugation is clear in the bottom figure. Disordered domains, which might be related to the growth of new graphite layer, are also visible in both figures. . . . .	51
3.14	Fourier analysis on a STM image of monolayer graphene on SiC(0001)surface. The STM image and the inverse Fourier transform is on the top and the corresponding Fourier transforms on the bottom (a) The original STM image obtained from the center $6 \times 6$ ordered region of Fig. 3.13b. The tip voltage was $-0.8\text{ V}$ and the constant tunneling current was $100\text{ pA}$ . (b) Inverse Fourier transform with selecting the region around $\sqrt{3} \times \sqrt{3}\text{ R}30^\circ$ spots and the region around $6 \times 6$ spots the Fourier transform spectrum of the STM image. . . .	52
3.15	STM images of monolayer graphene film on SiC(0001) with different tip bias taken simultaneously. The sample was annealed in UHV at $1250^\circ\text{ C}$ for 3 mins. (a) Fill states image. The tip voltage was $0.6\text{ V}$ . (b) Empty state image. The tip bias is $-0.6\text{ V}$ . The constant tunneling current was both $100\text{ pA}$ . (c) Fourier filtered image of the negative bias STM image by selecting the mask used in (f). (d) Fourier filtered image of the negative bias STM image by selecting the complementary mask of (f). (e) Fourier transform of the original STM image. (f) Fourier transform with a Fourier filter to suppress the spectrum not related to the feature LEED pattern. . . . .	53
3.16	A STM image and its STS spectra of of monolayer graphene on the SiC(0001) surface. (a) STM image of a surface region of the graphitized SiC(0001) surface, which is also from the center part of Fig. 3.13b. Two major domains are clear on this image. The higher domain is a disordered region, which could be the initial growth layer of the next graphene film, since the height between the two terrace is about $3.3\text{ \AA}$ , about the distance between two adjacent graphite layers. the lower domain on the right is the ordered $6\sqrt{3} \times 6\sqrt{3}\text{ R}30^\circ$ region. (b) $dI/dV$ spectra (log scale) acquired from disordered and ordered regions marked with corresponding color line in the image at top. Individual spectra in each region showed negligible variation from the average $dI/dV$ shown. On the right ordered region, the $dI/dV$ spectrum (black solid line) indicates a zero-gap semiconductor feature spectrum, which is from a graphene layer on top of the $6\sqrt{3} \times 6\sqrt{3}\text{ R}30^\circ$ interface layer. On the left disordered terrace, the $dI/dV$ spectrum (red solid line) also displays a zero-gap semiconductor feature spectrum but with a $30\text{ meV}$ around shift to the filled state energies. The bump at the $-0.2\text{ V}$ sample bias probably indicates some dangling bond states in the disordered region. . . . .	54
3.17	Schematic plot of the LEED pattern that thin graphite growth on the SiC(0001) surface. Diffraction spots are categorized according to their sources. The sizes of the spots are drawn according to their LEED intensities. . . . .	57

3.18	Simulation with kinematical scattering LEED pattern of SiC(0001) surface on a plane grid. The incident electron beam energy is set to be 60 eV. (a) one $6\sqrt{3} \times 6\sqrt{3} R30^\circ$ unit cell cut from the Fourier-filtered STM image of Fig. 3.14b (white dashed line). (b) Schematic drawing of one unit cell of the $6\sqrt{3} \times 6\sqrt{3} R30^\circ$ layer (grey shaded circles) sitting on SiC $1 \times 1$ substrate (filled black circle) used in the simulation. (c) Simulated LEED pattern from the $6\sqrt{3} \times 6\sqrt{3} R30^\circ$ reconstruction. (d) Simulated LEED pattern of four layers of graphene with 0.08 Å surface corrugation. . . . .	59
3.19	Schematic plot of the three SiC $\sqrt{3} \times \sqrt{3} R30^\circ$ reconstruction sublattices in one SiC $6\sqrt{3} \times 6\sqrt{3} R30^\circ$ unit cell. The three sublattices are plotted with three different colors: blue, red and green. Superposing these 3 sublattices yields a SiC $1 \times 1$ lattice. . . . .	60
4.1	STM images on graphitized 3.5° vicinal SiC(0001) surface. (a) The large scale STM image shows the terraces on graphitized surface. Step edges run along $[11\bar{2}0]$ on average. Two pieces of peeled off graphite flakes are visible on the surface. The tip voltage was $-1.0 V$ and the constant tunneling current was 100 pA. (b) Typical graphitized surface with $6 \times 6$ corrugation are visible on each terrace. A three bilayer step is also resolved. The tip voltage was $-1.0 V$ and the constant tunneling current was 100 pA. (c). A schematic drawing of the ideal graphite ribbons growth on each terraces with parallel ribbon edge running along $[11\bar{2}0]$ direction. (d) The profile of terraces shows the the step height between two adjacent major terraces is 0.75 nm, which is the height of three Si-C bilayer. . . . .	65
4.2	Schematic flow of the E-beam lithography process for fabricating graphene ribbons. . . . .	67
4.3	Patterned graphite ribbons after E-beam lithography process. (a) Optical microscopy image. The photo was taken under 150 times amplification mode. (b) AFM image before removing HSQ resist. (c) SEM image before removing HSQ resist. The AFM result indicate that the height between the HSQ surface (high region) and SiC surface (low region) is around 10 nm. (d) STM image after removing HSQ resist with HF solvent. The tip voltage was $-4.0 V$ and the constant tunneling current was 100 pA. The image was taken under big scan mode. The profile on the surface show that the height between graphite (higher region) and SiC (lower region) is around 20 nm. This is obviously against the result from AFM measurement when HSQ exist. This abnormal STM height different is due to the HSQ residue on graphene ribbon region. . . . .	69

- 4.4 STM images over patterned graphite ribbons after E-beam lithography process. The surface was subsequently heated to  $500^{\circ}\text{C}$  in the UHV chamber. (a) STM over both graphite and SiC regions. The higher region is graphite ribbon region and the lower region is the SiC region with graphite removal in the lithography process. “Nanocaps” from HSQ resist cover much of the surface. The tip voltage was  $-4.0\text{ V}$  and the constant tunneling current was  $100\text{ pA}$ . (b) A flat region not covered by HSQ shows SiC  $6\times 6$  corrugation. The tip voltage was  $-0.9\text{ V}$  and the constant tunneling current was  $1\text{ nA}$ . (c) Atomic resolution STM image on the center flat region of (b). SiC  $6\sqrt{3}\times 6\sqrt{3}\text{ R}30^{\circ}$  interfacial layer is resolved. The tip voltage was  $-0.5\text{ V}$  and the constant tunneling current was  $1\text{ nA}$ . (d) Another flat region show terraces remaining  $\text{H}_2$  etching features. The height between adjacent terraces are the SiC bilayer height or 6H-SiC half unit cell height. The tip voltage was  $-2.5\text{ V}$  and the constant tunneling current was  $100\text{ pA}$ . (e) SiC  $6\times 6$  corrugation obtained on the flat region in (d). The tip voltage was  $-0.4\text{ V}$  and the constant tunneling current was  $100\text{ pA}$ . (f) The profile along the red line in (d). . . . . 70
- 5.1 The evolution of the LEED patterns on SiC(000 $\bar{1}$ ) surface. (a) The LEED pattern after  $\text{H}_2$  etching shows SiC  $\sqrt{3}\times\sqrt{3}\text{ R}30^{\circ}$  reconstruction,  $E_p=118\text{ eV}$ . Some LEED patterns before graphitization also show 3-fold symmetry and diffuse background on C-face. Charge effects are observed, when the electron beam energy is below a threshold value of  $110\text{ eV}$ . (b) 1 to 2 graphene layers on SiC(000 $\bar{1}$ ) surface. Both graphite arcs and SiC  $\sqrt{3}\times\sqrt{3}\text{ R}30^{\circ}$  reconstruction spots are visible,  $E_p=73\text{ eV}$ . Graphite arcs indicate that the initial growth of graphite is azimuthally disordered. (c) 3 to 4 layers of graphene on SiC(000 $\bar{1}$ ) surface. Only graphite rings with stronger intensity and SiC  $1\times 1$  spots are visible,  $E_p=103\text{ eV}$ . (d) Thicker graphite films with more than 6 layers on SiC(000 $\bar{1}$ ) surface. Only graphite rings visible at this phase. The graphite ring is continuous but not uniform intensity. Bright arcs appears at certain azimuths along the graphite ring,  $E_p=69\text{ eV}$ . . . . . 74
- 5.2 AFM images on graphite films growth on the C-face of SiC prepared in the RF furnace by Xuebin Li. (a) AFM on thick graphite films growth on SiC C-face. The surface has big domains in several micron size. The height between big domains vary from  $2\text{ nm}$  to  $5\text{ nm}$ . Big nanotubes are across the surface. (b) AFM on  $\text{H}_2$  etched surface the C-face of SiC. The height between adjacent terraces is around one unit cell height of 4H-SiC. The surface maintain the terraces after a thin graphite film growth process. . . . . 76

- 5.3 STM images on thick graphite films grown on the C-face of SiC. (a)  $4\mu\text{m}$  scan presents an overview on the surface showing domains of micron size. Large nanotubes cross the surface often forming the boundaries between domains. The tip voltage was  $-2.5\text{ V}$  and the constant tunneling current was  $100\text{ pA}$ . (b) Nanocaps and flat areas between nanocaps on a flat domain. The nanocaps coverage is less than 40%. The profile over the lowest part of the nanocaps show that they sit on graphene islands over the uniform flat graphite films underneath. The tip voltage was  $-3.0\text{ V}$  and the constant tunneling current was  $100\text{ pA}$ . (c) Profile over several domains (dashed line in (a)). (d) Profile across the lowest region of nanocaps show that the height is about one layer of graphene, which means nanocaps probably grow on graphene islands beneath nanocaps. . . . . 77
- 5.4 High resolution TEM cross-sectional on C-face graphitized 4H-SiC. Along the (0001) direction, the periodicities of  $1\text{ nm}$  unit cell and  $0.25\text{ nm}$  SiC bilayers are both discerned within the 4H-SiC. The graphite films in this picture have uniform thickness of around 20 sheets. However, the thickness is not uniform on the same sample, varying from 5 to 25 monolayers. The gap between the SiC substrate and graphite films is probably due to peeling during sample wafering, since the gap changes in different TEM scans. This figure is after Ref. [10] . . . . . 78
- 5.5 The flat region on SiC C-face surface is terminated with graphite films. (a) The STM image on a flat region with nanocaps on surface. The tip voltage was  $-3.0\text{ V}$  and the constant tunneling current was  $100\text{ pA}$ . (b) Atomic resolution scanning within the dashed square of the flat region. Graphite with honeycomb structure is discerned. The tip voltage was  $-1.6\text{ V}$  and the constant tunneling current was  $100\text{ pA}$ . The graphite films in one domain show ordered crystal structure, which means the azimuthal disorder seen in LEED should come from different domains or different graphite layers. (c) Profile on graphene films shows surface corrugation is only 15-20 picometers. 79
- 5.6 STM images on thin graphite films grown on SiC C-face. (a) An overview of the surface shows that after the thin film graphitization process, the surface maintains the oriented terraces forming in the  $H_2$  etching process. Big nanotubes also appear on the surface, but the number density of nanotubes is much smaller than the thicker films. The tip voltage was  $-4.0\text{ V}$  and the constant tunneling current was  $50\text{ pA}$ . (b) The surface is also covered by nanocap islands. The nanocap coverage is nearly the same to the thick graphitized surface. The tip voltage was  $-4.5\text{ V}$  and the constant tunneling current was  $100\text{ pA}$ . (c) Profile from (a) shows that the terrace height is  $1\text{ nm}$  or  $2\text{ nm}$ . (d) Profile from (b) indicate that the height of nanocaps is around  $1-1.5\text{ nm}$  and the terrace height is  $1\text{ nm}$ . . . . . 81

- 5.7 STM image and its profile on the thin graphite film grown on the C-face of SiC. (a) STM scan on the flat region between the nanocaps. The structure is either a disordered structure underneath graphite film or the corrugation of graphite film itself. The tip voltage was  $-2.5\text{ V}$  and the constant tunneling current was  $50\text{ pA}$ . (b) The profile shows that the surface vertical undulation is within half an angstrom and the lateral spacing is from  $2\text{ nm}$  to  $5\text{ nm}$ . . 82

## SUMMARY

Ultrathin graphite films grown on silicon carbide (SiC) form a promising platform for ballistic-carrier devices based on nano-patterned epitaxial graphene [11]. Graphite films with thickness from 1 – 30 atomic layers are grown on the Si-terminated (0001) face and C-terminated ( $000\bar{1}$ ) face of 6H-SiC and 4H-SiC via thermal desorption of silicon in an ultrahigh vacuum (UHV) chamber or in a high-vacuum RF furnace. The growth of graphite films is investigated with low energy electron diffraction (LEED), Auger electron spectroscopy (AES), and scanning tunneling microscopy (STM). Graphite LEED patterns and atom-resolved STM images on graphite films prove that epitaxial growth is achieved on both faces of the SiC substrate. The thickness of graphite films is estimated with two methods, modeling the Si:C Auger peak to peak intensities with simplified assumptions and curve-fitting of synchrotron X-ray diffraction peaks.

Through LEED and STM investigations of monolayer graphite grown on the Si-face of 6H-SiC(0001), we show the existence of a SiC  $6\sqrt{3}\times 6\sqrt{3}$  R30° reconstructed layer between graphite films and the SiC substrate. The graphite films prepared on the Si-face have less than 0.2 Å vertical amplitude corrugation following a SiC  $6\times 6$  periodicity. We prove that this assumption is related to the SiC  $6\sqrt{3}\times 6\sqrt{3}$  R30° reconstruction layer. We also prove that the kinematic scattering from the SiC  $6\sqrt{3}\times 6\sqrt{3}$  R30° interfacial structure gives a good interpretation of the complicated  $6\sqrt{3}\times 6\sqrt{3}$  R30° LEED diffraction patterns, which traditionally are regarded as the result of double-scattering from the graphite film and SiC substrate. The graphitized surfaces show structurally coherent 50 nm<sup>2</sup> domains with surface height difference between adjacent domains in the same terrace varying from 0.5 Å to 3.0 Å. The minimum corresponds to the Si-C vertical separation within one SiC bilayer and the maximum to the graphite interlayer spacing. Further scanning tunneling spectroscopy (STS) measurements and low temperature STM show that the graphite films remain continuous over the steps between domains.

Ultrathin graphite films grown on the C-face of 6H-SiC(000 $\bar{1}$ ) in the UHV chamber or in the RF furnace are also investigated. Some areas of the surface prepared in RF furnace are covered by nanocaps or nanotubes, and the remaining areas are flat graphite films. The huge nanotube-like bumps often form common boundaries of the domains. The graphitized C-face surface generally has larger size domains and terraces than Si-face according to AFM and X-ray experiments. LEED patterns from the thinnest C-face films show epitaxial growth on the SiC substrate, however split diffraction arcs in the LEED pattern from thicker films indicate azimuthal disorder.



# CHAPTER I

## INTRODUCTION

### *1.1 Patterned Graphite Nanoelectronics*

The semiconductor industry always needs smaller, faster, and more efficient electronic devices. Scientists and engineers work on both scaling down the state-of-the-art CMOS technology and searching for new materials for narrower and thinner circuit lines. Since metals are thermodynamically unstable when metallic films are scaled down to nanometer thickness, sooner or later, novel nonmetal materials will inevitably occur on the roadmap of physical properties. The project, Patterned Graphite Nanoelectronics, investigates and explores potential device applications of a new material system: ultrathin epitaxial graphite films grown on silicon carbide substrates.

Organic conductors made of Bechgaard salts and carbon nanotubes are two recent notable technologies for nanoelectronics application. Carbon nanotubes have very high carrier mobility and stable structure, which are promising for high speed devices. Carbon nanotubes can be either metallic or semiconducting and resist mechanical and chemical degradation. Carbon nanotube field-effect transistors (FETs) already have been demonstrated and operated at room temperature [12, 13]. However, carbon nanotube's complicated 3D geometry and unruly growth inhibit its development for high volume device production in the semiconductor industry. Graphite films, the monolayer of which is called graphene, were thought to be nonexistent in the free state but have been discovered recently [11, 14, 15]. Graphite ribbons have been proven to have similar electronic properties to carbon nanotubes with both semiconducting and metallic properties depending on the crystallographic direction of the graphite ribbon axis [16, 17]. Graphite ribbons have much higher potential for circuit fabrication through typical microelectronic technologies, since graphene has planar structure.

Two methods of fabricating ultrathin graphite films, graphene, or few-layer graphene,

have been developed. One way is to micromechanically cleave graphite films from highly oriented pyrolytic graphite(HOPG) [14, 15], and the other is to grow graphite films on silicon-terminated or carbon-terminated surfaces of silicon carbide substrates [11]. A thorough description of the micromechanical method can be found in the works of Novoselov, et al. and Zhang, et al. [14, 15]. The latter method, growth of ultrathin epitaxial graphite films on single-crystal silicon carbide, is promising for fabricating large scale circuits [11]. The transport properties of graphite ribbons are closely related to those of carbon nanotubes and reveal the Dirac nature of the charge carriers [4, 18]. Magnetotransport measurements of patterned structures reveal remarkable quantum confinement effects showing that graphene ribbons act as electron waveguides. The phase coherence length exceeds one micrometer at 4K and mobilities can be over  $2.5 \text{ m}^2/\text{V} \cdot \text{s}$  [19]. All graphene electronically coherent devices and device architectures are envisaged.

## ***1.2 Silicon Carbide***

The reason silicon carbide (SiC) was selected as the platform for growing ultra thin graphite films is its unique properties. Under certain high temperature and high vacuum conditions, SiC evaporates Si atoms on its surfaces and the remaining carbon atoms naturally form ultrathin graphite films on the surface. On the other hand, as one of the most interesting wide band gap semiconductors, the physical and chemical properties of SiC have been widely investigated for over 100 years. Its special fabrication process and numerous applications are among the top research interests of scientists and engineers.

### **1.2.1 Physical Properties of SiC**

Silicon carbide has more than 170 polytypes, however only a few of them are useful for reliable semiconductor electronic devices. Each SiC polytype, consisting of half silicon atoms and half carbon atoms, has its own distinct electronic and optical properties due to the unique stacking sequences of Si-C bilayers. All polytypes have a hexagonal frame of SiC bilayers [20]. In each bilayer, the distance between the carbon and silicon atom is  $1.89 \text{ \AA}$ , and the distance between the closest carbon atoms is  $3.08 \text{ \AA}$  [20, 21]. The distance between two bilayers is  $2.52 \text{ \AA}$ . The most common polytypes of SiC being developed for electronics are

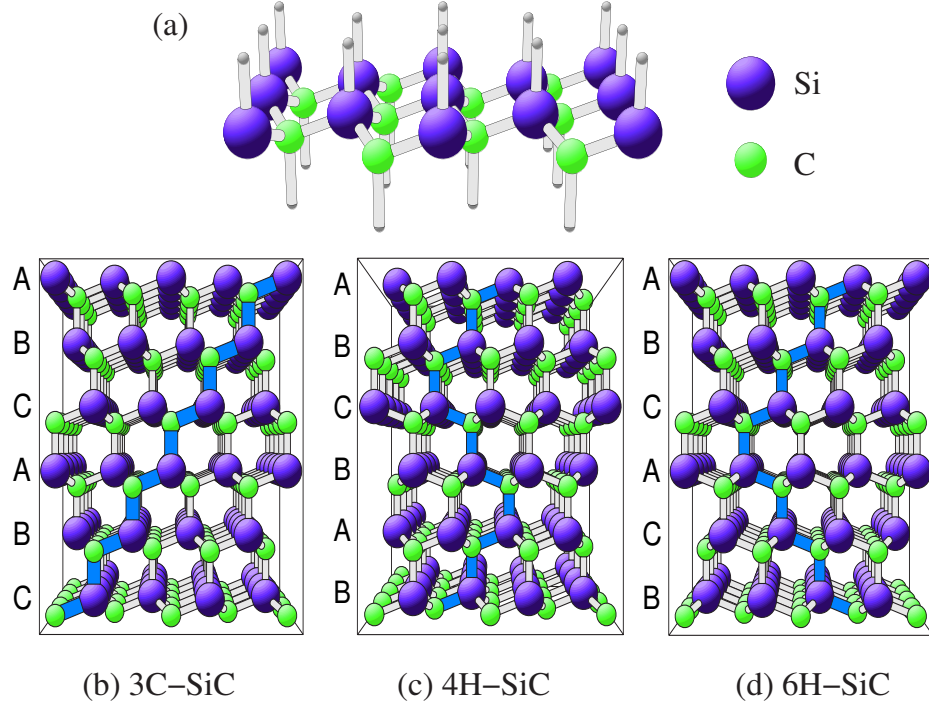


Figure 1.1: The crystal structure of commonly used SiC polytypes. The stacking sequence of Si-C bilayers along the  $c$ -axis ( $0001$ ) determine the properties of each SiC polytype. (a) In SiC, each Si atom is bonded tetrahedrally with four C atoms and each C atom is also bonded tetrahedrally with four silicon atoms. Each bilayer plane is perpendicular to the  $[0001]$  direction. Six bilayers of each polytype are plotted: (b) 3C-SiC has ABC stacking sequence as common fcc structure. (c) 4H-SiC has ABCB stacking sequence with hexagonal structure, which is displayed parallel to SiC  $\{11\bar{2}0\}$  plane. (d) 6H-SiC(hexagonal) has ABCACB stacking sequence with structure. This figure is after Ref. [1].

3C-SiC, 4H-SiC, and 6H-SiC. 3C-SiC is the only form of SiC with a cubic crystal structure, whose stacking sequence is ABC...; 4H-SiC and 6H-SiC, which have stacking sequences of ABCB... and ABCACB... respectively, are two of many SiC polytypes with a hexagonal crystal structure. Hexagonal SiC crystals have a polar  $c$  axis, which means the two opposite faces of the SiC along  $c$  axis terminate with different atoms, i.e. silicon atoms on Si-face ( $0001$ ) and carbon atoms on C-face ( $000\bar{1}$ ). The two faces are different in physical and chemical properties. The plane formed by a bilayer sheet of silicon and carbon atoms is defined as the basal plane, and the stacking direction  $[0001]$  is normal to the basal plane. Figure 1.1 depicts schematically the stacking sequence of the 3H-SiC, 4H-SiC and 6H-SiC polytypes, respectively [1].

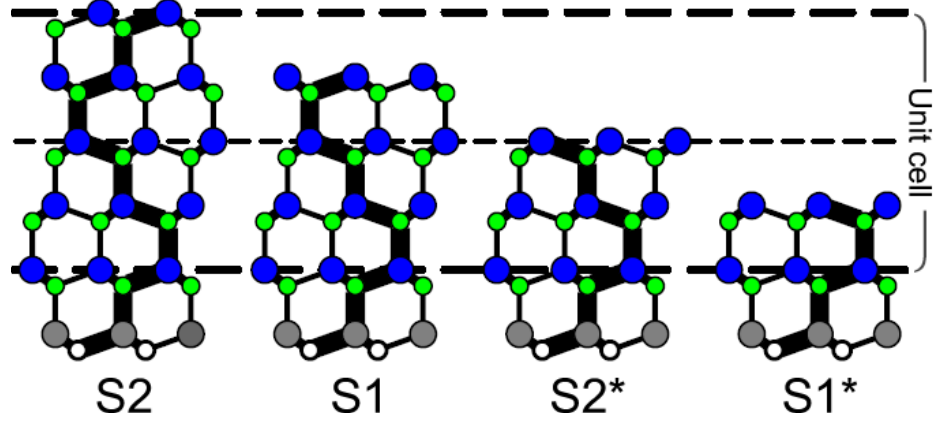


Figure 1.2: Four possible bulk-terminated surface layer stacking sequences on 4H-SiC (0001). S1 and S2 are different configurations according to different orientated bilayers.  $S1^*$  and  $S2^*$  have the same configuration as S1 and S2 respectively, after a  $60^\circ$  rotation along [0001] axis. This figure is after Ref. [2].

The bulk termination of SiC may influence graphite film growth, therefore characterizing it is important. The truncated layer can be any SiC bilayer and a different truncated layer brings a different configuration from the side view. For instance, 4H-SiC has four possibilities of termination, which are labeled S1, S2,  $S1^*$  and  $S2^*$  in Fig. 1.2. Configuration S1 and S2 are different, while  $S1^*$  and  $S2^*$  have the same configuration as S1 and S2, respectively, after a  $60^\circ$  rotation along (0001) axis [1]. If the entire surfaces consistently terminated with one type of bilayer, the LEED patterns show 3-fold symmetry rather than the typically observed 6-fold symmetry. This phenomenon exists on  $H_2$  etched SiC. The crystalline structure of SiC determines that if the SiC (0001) or (000 $\bar{1}$ ) surfaces are terminated randomly on different domains, the corresponding LEED diffraction spots will be 6-fold symmetric.

### 1.2.2 CVD Growth of SiC Wafer

Growing high quality SiC wafers has been a challenging task since SiC was discovered in the early nineteenth century. High quality SiC wafers are much more difficult to prepare than silicon or germanium, since SiC will sublime before melting at a certain high temperature, which will invalidate the traditional silicon crystal growth treatments. Two state-of-the-art methods are commonly used for growing high quality SiC wafers. One is Seeded Sublimation

Growth, which was invented by Tairov and Tsvetkov in 1978 [22] and developed by Cree Inc. [23]. Cree used the “step-controlled epitaxy” technique to grow high-quality epitaxial SiC on off-axis SiC substrates in 1989 [20] and the company further developed into the biggest commercial SiC wafer manufacturer. In the seeded sublimation growth process, the temperature gradient between the SiC powder and the SiC seed is the critical factor and needs to be accurately controlled. The other SiC growth method is the High Temperature Chemical Vapor Deposition (HTCVD) technique developed in the mid-1990s [24]. For HTCVD method, the gases of mainly silane, ethylene, and a helium carrier are used as the sources instead of SiC powder. The silane decomposes and forms small Si liquid droplets or solid microcrystals in the HTCVD furnace. The ethylene also takes part in the reaction, forming microparticles of  $Si_xC_y$ .

### 1.2.3 Electronics Application of SiC

SiC can be used for any color LED from the visible to very short wavelength ultraviolet (UV) due to its wide band gap. The first viable full-color LED-based displays were achieved in a  $1 \times 1 \text{ cm}^2$  single crystal wafer of 6H-SiC. However, the brightness of SiC blue LEDs was only around 10 *mcd* to 20 *mcd* and the quantum efficiency was much less than 1% due to its indirect band gap [20]. Thus, although 6H-SiC has been commercialized since 1989 as the first blue LED, it has been replaced by much brighter and higher efficiency III-V nitride semiconductors, like GaN and AlN, which have attained emission at 210nm [25].

Silicon carbide has long been recognized as a good candidate for high power and high temperature electronics due to its outstanding electrical and thermal properties. Silicon carbide has a wider band gap energy and much lower intrinsic carrier concentration than silicon, which leads to a much higher-temperature functional range than silicon. For semiconductor electronic devices, the intrinsic carrier concentration is a fundamental factor in determining junction reverse-bias leakage currents. As temperature increases, the number of intrinsic carriers increases exponentially. This leads to the dramatic growth of undesired leakage currents. At sufficiently high temperature, intrinsic carrier density exceeds the doping density and the semiconductor device will not function. Silicon devices are

commonly applied below  $300^{\circ}\text{C}$  due to this issue. Taking advantage of low intrinsic carrier concentration, SiC can operate theoretically at junction temperatures of more than  $800^{\circ}\text{C}$ . Several SiC prototype devices operating at up to  $600^{\circ}\text{C}$  have been demonstrated experimentally.

Due to its high breakdown electric field, SiC can withstand a voltage gradient over eight times greater than Si or GaAs, which enables the fabrication of high-voltage and high-power electronics devices. SiC has a thermal conductivity that is higher than any metal at room temperature, which enables SiC devices to operate at extremely high power levels and still dissipate large amounts of excess heat that are generated. The high breakdown field and high thermal conductivity of SiC coupled with high operational junction temperatures theoretically permit extremely high power densities and efficiencies to be realized [26]. The significantly higher breakdown field and wide energy band gap of SiC also enable much faster power switching than comparable silicon-based power-switching devices with similar breakdown voltages. Therefore, SiC based power converters can operate at higher switching frequencies with greater efficiency.

### ***1.3 Graphite Films and Graphene***

Graphite has a three-dimensional (3D) layered crystal structure in which the carbon atoms are arranged in a hexagonal lattice. Among several possible layer stacking sequences, the AB sequence (Bernal crystal structure) is the most common and stable stacking sequence of graphite. The layer separation in the Bernal structure is  $3.35\text{ \AA}$ , which is approximately twice the van der Waals radius of carbon [27]. An AB stacking graphite unit cell has 4 atoms, as labeled by  $A$ ,  $A'$ ,  $B$  and  $B'$  in Fig. 1.3a. The dimensions of the unit cell are  $c = 6.7\text{ \AA}$  and  $a = 2.46\text{ \AA}$ . The  $A$  and  $A'$  atoms have neighbors directly above and below in adjacent layer planes, whereas the  $B$  and  $B'$  atoms do not have such neighbors [28]. The direct neighboring of  $A$  results in a bonding disturbance of electron density states, therefore only  $B$  atoms are resolved for most STM atomic resolution images on graphite [29], as will be discussed further in chapter 3. The 3-D first Brillouin zone of the Bernal graphite is formed by the planes  $k_z = \pm\frac{\pi}{c}$  and the six planes going through the 2D Brillouin zone

hexagon edges of length  $\frac{4\pi}{3a}$ .

The band structure of graphite has been studied for more than half a century since the early work of Wallace [30]. The atomic electronic configuration of an isolated carbon atom is  $1s^2 2s^2 2p^2$ . The three valence electrons in  $2s$ ,  $2p_x$  and  $2p_y$  orbitals are mixed with each other, which is well known as  $sp^2$  hybridization. These  $sp^2$  orbitals overlap and form strong  $\sigma$  bonds between carbon atoms on a graphite layer plane. On the other hand, the  $2p_z$  electrons form delocalized orbitals of  $\pi$  symmetry. The loosely bound  $\pi$ -electrons have much higher mobilities, so that the  $\pi$ -electrons play a dominant role in the electronic properties of graphite [28, 30, 31]. In one unit cell, there are 4 atoms and 16 energy bands, 12 of which are  $\sigma$ -bands and the other 4 are  $\pi$ -bands. Six  $\sigma$ -bands are bonding and the other six  $\sigma$  bands at higher energies are antibonding. These 2 groups of six  $\sigma$ -bands are separated by  $\sim 5\text{eV}$ [28]. The  $\pi$ -bands lie between these two groups of  $\sigma$ -bands. Similarly, two  $\pi$ -bands are bonding and the other two are anti-bonding. However all 16 bands are coupled and the four  $\pi$ -bands are coupled most strongly. Only half of the 16 energy bands in one unit cell are filled, thus the Fermi level lies in the middle of the four  $\pi$ -bands. The upper  $\pi$ -bands, which form the highest valence bands, overlap along the edges of Brillouin zone, making graphite a semi-metal. The  $\pi$  band overlap energy is about  $0.03\text{eV}$  [28].

Graphene is a single atomic layer of graphite with  $sp^2$  bonded carbon atoms in a honeycomb structure(Figure 1.4a). One unit cell includes two atoms. The charge carriers in graphene are mimic relativistic particles with a linear  $E - k$  dispersion following the form of Einstein's equations of  $E_{\pm} = \pm \sqrt{m^2 v_F^4 + \hbar^2 v_F^2 k^2}$ , where  $\hbar k$  is the electron momentum (Figure 1.4b). The carriers have an effective "speed of light"  $c_* \approx 10^6 \text{ms}^{-1}$ , i.e. one thirtieth of the speed of light [32]. The  $E - k$  dispersion depends sensitively on the thickness of graphene layers. The newest study on 2-layers of graphene shows that the  $E - k$  dispersion become parabolic at the Dirac point  $E_{\pm} = a \pm \sqrt{m^2 v_F^4 + v_F^2 k^2}$  [31].

Graphene is the first semi-metal two-dimensional(2D) electron- and hole-gas system. Two dimensional electron gases (2DEGs) offer a mature system of extremely high mobility electrons, especially at low temperatures. When cooled to  $10\text{mK}$ , systems can have

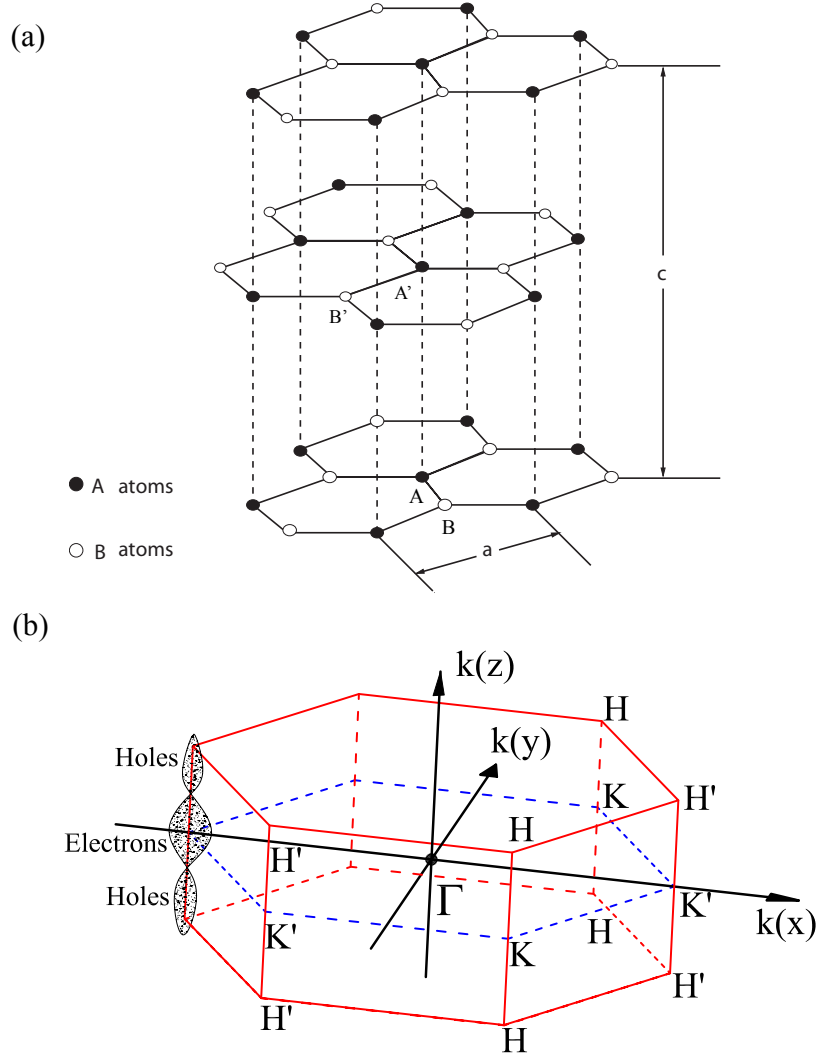


Figure 1.3: The crystal structure of graphite **ABAB** (Bernal Structure) and its Brillouin zone. (a) The primitive unit cell with dimensions  $a = 2.46 \text{ \AA}$  and  $c = 6.71 \text{ \AA}$ . The bonding in plane length is  $1.42 \text{ \AA}$ . There are four atoms per unit cell, labeled as  $A$ ,  $A'$ ,  $B$  and  $B'$ . The difference between  $A$  atoms and  $B$  atoms lies in that  $A$  atoms (solid circles) have neighbors directly above and below in the adjacent layer planes but  $B$  atoms (hollow circles) do not have such neighbors in adjacent planes. (b) The Brillouin zone of graphite. The electron and hole Fermi surfaces are located in the vicinity of the edges  $HKH$  and  $H'K'H'$ , where  $KH = \frac{\pi}{c}$ .



mobilities of  $3 \times 10^7 \text{ cm}^2/(\text{V} \cdot \text{s})$ . The typical 2DEG systems are inversion layers of MOS-FET transistors, heterojunction transistors [also called High Electron Mobility Transistor (HEMT)] and quantum wells. The graphene 2DEG is a quantum well system that confines carriers within an extremely narrow quantum well. Carrier mobilities are expected to approach  $10^6 \text{ cm}^2/\text{V} \cdot \text{s}$ . Transport in ultrathin graphite films has been studied very recently, and several striking properties have been found [11, 32–34]. Unlike nanotubes, conventional nanolithography can be applied to control the ribbon geometry and placement, which makes graphene more promising for future large-scale-integrated electronic devices. The graphite/silicon carbide system is a promising platform for ballistic-carrier devices based on nano-patterned epitaxial graphene [11].

### 1.3.1 Quantum Hall Effect and Landau Levels

A 2-D electron system (2DES) has confinement along the z-axis (perpendicular to the 2DES plane), so the energy of an electron for a motion along the z axis is quantized. What's more, if a strong magnetic field perpendicular to the plane exists, the energy in plane is also quantized, which is called Landau quantization.

The Hall resistance in 3-D bulk conductor is

$$\rho_H = \frac{H}{nec} \quad (1.1)$$

which is a smoothly varying function of the density of carriers and magnetic field [35]. For a 2D electron gas surface, the electrons are confined in a plane, when we add a strong magnetic field perpendicular to the surface, the semiclassical electrons in the center will travel in orbits with the cyclotron frequency [36],

$$\omega_c = \frac{eH}{mc}, \quad (1.2)$$

and its energy is quantized with

$$\varepsilon = (n + \frac{1}{2})\hbar\omega_c. \quad (1.3)$$

The circular motions of electrons in the center do not contribute to the net current. The current is from the “skipping orbits” of electrons at the edge of the sample. Therefore

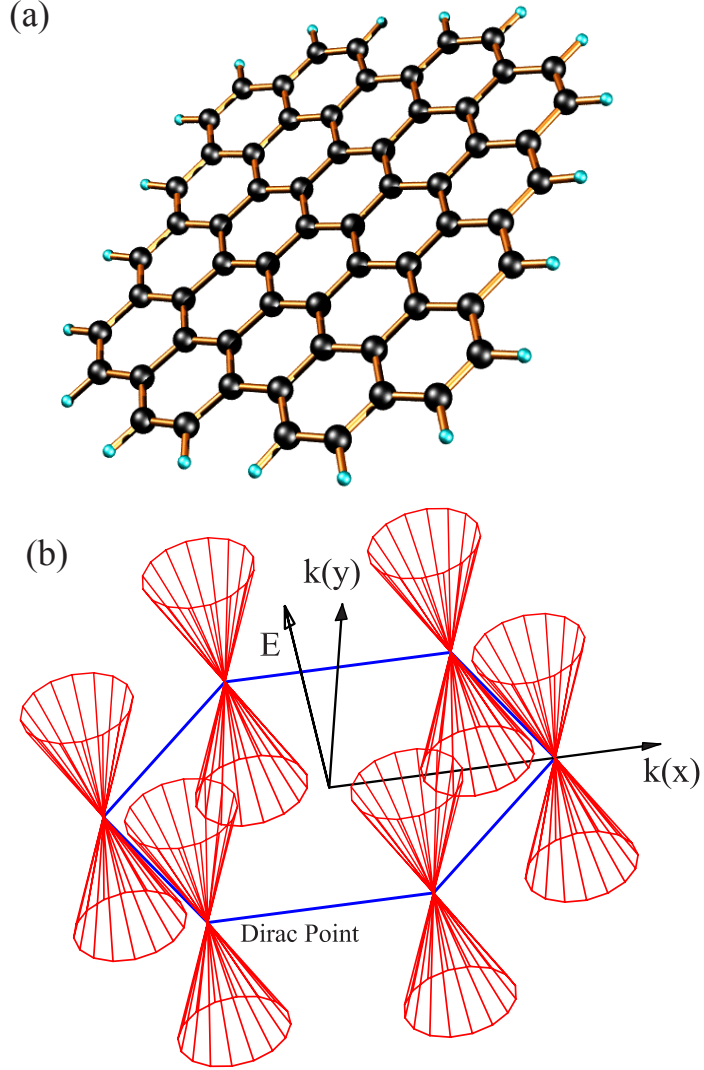


Figure 1.4: Representations of graphene in real space and momentum space . (a) Graphene's honeycomb lattice. Each carbon atom (black solid ball) has three covalent  $\sigma$ -bond electrons bonding tightly with three other carbon atoms in plane and one  $\pi$ -bond electron having high mobility.  $\pi$ -bond electrons wander across the plane and forming 2D electron gas. Hydrogen atoms (representing with the small blue balls) are often used to passivate the dangling bonds hanging on the edge of graphene. This figure is after Ref. [3]. (b) Band structure of the graphene film. The energy-momentum dispersion is linear,  $E = \hbar k |v_F|$  near the Dirac points representing as the vertices of the blue hexagon.

the Hall resistance vs. number of electrons curve shows plateaus, which is known as *integral Quantum Hall Effect* for impure samples and *fractional Quantum Hall Effect* in pure samples.

The Hall conductance  $\sigma_{xy}$  takes on the quantized values

$$\sigma_{xy} = \nu \frac{e^2}{h} \quad (1.4)$$

with  $\nu$  the “filling factor”, Hall constant. The Hall conductivity is measured perpendicular to the direction of current flow. At the same time, the resistivity measured parallel to the current flow goes to zero:  $\rho_{xx} \rightarrow 0$ . In the the integer Quantum Hall Effect,  $\nu$  takes on integer values ( $\nu = 1, 2, 3$ , etc.) with a precision of about  $10^{-10}$ . In the fractional quantum Hall effect,  $\nu$  can occur as a rational fraction.

However, QHE phenomenon of the 2DEG in graphene is special. The first plateau in the Hall conductivity is equal to  $2e^2/h$  (Fig. 1.5), which is a half filled Landau level. For graphene, the filling factor  $\nu = 4$  is due to the double-spin and double-valley degeneracy. The half integer shift was explained by Geim’s group with “pseudospins”, which have nothing to do with the real spin but are “built in” to the Dirac-like spectrum of graphene [4, 18].

### 1.3.2 Graphite Films/SiC system

It has been demonstrated that heating 4H/6H-SiC (0001) or (000 $\bar{1}$ ) samples in ultra high vacuum (UHV) or high vacuum environment results in the depletion of silicon from the surface, with the development of several reconstructions, culminating in the formation of thin graphite films [37–39]. Three SiC bilayers of carbon atoms can collapse into one graphene layer according to the 2-D atom densities of SiC and graphite. The mechanism of graphite growth on both faces is obviously different but still not yet clear. On Si-face, the low energy electron diffraction (LEED) patterns show that there is a  $30^\circ$  rotation between the graphite unit cell and the SiC substrate unit cell. When the graphite film is thin, a very complicated  $6\sqrt{3} \times 6\sqrt{3}$  R $30^\circ$  reconstruction LEED pattern can be observed. STM on Si-face shows that the graphite films have a SiC  $6 \times 6$  surface corrugation and the surface has many domains. On C-face, the graphitization starts  $50^\circ$  C lower in temperature than on

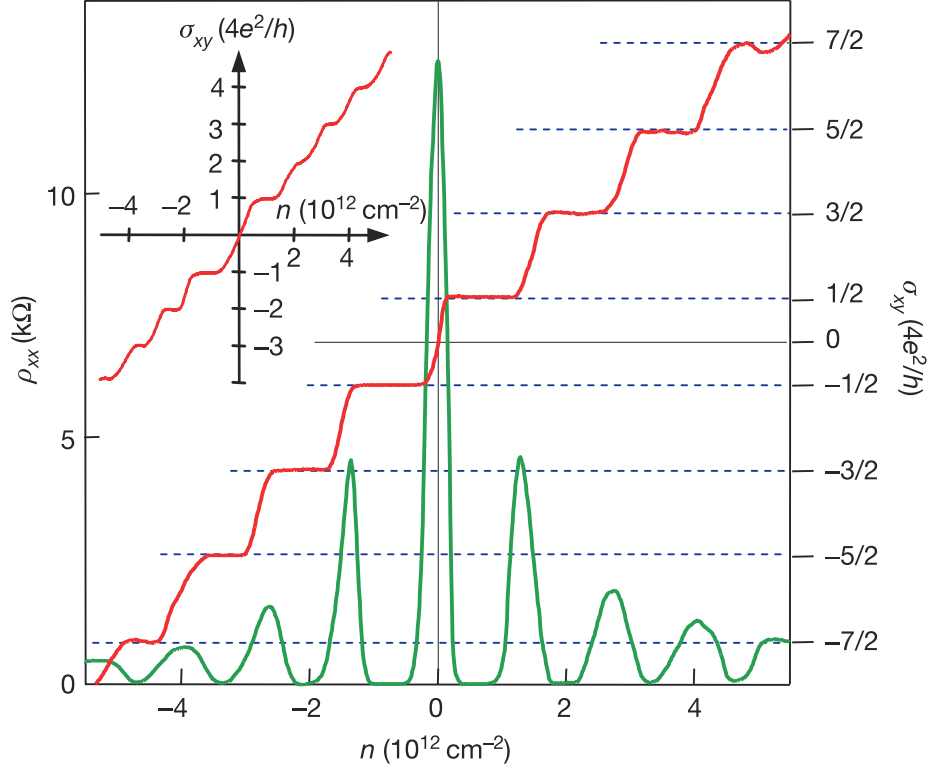


Figure 1.5: Quantum Hall Effect in graphene. The green line is the longitudinal resistivity  $\rho_{xx}$  of the graphene 2D electron gas in high magnetic field.  $\rho_{xx}$  goes to zero at the values where the transverse conductivity  $\sigma_{xy}$  is quantized in units of  $e^2/h$ . The factor 4 is due to the spin and band-structure degeneracy in graphene. The inset plot shows that the 1/2-integer phase shift disappears and the band symmetry changed when one of the systems has more than one graphene sheet. This figure is after Ref. [4].

the Si-face and has a much higher growth rate. The LEED pattern on thicker C-face films shows graphite rings instead of the graphite diffraction spots on Si-face, which represents the azimuth disorder of graphite on the surface. The graphite ring is not continuous but split into several arcs. STM on C-face shows that surface has carbon nanotube and nanocap structures [40–43].

## ***1.4 Work in This Thesis***

My thesis work focuses on 1) growing large-scale high quality flat graphite films, 2) characterizing graphite films grown on both Si and C faces of SiC, and 3) identifying the interfaces between graphite films and SiC. The study of the interface on the Si-face gives a partial solution to the controversy of the mechanism of the initial graphite growth. The transport properties of a graphite/SiC system are very likely connected to the interfacial layers. In this thesis, I trace the evolution of LEED patterns and Auger electron spectra (AES) in the stepwise heating of SiC(0001) face by electron-bombardment heating in UHV and SiC(000 $\bar{1}$ ) face after RF furnace heating. I also record STM images on different thickness graphite films on both faces of SiC. With clear LEED patterns and Fourier analysis on STM images of the graphite films on SiC(0001), I evaluate the origin of LEED diffraction spots of the SiC  $6\sqrt{3} \times 6\sqrt{3}$  R30° reconstruction on SiC(0001), emphasizing the kinematic scattering model. Through LEED, AES and STM, I conduct surface analysis on graphite ribbons grown on vicinal 6H-SiC samples and graphite ribbons patterned by an E-beam lithography process. I also investigate the surface topology of the graphitized SiC(000 $\bar{1}$ ) surface and identify different graphitized surface structures from the SiC(0001) face.

## CHAPTER II

### EXPERIMENTAL APPARATUS AND TECHNIQUES

Most surface studies in this paper were performed in a home built ultra high vacuum (base pressure  $< 10^{-10}$  Torr) surface-analysis chamber [44]. The system is equipped with a ion sputtering gun, a field emission/ion microscopy, a 4-grid LEED system, a single-pass cylindrical mirror analyzer, and a scanning tunneling microscopy. The LEED, AES, and STM, as the most related techniques will be discussed below.

#### ***2.1 Low Energy Electron Diffraction***

##### **2.1.1 Four-grid LEED System**

The four-grid reverse view LEED system was made by Princeton Research Instruments [5]. The complete unit is mounted on an 8 inch OD knife edge flange. The diagram of the LEED optics is depicted in Fig. 2.2. The four metal mesh grids and the phosphor screen (collector) are constructed as concentric hemispheres. The sample sits at the center of these hemispheres. Metal mesh Grid 1 is common grounded, thus scattered electrons fly freely within the hemisphere of Grid 1. Grids 2 and 3 are both connected to a negative suppress voltage source acting as a high energy pass filter, which suppresses the inelastically scattered electrons and improve the LEED contrast. Grid 3 is helpful in eliminating the inhomogeneities caused by the high electrical field of the phosphor screen. Grid 4 is grounded to reduce the capacity between the collector and Grid 3 and to exclude any possible AC modulation voltage from suppress grids to the collector, which is important when the four-grid LEED system is used as a retarding field analyzer for the AES experiments. A positive bias from 2kV to 5kV is applied to the phosphor screen to collect the electrons with energy higher than suppress bias for a LEED pattern or RFA collector current.

The bias controls are the key to obtaining sharp LEED patterns. Four voltages can be adjusted in our LEED system,  $V_1$  for emission current,  $V_2$  for focusing, and  $V_3$  for retarding

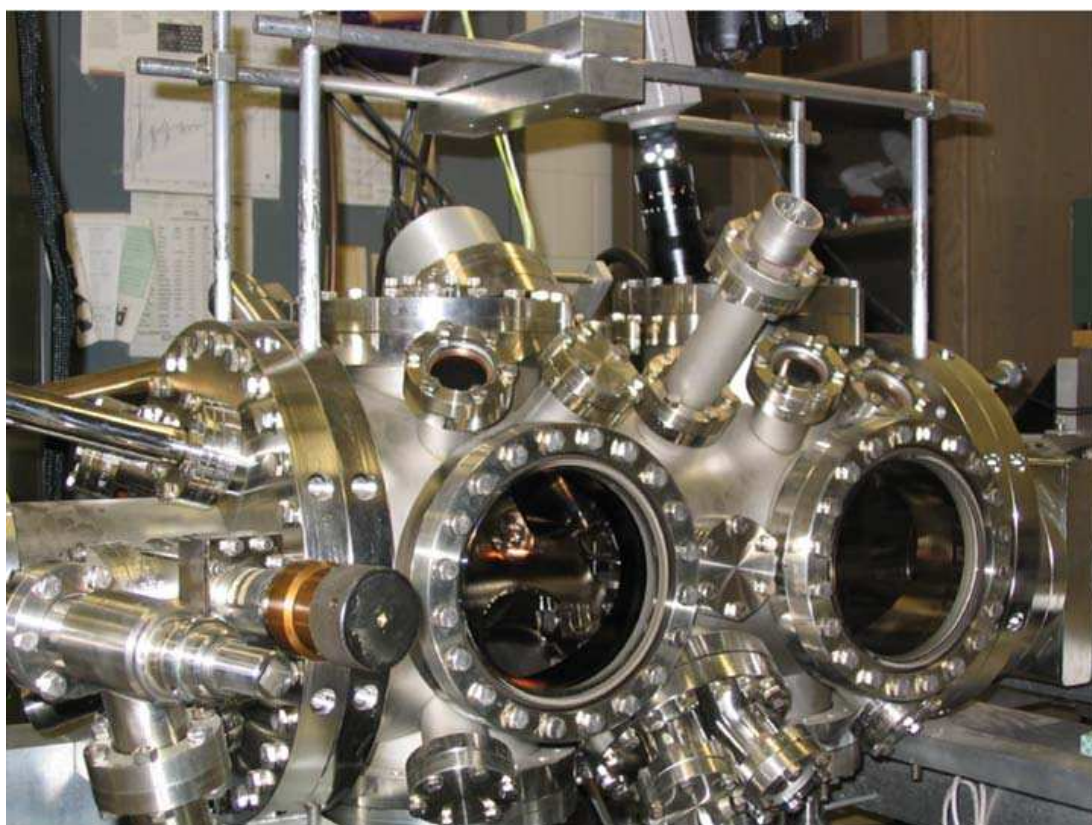


Figure 2.1: A picture of the room temperature, ultra high vacuum scanning tunneling microscopy system. The chamber includes capabilities for scanning tunneling microscopy, low-energy electron diffraction, Auger electron spectroscopy, ion beam sputtering, a field ion/field emission microscope, metal deposition, residual gas analysis, and a load-lock for tip/sample exchange.

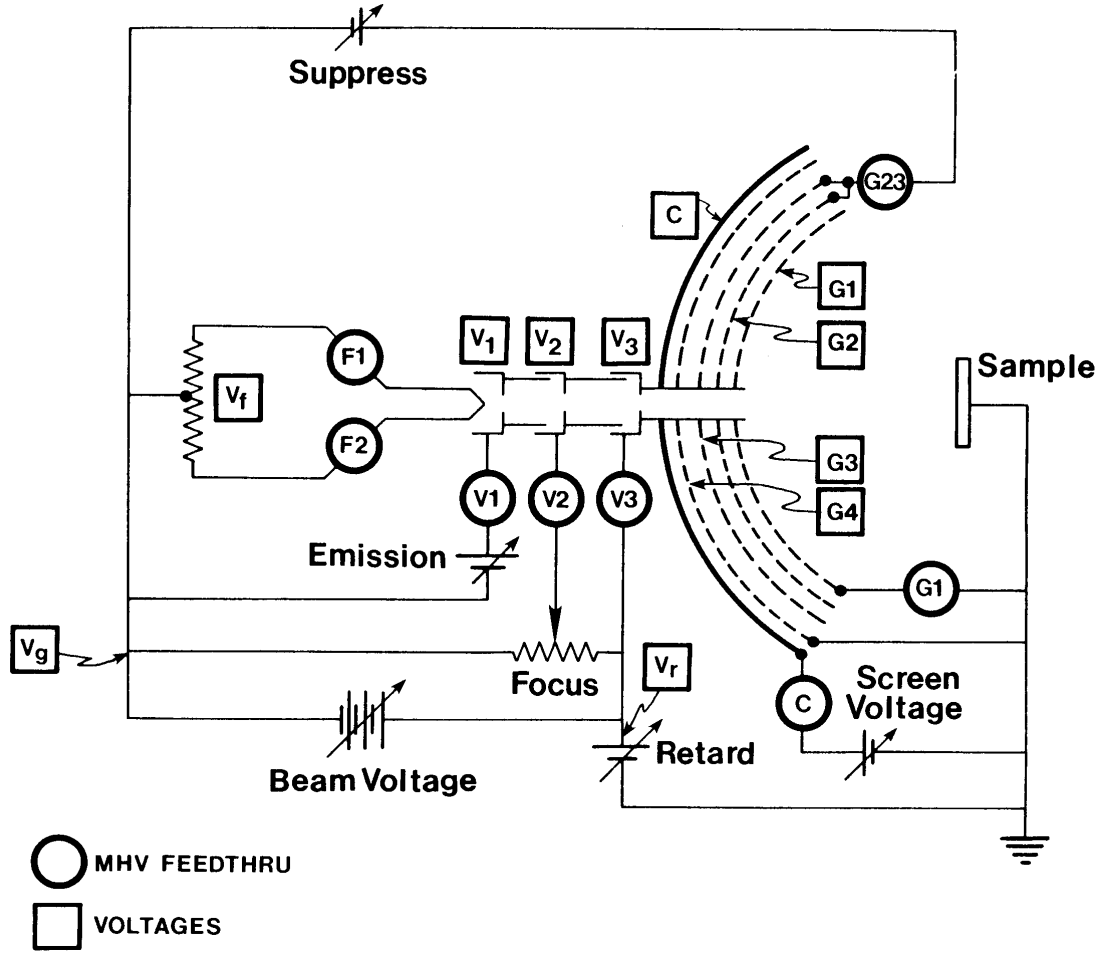


Figure 2.2: The diagram of the four-grid reverse view LEED system optics. This figure is from the manual of the LEED system [5].

and suppress voltage adjusting contrast. The gun is designed to maintain the stability of the focus at different energies when the ratio of  $(V_2 - V_f)/(V_3 - V_f)$  is fixed. Since we did not fix that ratio, we kept adjusting the above voltages for the optimum images at different beam energies. The emission bias controls the size and intensity of the electron beam and should be set around 20% to 50% of the maximal value for optimum focus and contrast.

### 2.1.2 LEED Pattern Interpretation

The kinematic LEED pattern can be interpreted straightforwardly with the aid of Ewald sphere construction. For an ideal single layer of 2D lattice, the reciprocal lattice changed from 3D reciprocal lattice points to 2D rods, like (01), (02), the directions of which are



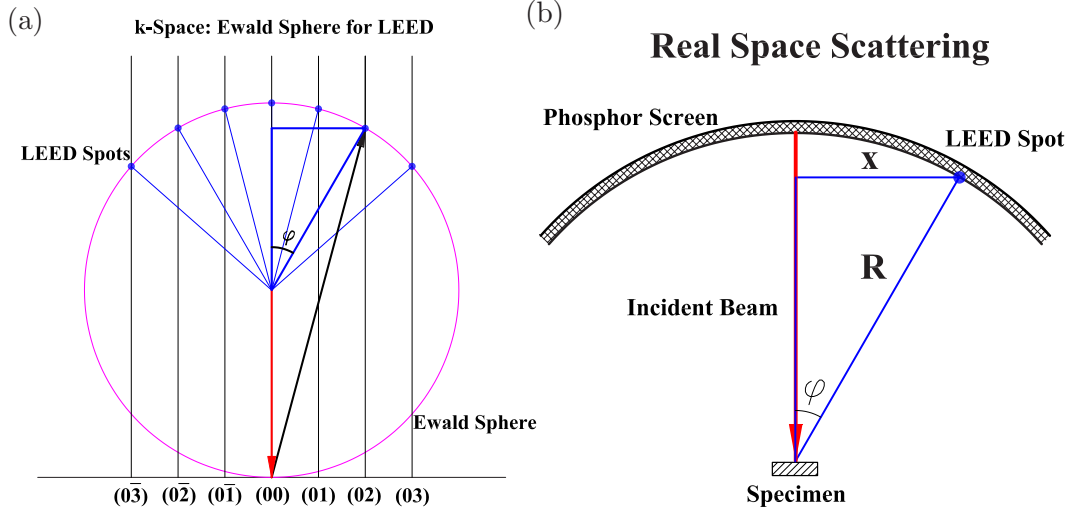


Figure 2.3: (a) 2D LEED diffraction interpreted with Ewald sphere. Surface diffraction rods (01), (02), and ... are normal to the 2D crystalline plane and intercepted by the Ewald sphere at the constructive diffraction spots. (b) Diffraction beams and LEED spots in real LEED system. The blue triangles in two figures are analogous, which determines a direct mapping from the diffraction spots on camera photos and reciprocal lattices through a simple formalism.

parallel and perpendicular to the 2D plane (Fig. 2.3a). A simple geometric relationship between the constructive diffraction triangle in Ewald sphere and the triangle in real optics exists, therefore the LEED picture obtained with a camera exactly maps certain 2D reciprocal lattices of the top layers of the sample (Fig. 2.3) [45]. The lattice constant of a hexagonal 2D structure can be calculated by the following formula,

$$a = \frac{2}{\sqrt{3}} \frac{R}{x} \sqrt{\frac{150.4}{E(\text{eV})}} \quad (2.1)$$

Where  $R$  is the radius of the phosphor screen,  $x$  is the distance between the first order diffraction spot of the hexagonal lattice and the origin spot (00), and  $E$  is the energy of electron beam in eV. The unit of lattice constant  $a$  is angstrom. Since the lattice constant of SiC is already known accurately, we can measure the LEED pattern to calibrate the sample surface to the center of the concentric sphere grids in the LEED system.

## 2.2 Auger Electron Spectroscopy: Single-pass CMA

### 2.2.1 Auger Process

Auger process is an electron-impact inelastic ionization process. Since the output Auger electron energy relates directly with the core subshell energy bands, Auger electron spectrum can record the feature peaks like the finger prints of each element. Fig. 2.4a depicts a typical  $KL_1L_2$  Auger process. An electron in K shell is excited by the high energy incident electron beams and leaves a hole on K shell resulting in a decay that an electron from  $L_1$  shell transits to K shell filling the hole. The transition energy is transferred to another electron in another L subshell and this electron escapes from the bonding of the core and become an Auger electron. The energy of an KLL process Auger electron is

$$E_{kin} = E_K - E_{L1} - E_{L2}, \quad (2.2)$$

where  $E_{L1}$  and  $E_{L2}$  are the binding energies of  $L_1$  and  $L_2$  levels [46].

The universal curve (Fig. 2.4b) gives the relation between inelastic mean free path (i.e., escape depth in the Auger process) and kinetic energy of the electrons. The escape depth of the Auger electrons of Si and C can be estimated from this universal curve, which is useful for estimating the thickness of graphite films roughly.

### 2.2.2 Modulation Technique for Auger Spectra

Buried in the strong secondary electron background, Auger electron signal is measured with a modulation technique applied by an additional Lock-in Amplifier. The Lock-in Amplifier superimposes a modulation voltage  $\Delta E = k \sin(\omega t)$  on the pass energy of an electrostatic analyzer, then the total current collected can be written as a Taylor series:

$$I(E + \Delta E) = I(E) + I'(E)\Delta E - \frac{I''(E)}{2!}\Delta E^2 + \frac{I'''(E)}{3!}\Delta E^3 + \dots \quad (2.3)$$

where the prime denotes differentiation with respect to E. Therefore,

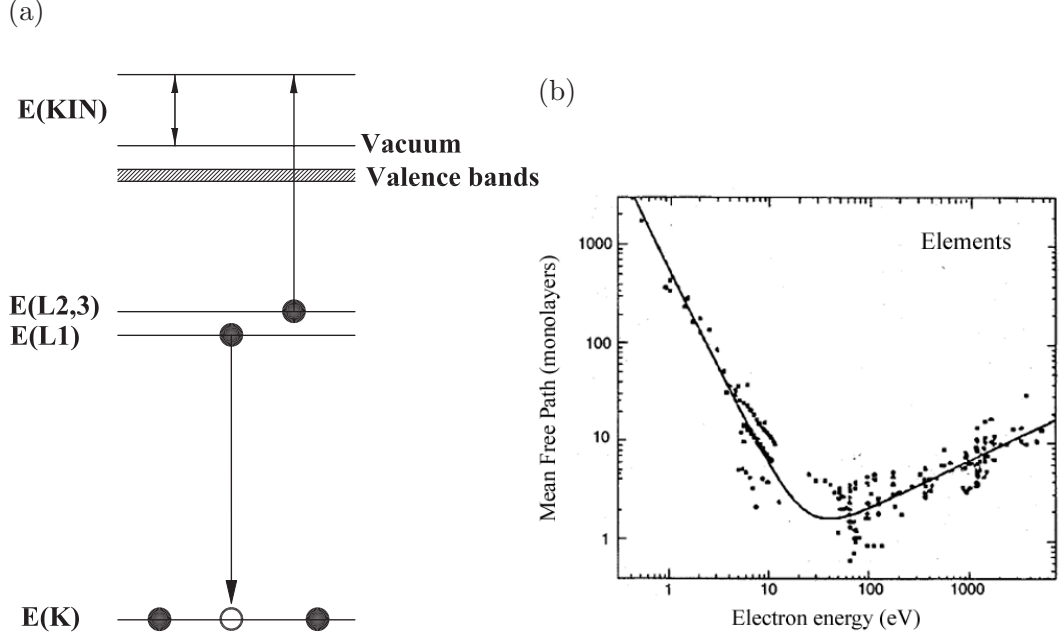


Figure 2.4: (a) A schematic drawing of the KLL Auger process. (b) Universal curve of the inelastic mean free path vs. electron energy. The solid line is the theory result. This figure is after Ref. [6, 7].

$$\begin{aligned}
 I &= I_0 + (I'K + \frac{I'''}{8}K^3 + \dots) \sin \omega t - (\frac{I''}{4}K^2 + I''') \cos 2\omega t \\
 &\simeq I_0 + I'K \sin \omega t - \frac{I''}{4}K^2 \cos 2\omega t
 \end{aligned} \tag{2.4}$$

When the modulation voltage  $K$  is small (Note:  $K$  should be less than 3 volts, and we used 0.34 volt for our AES experiments.), the higher order terms can be neglected.

We used the retard field analyzer to measure the AES in our low temperature STM system. The current acquired from the collector of RFA is the integral of electrons with energy above the retard field, therefore, we should set the Lock-in at the second harmonic of the modulating frequency mode, which displays the second derivative of collector current, the magnitude of which is proportional to the Auger spectrum  $\frac{dN(E)}{dE}$ .

A single-pass cylindrical mirror analyzer (CMA) is used for AES measurement in our room temperature STM system. The diagram of the CMA is in Fig. 2.6. Due to a preset electrical field between the inner and outer shells of the cylinder, only electrons with a certain energy ( $E \sim E + \Delta E$ ) can pass the cylinder and contribute to the collector current.

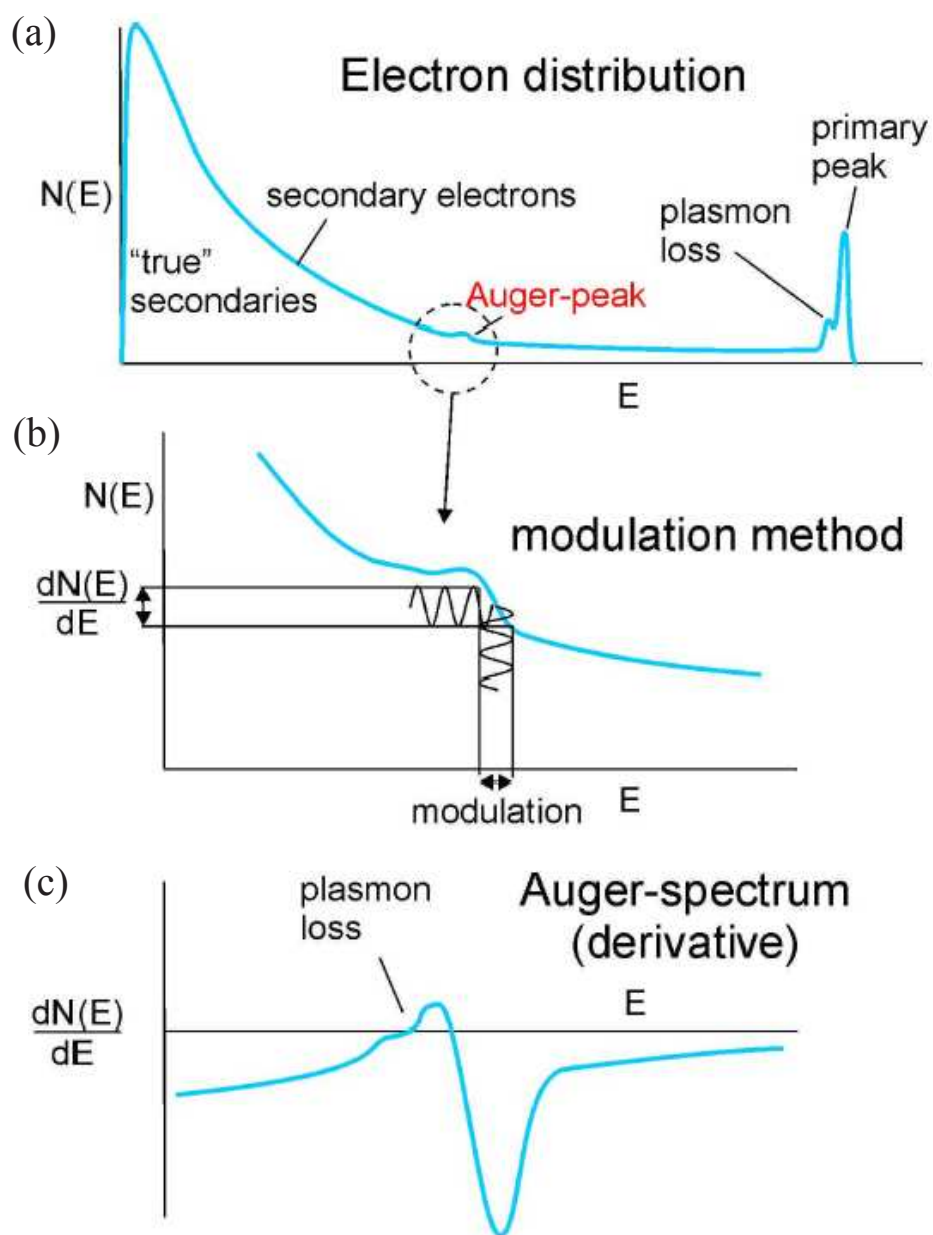


Figure 2.5: Modulations techniques used for AES analysis. (a) Electron and current distribution of signals are the same in CMA method ( $I(E) \propto E \cdot N(E)$ ). (b) Adding modulation to the Auger electrons distribution  $N(E)$ . (c) The first derivative of current distribution gives the AES spectrum. This figure is after Ref.[8].

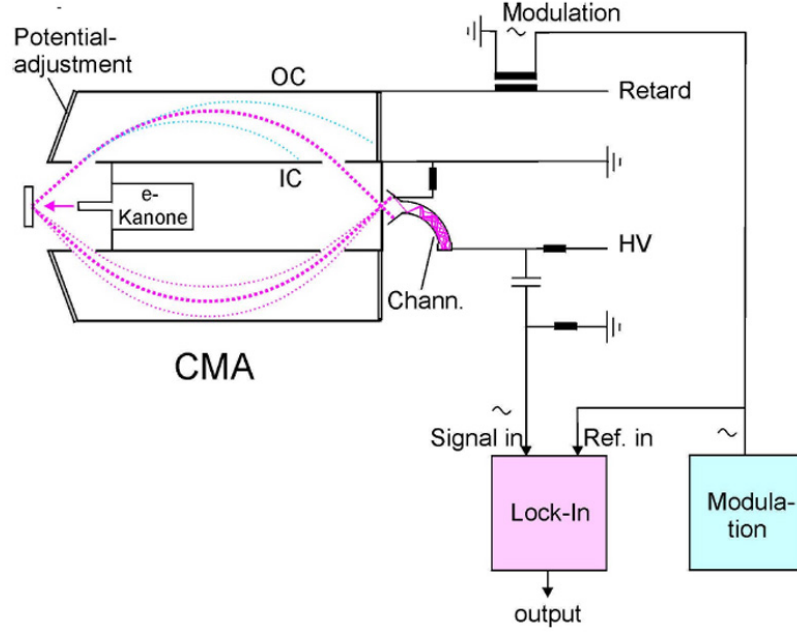
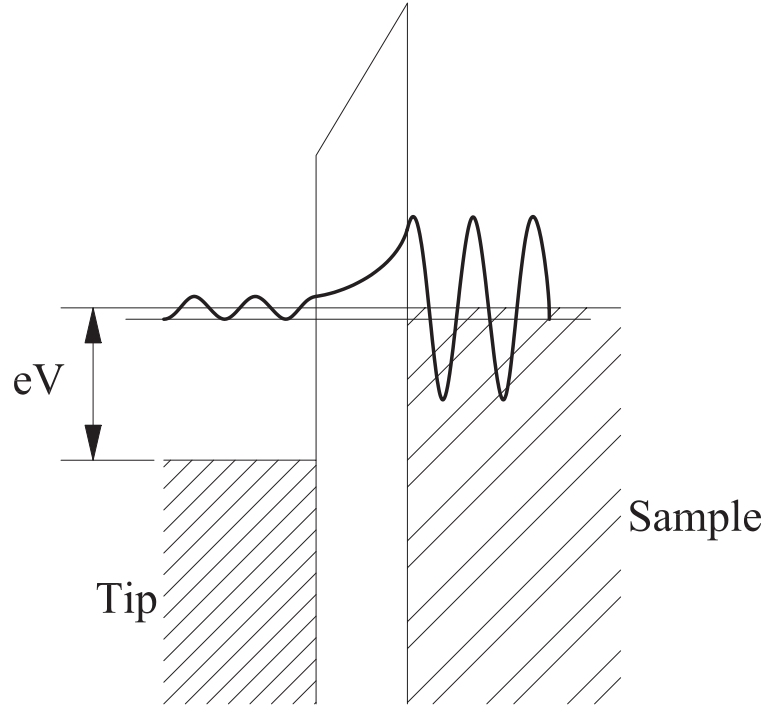


Figure 2.6: A schematic diagram of the single pass cylindrical mirror analyzer. This figure is after Ref. [8].

The bias between inner and outer cylinders is  $V = 1.3E \cdot \ln(R_{out}/R_{in})$ , where  $L_0 = 6.1R_{in}$  and  $E$  is the energy of Auger electrons. Since  $\Delta E/E$  is independent of  $E$ , the collector current  $I \propto E \cdot N(E)$ . Instead of the second derivative used in a RFA, the first derivative of the collector current in CMA is used here, which is equal to  $E \cdot dN(E)/dE + N(E)$ . The two terms are opposite signs when the E-beam energies are below 200eV, resulting in a flat background. On the other hand, Auger electron intensity dramatically increases with decreasing E-beam energy, which is compensated by the gain decreasing of the multiplier with energy dropping, therefore the whole spectrum can be recorded with the same gain (Fig. 2.5). The amplitude  $A(\omega)$  at frequency  $\omega$  is given by

$$A(\omega) \approx KI'(E) \propto \frac{dN(E)}{dE} \quad (2.5)$$

The CMA acts as an energy bandpass filter and the RFA is a high energy pass filter. Therefore the actual collector current of CMA is around  $10^4$  smaller than that of RFA, which leads to a higher signal to noise (SNR) ratio of factor  $10^2$  [45].



STM Schematic Tunneling

Figure 2.7: A schematic diagram of STM tunneling.

## 2.3 *Scanning Tunneling Microscopy Techniques and Equipments*

### 2.3.1 STM Techniques

Instead of using light source or electron guns as traditional microscopes, a scanning tunneling microscope (STM) applies an ultra sharp tip to sense the tiny current tunneling to the approached surface for collecting the surface information. Due to its high lateral and vertical resolution, STM is able to reveal the atom arrangement and/or the local density of states (LDOS) on surface in real space, which is an important complimentary result to the LEED diffraction patterns, since LEED holds reciprocal lattices' information. Comparison between images from these two tools usually solves straightforwardly surface atom arrangement. Further, scanning tunneling spectroscopy (STS), a function associated with most STM systems, provides atomically resolved spectroscopy, which contains a wealth of important information of surfaces, such as LDOS, band gaps, dangling bonds, adsorbates,

and chemical compositions.

The simplest STM tunneling model can be obtained from the typical finite rectangular barrier problem of quantum mechanics (Fig. 2.7). An immediate derived tunneling current is given by  $I \propto e^{-2\kappa d}$ , where  $\kappa = \sqrt{2m(V_B - E)/\hbar}$ . For STM experiments, the work function of material  $V_B$  is about  $4 \sim 5$  eV and the  $\kappa \sim 1$  Å, so typically the current drops almost an order of magnitude for every additional 1 Å tip sample gap. When the coupling between the tip and the sample is very weak, the first-order perturbation theory exists and the current can be expressed as,

$$I = \frac{e}{h} \sum_{\mu, \nu} |M_{\mu\nu}|^2 \delta(E_\mu - E_\nu) f(E_\mu) f(E_\nu + eV), \quad (2.6)$$

$$M_{\mu\nu} = \frac{\hbar}{2m} \int (dS(\psi_\mu^* \nabla \psi_\nu - \psi_\nu^* \nabla \psi_\mu)) \quad (2.7)$$

where  $M_{\mu\nu}$  is the matrix element between the filled states  $\psi_\mu$  and the empty states  $\psi_\nu$ . The tunneling only occurs from filled states to empty states. Positive tip voltage leads to filled states of the specimen, and the negative tip voltage represents the empty states. The  $\delta$  function means that only elastic tunneling is considered.

The formalism above assumes that the two electrodes can be described as independent systems and the tunneling is regarded as a small coupling, which does not perturb significantly the wave functions. However, this assumption is often far away from the real situation of STM experiments since the barrier shape in 3D is very complicated. Nevertheless, this method is still widely used since it incorporates the band structure and surface density of states into the calculation [47].

Another approach to studying tunneling current is to solve the Schrödinger equation, which requires tremendous calculation to consider real metal Fermi surfaces as well as a complex tip and sample geometry. Simmons (1963) gave the solution with a simplified model of one dimension tunneling using the WKB approximation and a free electron metal [48]. With WKB approximation, the tunneling current can be written as

$$I = \int_0^{eV} V dE D_\mu(E - eV) D_\nu(E) M(E, V) \quad (2.8)$$

where  $D_\mu$  and  $D_\nu$  are the density of states (DOS) of the tip and the specimen. Further calculation with locally sphere tip model also shows that the density of states are relevant for the tunneling current [49].

In STS experiments, I-V curves for fixed separations are obtained by measuring the variation of the tunneling current as a function of voltage at a constant tip-sample separation. If  $D_\mu$  and the transmission coefficient  $M(E, V)$  are constant,  $\partial I / \partial V$  is proportional to the density states of the sample. However, the transmission coefficient is not a constant due to the exponential growth of current with voltage, therefore the normalized differential conductance  $\frac{dI/dV}{I/V}$  is often used, which is equal to  $d(\ln I) / d(\ln V)$ .

$$\frac{dI/dV}{I/V} = \frac{D_\nu(eV) M(eV)}{\frac{1}{eV} \int_0^{eV} D_\nu(E) M(eV) dE} \quad (2.9)$$

The normalized differential conductance provides a good approximation to the surface density of states, however it doesn't work at the band gap edge, where the current goes to zero much faster than the differential conductance. Usually, density of states goes to zero at band edges, so the large peaks appearing on the edge of the band gaps are due to the divergence not the large density of states. One way to solve this problem is to average  $I/V$  over a large scale voltage [47, 50, 51].

### 2.3.2 Room Temperature STM

The thorough description of our home-built, room temperature STM can be found in previous literature [52]. In a nutshell, The STM tip scanner consists of concentric piezoelectric tubes. The 12.5 mm diameter outer tube controls tip-sample separation along Z axis, while the inner 6 mm diameter tube is split into four quadrants and used for scanning along horizontal X and Y directions. The sample block is connected to the virtual-ground input of an in situ Op-Amp (OPA128 [53]) current-to-voltage converter ( $10^8 V/A$ ), which has less than 0.01 pA noise. A switch is mounted on the Op-Amp to select modes of via or bypass the Op-Amp. A voltage pre-amplifier is used to further amplify the voltage up to preset value



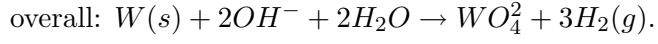
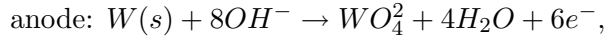
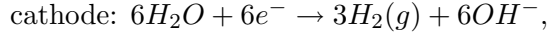
and feed this signal ( $V_{in}$ ) into a log amplifier. The  $V_{in}$  is compared with a reference signal of  $V_{ref} = 1V$ , which yields an error signal output from the log amplifier,  $V_{err} = A \log_{10}(\frac{V_{in}}{V_{ref}})$ , where  $A$  is the gain of the log amplifier. Since the tunneling current has an exponent relationship with the tip-sample distance, this error signal  $V_{err}(x)$  is proportional to the difference between instantaneous tip-sample distance  $d(x)$  and the preset reference distance  $d_0$ . This error signal is amplified and transferred to a voltage signal  $V_z$  which is applied to the center piezo tube. Since  $V_z$  also has a linear relationship to the difference of  $d(x)$  and  $d_0$ , i.e.,  $V_z \propto [d(x) - d_0]$ , the error signal can be used as a feedback to adjust the tip-sample distance  $d(x)$  to approach preset  $d_0$  so as to approximately maintain a constant tunneling current. As for the coarse motion of the STM system, it is accomplished by using Burleigh piezoelectric inchworm motors to push/pull the sample block [54, 55].

### 2.3.3 Low Temperature STM

The thermal limit determined by the width of the edge of the Fermi distribution of electrons in the metal electrodes is about  $2kT$  ( $\sim 50meV$ ). The resolution is good enough for most interested features on metals, such as some inelastic process limits ( $\sim 5.4kT$ ), however, this resolution is not sufficient for band gap of superconductivity and the energies of other inelastic processes associated with photons or excitations of vibrational models of adsorbed molecules ( $\sim 5meV$ ). The quantum confinement of narrow graphite ribbons determines that the band gap is dependent to the width of the ribbon. when width of graphite ribbons changes from  $10nm$  to  $1\mu m$ , the band gap varies from  $10meV$  to  $1eV$ , which smaller than the thermal limit of RT STM, therefore a LT-STM is necessary for an accurate graphite IV spectroscopy measurement. Moreover, the low temperature of the STM freezes the motion of most adsorbates that can be evaporated onto the sample surface either inside or outside the STM, so that the surface can be scanning for several weeks without degradation. We have collaborated with the STM lab at NIST for the study of graphitized SiC and obtained excellent atomic resolution graphene STM images and high resolutions spectroscopies[56].

### 2.3.4 Tip Preparation

All the STM experiments in this paper were done with the tungsten tips that have high stiffness, high purity and good inertness. The tungsten tips were prepared through traditional electrochemical method (AC current etching). The electrochemical reaction is



In this reaction, tungsten was dissolved to soluble tungstate ( $WO_4^{2-}$ ) anions at the anode, and the water was dissolved into hydrogen forming bubbles and  $OH^-$  ions at the cathode [55]. The oxidized layers of the tips were removed by bombardment heating in the UHV chamber.

## CHAPTER III

# CHARACTERISTICS OF GRAPHITE FILMS ON SiC (0001) SURFACE

### 3.1 *Sample Preparation*

Our two SiC wafer suppliers are Cree, Inc. [23] and NASA Glenn [57] Research Center. Cree is our major 6H- and 4H-SiC wafer supplier. The wafers from Cree are all completed 2-inch wafers, which were first sawed into small pieces in the clean room of the Microelectronics Research Center (MiRC) of Georgia Tech. The typical sample size is  $3.5\text{ mm} \times 4.5\text{ mm}$ . We only study supplier pre-polished SiC surfaces. 6H-SiC wafers as-received are either only Si face polished or both Si and C faces polished and 4H-SiC wafers are all double-side polished. All the 4H-SiC wafers are un-doped and the resistivity is  $0.5\ \Omega \cdot \text{cm}$ . The as-received surfaces of the wafers are full of scratches and surface defects (Fig. 3.1a), therefore the first treatment is to polish the surface to atomic flat level with chemical or physical methods, which is an obvious prerequisite for growing high quality graphite films.

#### 3.1.1 Hydrogen Etching and Chemical Vapor Deposition Growth

Xuebin Li et al. successfully developed a hydrogen etching process by applying mixed gas of 5% hydrogen and 95% argon to chemically react with the SiC surface at around  $1500^\circ\text{C}$  in the quartz tube of a home built RF furnace. The annealing curve was monitored via a Lab View program with optimum parameters based on numerous annealing tests. The  $H_2$  flow rate was controlled by empirical parameters. A typical 30 to 60 minutes  $H_2$  etching removes all sorts of surface defects and scratches (Fig. 3.1b). After this process, the polished sides are typically composed of atomically-flat terraces, separated by steps of half or one SiC unit cell height, as shown in Fig. 3.1b & d (note: in case of half unit cell height, it is  $5\text{\AA}$  for 4H-SiC or  $7.5\text{\AA}$  for 6H-SiC).

After  $H_2$  etching in the furnace, there are some small fine structures on each terrace

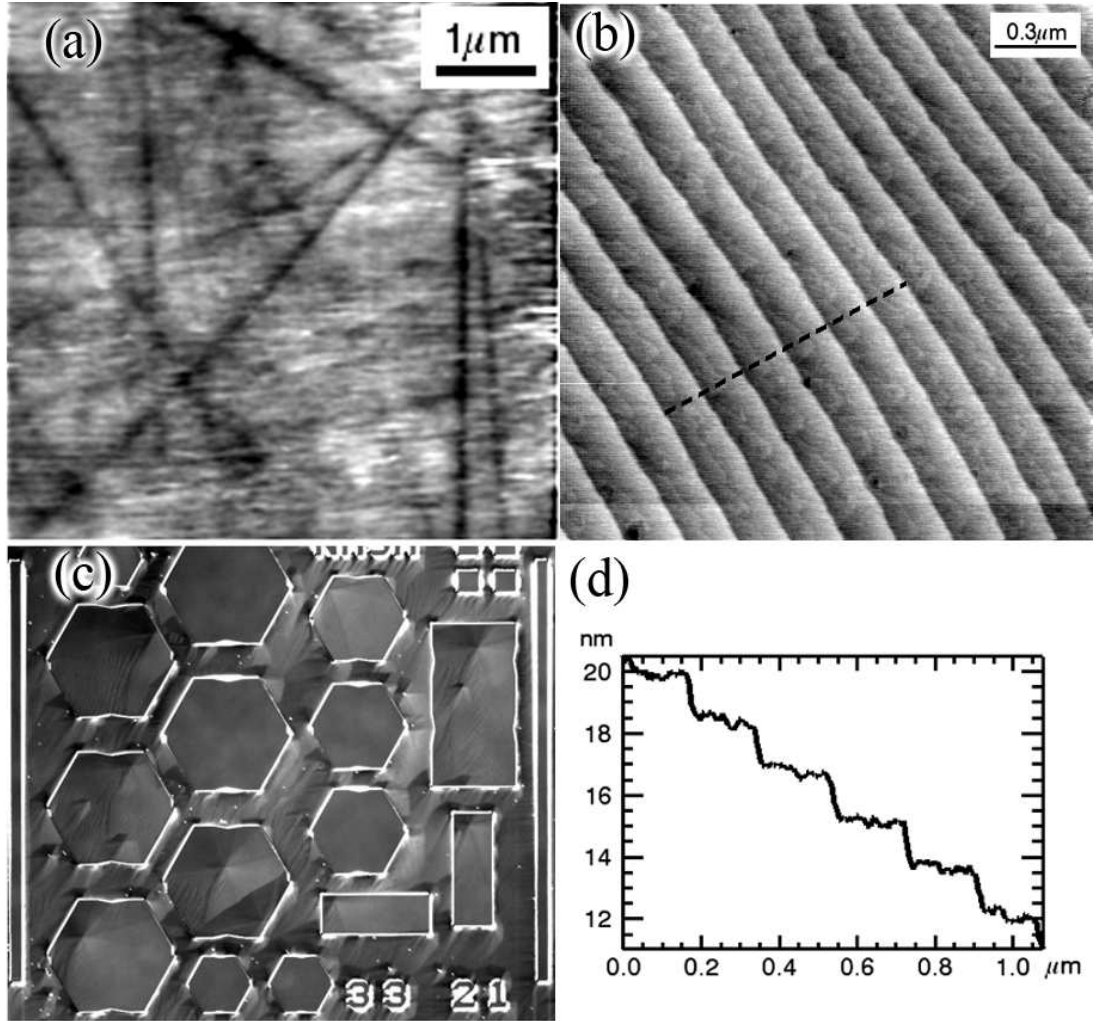


Figure 3.1: SiC surface preparation before growing graphite films. (a) AFM image on 6H-SiC Si-face of an as-received sample, full of scratches and defects. (b) After  $H_2$  etching at  $1500^\circ\text{C}$  for 30 minutes in the home built RF furnace, the surface on SiC (0001) or (000 $\bar{1}$ ) face becomes atomic flat with ordered terraces and step of one unit cell height (1.5 nm for 6H-SiC and for 1.0 nm for 4H-SiC). (c) NASA samples have been further processed with CVD growth to remove terraces and develop atomically flat surfaces on some mesas. The mesas on the surface are used to prevent the spread of intrinsic screw dislocations in SiC substrates. The image size is in  $1\text{ mm} \times 1\text{ mm}$ . (d) Profile of on terraces in Fig. (b) shows the height between terrace is half the unit cell of 6H-SiC.

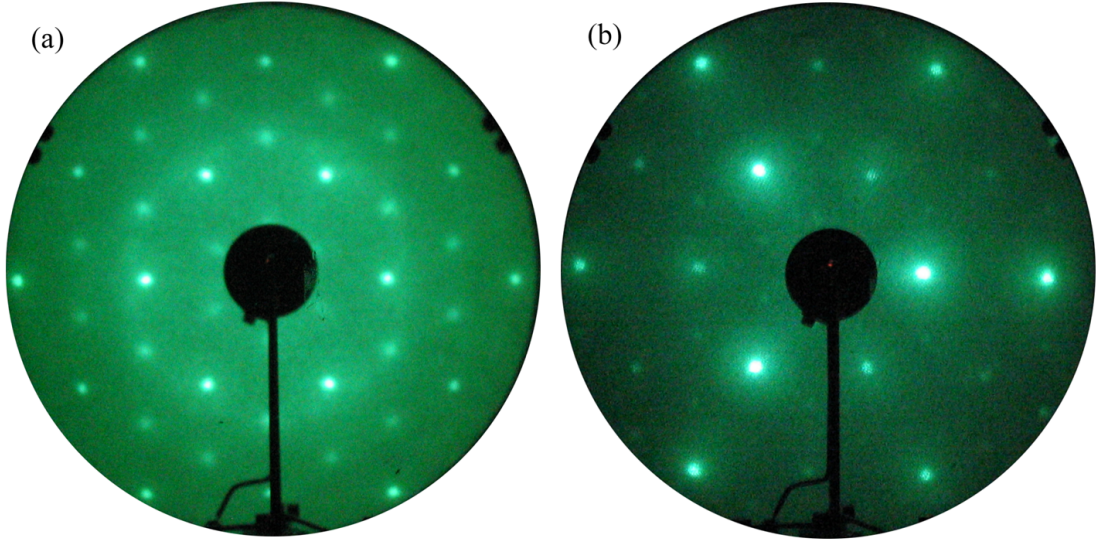


Figure 3.2: The LEED patterns on SiC (0001) surface after  $H_2$  etching before any further treatment in the UHV chamber. (a) SiC  $\sqrt{3}\times\sqrt{3}$  R30° reconstruction is always the dominant feature of  $H_2$  etched samples. A diffuse ring around the third order  $\sqrt{3}\times\sqrt{3}$  R30° spots are visible at this E-beam energy,  $E_p=169\text{eV}$ . (b) Three fold symmetry  $\sqrt{3}\times\sqrt{3}$  R30° LEED pattern, which is the evidence of uniform termination on SiC surface after  $H_2$  etching,  $E_p=197\text{eV}$ .

observable in the AFM images (Fig. 3.1b). These fine structures might relate to the origin of the diffuse ring around the third-order  $\sqrt{3}\times\sqrt{3}$  R30° LEED diffraction spots (Fig. 3.2a). Mounting these samples into the UHV chamber, we observed SiC  $\sqrt{3}\times\sqrt{3}$  R30° reconstruction LEED patterns before any further treatment in UHV. Some LEED patterns show clearly 3-fold symmetry instead of typical 6-fold symmetric  $\sqrt{3}\times\sqrt{3}$  R30° LEED pattern during the graphitization process (Fig. 3.2b), which can be explained by the termination situation mentioned in Chapter 1. If a SiC (0001) or (000 $\bar{1}$ ) surface is terminated randomly with different bulk layers, its LEED patterns should have a 6-fold symmetry, therefore the etched surface should be terminated dominantly by one type of SiC bilayer, which is probably type A bilayer [1]. According to the study of Starke et al., who used a similar  $H_2$  etching process, the etched surface is covered by a silicate monolayer, in the form of  $Si_2O_3$  [1].

The 6H-SiC samples from NASA were also made from a two-inch wafer supplied by

Cree. Besides  $H_2$  etching, NASA performed further chemical treatment to get a flatter surface without terraces. The sample was first lithographically-patterned into mesas typically  $100\text{ }\mu\text{m} \times 100\text{ }\mu\text{m}$  square and 1 to 2  $\mu\text{m}$  high (Fig. 3.1c), which was to prevent the spread of screw dislocation during heating and the CVD growth. The special screw dislocations in SiC are called micropipes, which are actually giant screw dislocation bunching up by several small screw dislocations. Micropipes are the major defect for any SiC wafer growth, and can disable any devices sitting on them [20, 58]. Mesa regions occupied  $\sim 75\%$  of the NASA sample surface. A  $1\text{ }\mu\text{m}$ -thick overlayer of 6H-SiC was deposited on the patterned surface by high-temperature chemical vapor deposition (HTCVD) with  $SiH_4$  and  $C_3H_8$  precursors. Prior to growth, samples were etched in-situ in  $H_2$  gas at  $1600^\circ\text{C}$ . These procedures have been shown to produce atomically-flat mesas by limiting the spread of micropipes [59, 60].

### 3.2 Graphitization Process

We studied the graphitization process of 3 sets of SiC samples with different preparations or different crystalline structures: a) On-axis 6H-SiC samples from NASA, prepared via the HTCVD treatment described previously. b) On-axis 4H/6H-SiC samples from Cree (vicinal cut angle less than  $0.15^\circ$ ),  $H_2$ -etched in our home-built RF furnace, which will be called “on-axis” samples. c) Off-axis 6H-SiC samples from Cree (vicinal cut angle  $3.46^\circ$ ), also  $H_2$ -etched in the RF furnace, which will be called “vicinal” samples.

Prior to acquisition of the data presented here, the NASA samples were subjected to extra graphitization and oxidization processes in our lab, as compared with other samples. The as-received NASA sample shows very faint SiC  $1 \times 1$  LEED pattern with strong diffuse background and no graphite diffraction spots were detected. A large carbon Auger peak appears on this surface. The sample was then annealed in UHV at  $1400^\circ\text{C}$  for 5 minutes and subsequently oxidized ex-situ for 15 minutes at  $780^\circ\text{C}$  and atmospheric pressure, in order to remove excess non-graphitic carbon from the surface, which is possibly from a graphite sample holder used during the HTCVD growth at NASA.

Before mounting in the UHV chamber, the samples were all ultrasonically cleaned in successive solutions of acetone and ethanol for 10 minutes each. Sample heating was done by

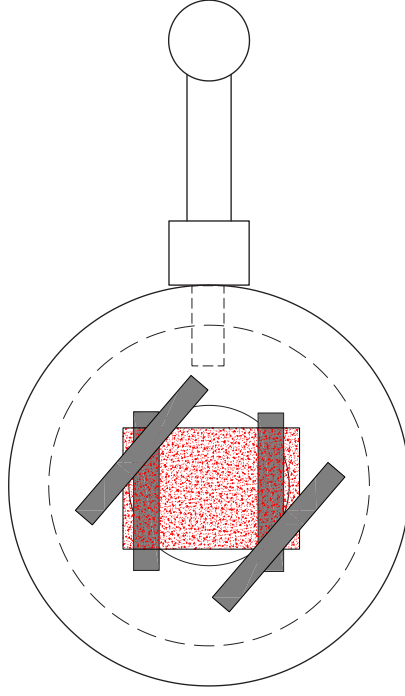


Figure 3.3: The schematic drawing of the SiC sample mounting. The sample holder is made of molybdenum. The hole in the center of the sample holder is drilled for E-beam bombardment heating. The SiC sample (red rectangle) is mounted over two tantalum sheets as a bridge. Another two tantalum sheets are spot-welded on top pinching tightly on the two diagonal corners of the sample.

electron-bombardment of the back side of the sample. The hole of the molybdenum sample holder is often a little bit bigger than the sample, therefore samples are usually mounted as a bridge over the two thin tantalum sheets (0.25 mm thick) and held to the sample holder via two other spot-welded tantalum tabs (Fig. 3.3). Temperature was measured on the corner of the sample which is on the tantalum sheets but not exposed to the E-beam directly, so that the emission of the heater filament does not affect the measurement with the optical pyrometer. The optical pyrometer was calibrated to the melting point of gold in another UHV chamber.

It has been demonstrated that heating 4H/6H-SiC(0001) samples in UHV results in depletion of silicon from the surface, with the development of several reconstructions, culminating in the formation of a thin graphite film [37, 39, 61]. As temperature increases from 800° C to 1400° C, the silicate layer is first removed since 950° C and typical reconstructions observed are  $\sqrt{3}\times\sqrt{3}$  R30°, and  $6\sqrt{3}\times 6\sqrt{3}$  R30° at sufficiently high temperature



[37, 39, 62]. Further annealing to above 1700° C results in multilayer graphite growth on the (0001) surface and carbon nanocaps or nanotubes on the (000 $\bar{1}$ ) surface [40, 41]. A slightly different series of reconstructions is observed when heating in the presence of a silicon flux [63–65]. In this case, a silicon-rich  $3\times 3$  reconstruction phase is always observed, which has been explained in a dimer adatom stacking fault (DAS) model [63], a modified DAS model [66], and the twisted reconstruction model [2]. Other phases like SiC  $2\sqrt{3}\times 2\sqrt{13}$  and Si  $7\times 7$  can be obtained by altering annealing temperature and Si flux [21].

### 3.2.1 SiC $\sqrt{3}\times\sqrt{3}$ R30° and $3\times 3$ Reconstruction

In the absence of silicon flux, the first phase after oxygen removal is  $\sqrt{3}\times\sqrt{3}$  R30° reconstruction forming near 1100° C [38, 63]. Well-ordered  $\sqrt{3}\times\sqrt{3}$  R30° adatoms could either take  $T_4$  or  $H_3$  sites (Fig. 3.4). The  $T_4$  model means the adatoms occupy the four-fold coordinated sites above second layer atoms and the  $H_3$  model indicates that adatoms sit on the hollow sites above the fourth layer atoms [21, 63, 64, 67]. The  $T_4$  was proposed to be the most likely positions for a Si rich  $\sqrt{3}\times\sqrt{3}$  R30° surface [67]. X-ray diffraction results from Coati et al. [68] and n-beam RHEED results from Xie et al. [9] are consistent with theoretical expectations [63, 64, 67] for a  $T_4$  adatom model of the reconstruction. Ramachandran et.al discovered that the filled state and empty state STM images both are localized in the same spatial area, supporting a silicon adatom model which predicts a Mott-Hubbardtype density of states [69]. In Sec. 3.5, we know that further annealing of the  $\sqrt{3}\times\sqrt{3}$  R30° surface to higher temperature will disorder the regular  $\sqrt{3}\times\sqrt{3}$  R30° reconstruction and result in a more complicated reconstruction, where the spacing between adatoms are still close to the spacing of  $\sqrt{3}\times\sqrt{3}$  R30° reconstruction, but the unit cell should be redefined as SiC  $6\sqrt{3}\times 6\sqrt{3}$  R30° reconstruction (Sec. 3.5). Both  $T_4$  and  $H_3$  positions can be occupied by adatoms in the SiC  $6\sqrt{3}\times 6\sqrt{3}$  R30° reconstruction layer between graphene films and SiC substrates (See Fig. 3.18b).

With a Si flux, the evaporation process of Si atoms can be better controlled. A  $3\times 3$  reconstruction are always observable phase with a Si flux, which is from a Si adlayer on the top of the terminal SiC bilayer resulting a Dimer Adatom Stacking (DAS) fault analogous



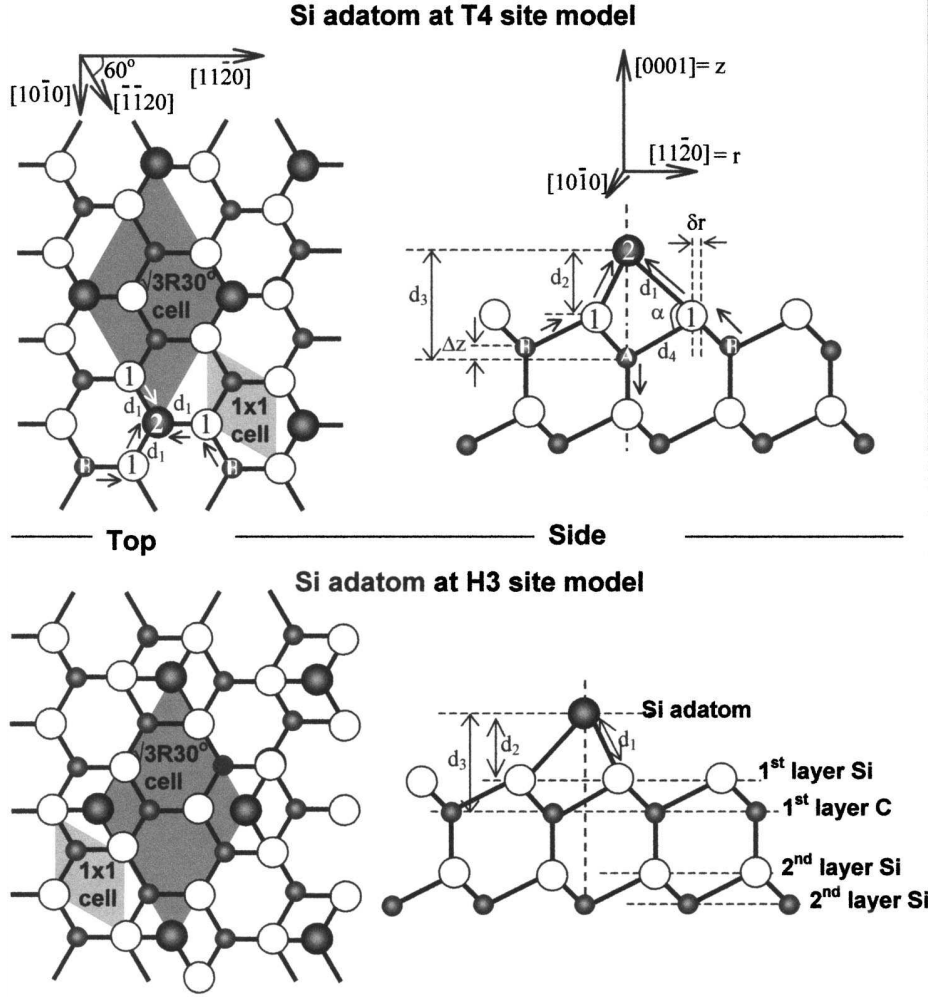


Figure 3.4: Top and side views Si adatom model of the  $\sqrt{3} \times \sqrt{3} R30^\circ$  reconstruction for  $T_4$  and  $H_3$  positions. This figure is after Ref. [9].

to the silicon  $7 \times 7$  reconstructions [2, 63].

### 3.2.2 SiC $6\sqrt{3} \times 6\sqrt{3} R30^\circ$ and the Conventional Explanations

A  $6\sqrt{3} \times 6\sqrt{3} R30^\circ$  LEED pattern is always observed in the evolution from  $\sqrt{3} \times \sqrt{3} R30^\circ$  reconstruction to graphite  $1 \times 1$  reconstruction on SiC(0001) surface. The interpretation of the  $6\sqrt{3} \times 6\sqrt{3} R30^\circ$  SiC LEED pattern is still controversial due to its complexity. Van Bommel et al. first proposed the explanation of SiC  $6\sqrt{3} \times 6\sqrt{3} R30^\circ$  reconstruction LEED pattern with double scattering, which assumes monocrystalline graphite growth directly on the SiC(0001) surface [37, 39]. Instead of using double scattering, Owman et al. suggested

that a mixture of  $\sqrt{3}\times\sqrt{3}$  R30°, 2.1×2.1 R30°, 5.3×5.3, 6.2×6.2 reconstructions forming before the initial growth of the graphene layer is the origin of  $6\sqrt{3}\times6\sqrt{3}$  R30° LEED pattern [61]. Our results support the reconstruction explanation, but the reconstruction we construct to explain the  $6\sqrt{3}\times6\sqrt{3}$  R30° LEED pattern is different from Owman's proposal. We believe the structure factor of a  $6\sqrt{3}\times6\sqrt{3}$  R30° reconstruction layer between graphite films and SiC is the main reason for the SiC  $6\sqrt{3}\times6\sqrt{3}$  R30° LEED pattern.

Details of the formation of the initial graphite layer are also controversial. Subsequent scanning tunneling microscopy (STM) measurements [61, 70, 71] showed that the graphite surface is modulated with a period that can be characterized as 6×6 relative to the underlying SiC (but note that the graphite modulation can be commensurate with the SiC lattice only over the  $6\sqrt{3}\times6\sqrt{3}$  R30° unit cell). The 6×6 superstructure from STM has three interpretations: 1) It is a Moiré pattern of incommensurate graphite monolayer on the perturbed substrate grown on the SiC(0001) surface, which was explained with the first principles pseudofunction (PSF) model by Tsai et al. [70]. 2) It is an intrinsic substrate reconstruction [61, 71]. 3) It is from the carbon nanomesh structure, which was identified by Chen et al. through comparing the DFT calculation and the STM images on SiC(0001) surface [72].

Whether the initial graphite layer constructs directly on SiC substrate or a transition interface exists between the graphene and SiC substrate is still unclear. Evidences from other research groups show that  $\sqrt{3}\times\sqrt{3}$  R30° Si-adatom reconstruction remains after formation of the first graphite layer. Simon et al. proposed a correlation between the  $\sqrt{3}\times\sqrt{3}$  R30° and the  $6\sqrt{3}\times6\sqrt{3}$  R30° reconstructions based on x-ray photoelectron diffraction (XPD) and concluded that the first commensurable graphite layer should form on the  $\sqrt{3}\times\sqrt{3}$  R30° Si adatom layer [73]. Forbeaux et al., using **k**-resolved inverse photoelectron spectroscopy (KRIPES) experiments, also suggest that the growth of the first graphene sheet may be on top of adatoms characteristic of the  $\sqrt{3}\times\sqrt{3}$  R30° reconstruction [39]. Our atomic resolved STM image on the surface with one layer of graphene initially forming reveals that an interfacial layer with SiC  $6\sqrt{3}\times6\sqrt{3}$  R30° geometry does exist (Sec. 3.5), which coincides with the suggestions of Forbeaux and Simon, since the spacing of adatoms in the  $6\sqrt{3}\times6\sqrt{3}$  R30°

is very close to the  $\sqrt{3} \times \sqrt{3}$  R30° structure.

### ***3.3 Graphite Thickness Estimation with Auger Peak-To-Peak Ratio***

Graphite film properties, such as surface conductivity, magnetoresistance, and carrier mobility, are strongly related to the thickness of graphite films. We estimate the graphite thickness on SiC(0001) through the Auger peak-to-peak ratio between silicon (LVV) and carbon (KLL). This method can give us a quantitative idea about the average graphite film thickness within the Auger electron beam area.

#### **3.3.1 Auger Attenuation Model**

If we assume at the Auger peak in the  $N(E)$  curve is Gaussian, then the peak-to-peak ratio in the  $dN(E)/dE$  spectrum is proportional to the emission current of Auger electrons [45]. Thus a measurement of the Si:C intensity ratio allows us to estimate the thickness of the graphite film, using the inelastic mean free paths (IMFP) of electrons in graphite and SiC with energy of 92 eV, 271 eV and 3 keV [74–76], we can calculate the attenuation of electrons at each atom layer on graphitized SiC and therefore the thickness dependence of Si (KLL) to C (LVV) Auger intensities. We assumed three different possible graphitized surfaces: 1) A single layer of  $6\sqrt{3} \times 6\sqrt{3}$  R30° reconstruction with Si adatoms between the graphite film and SiC, 2) the same layering but with C adatoms in the reconstruction layer, and 3) a graphite film grown directly on the bulk terminated Si-face of SiC. Fig. 3.5 shows a schematic of the model.

Two parameters are considered in our attenuation model,

a.) Mean Free Path  $\lambda$ . The inelastic mean free paths of different Auger electrons are obtained from references [74–76]. Since we consider the attenuation by layers of atoms, we converted the IMFP unit to number of layers in Table 3.1.

b.) CMA angle. For our instrument, the angle between the normal of the sample surface and the direction of outgoing Auger electrons that can be collected by the CMA is 42.2°. This lengthens the outgoing electron path by  $1/\cos(42.2^\circ)$  in the sample. Equivalently, we can consider the IMFP to be shorter by a factor  $\cos(42.2^\circ)$ , which is already considered in

Table 3.1: Mean free paths of electrons at different layers.

Cases	Symbols	Number of layers	Descriptions
1	$\lambda_{3kV,G}$	19.42	IMFP of 3 keV electrons in Graphite layers
2	$\lambda_{3kV,Si}$	29.3	IMFP of 3 keV electrons in Silicon layers of SiC
3	$\lambda_{3kV,C}$	58.30	IMFP of 3 keV electrons in carbon layers of SiC
4	$\lambda_{92V,G}$	2.079	IMFP of 92 eV electrons in Graphite layers
5	$\lambda_{92V,Si}$	2.794	IMFP of 92 eV electrons in Silicon layers of SiC
6	$\lambda_{92V,C}$	6.238	IMFP of 92 eV electrons in carbon layers of SiC
7	$\lambda_{272V,G}$	4.230	IMFP of 272 eV electrons in Graphite
8	$\lambda_{272V,Si}$	6.322	IMFP of 272 eV electrons in Silicon layers of SiC
9	$\lambda_{272V,C}$	12.69	IMFP of 272 eV electrons in carbon layers of SiC

Table 3.1.

### 3.3.2 Auger Peak-to-peak Ratio Calculation

Here, in order to simplify the expression, we use the attenuation factor  $\alpha$  in each monolayer to replace IMPF and let  $\alpha = 1/\lambda$ . The attenuation of the incident E-beam and outgoing Auger electron depends on the atom types and densities in each layer. If there are  $n$  graphite ML layers growth on the surface and the carbon Auger electron current from top graphite (1st) layer is  $I_{G,1}$ , we know that the Auger current from the “ $m$ th” layer graphite is

$$I_{G,m} = I_{G,1} \exp[(-m)(\alpha_{3kV,G} + \alpha_{271V,G})] \quad (3.1)$$

therefore the overall carbon auger current from  $n$  layers graphite is

$$I_{graphite}^{carbon} = \sum_{m=1}^n I_{G,m} = \frac{1 - \exp[(-n) \times (\alpha_{3kV,G} + \alpha_{272V,G})]}{1 - \exp[(-1) \times (\alpha_{3kV,G} + \alpha_{272V,G})]} \quad (3.2)$$

In a typical quantitative analysis for a homogeneous mixture  $AB$ , the component mole fractions and Auger current are related:

$$\frac{x_A}{x_B} = F_{AB}^A \cdot \frac{I_A/I_A^0}{I_B/I_B^0} \quad (3.3)$$

where  $x_A$  and  $x_B$  are the mole fraction of each components,  $F_{AB}^A$  is the Auger electron backscattering matrix factor, and  $I_A^0$  and  $I_B^0$  are the relative elemental sensitivity factors

## Schematic of Auger Attenuation

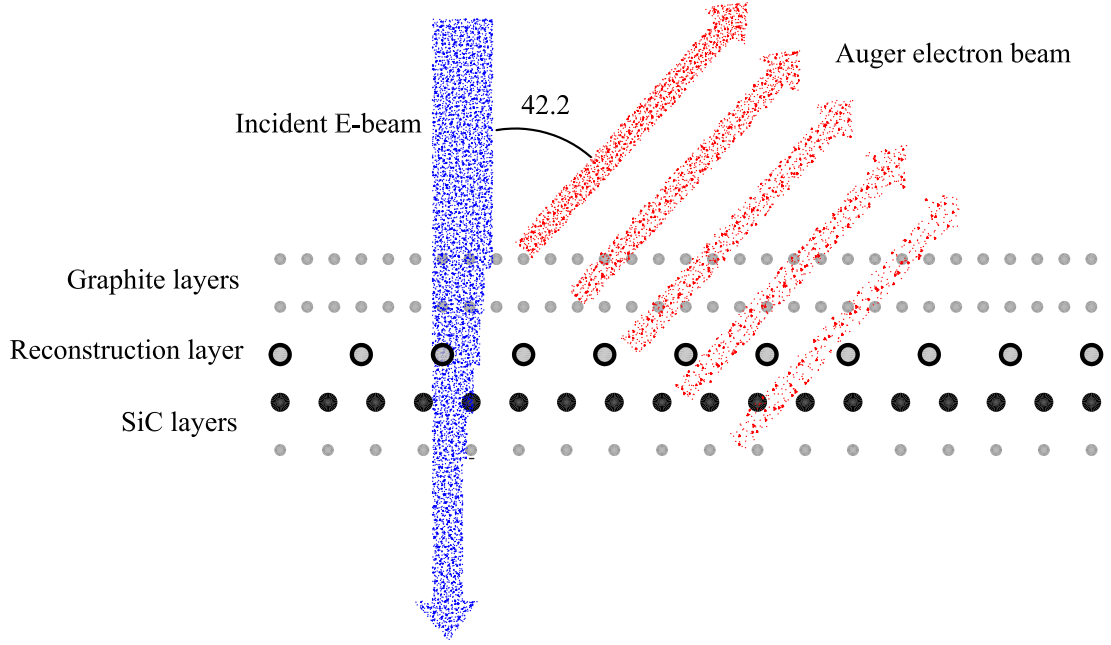


Figure 3.5: The schematic drawing of the Auger attenuation model on graphitized SiC(0001) surface. The atom number on each layer is drawn to be proportional to real number of atoms on each layer. The reconstruction layer can be all carbon or silicon atoms, or a mixture of them. The sum of the attenuation factors of Si and C are calculated with the Matlab code. The attenuation induced by both incident E-beam and outgoing Auger electron beam is considered. The incident beam is normal to the surface and the CMA Auger electron collecting angle is  $42.2^\circ$  from the normal of the surface, therefore an extra angle factor  $\cos(42.2^\circ)$  is considered for the IMFP in Tab. 3.1.

of  $A$  and  $B$  [45]. When considering layer by layer stacking model on SiC(0001) surface, equation 3.3 still hold by considering the attenuation of electron beams on each layer.

Our STM results indicate that at least one SiC  $6\sqrt{3}\times 6\sqrt{3}$  R30° reconstruction layer exists between graphite film and SiC substrate. The components of this layer can be either all Si or all C atoms, or a mixture of both. Therefore the calculation of three cases was conducted: I) The graphite films are grown directly on the Si-face of SiC, i.e. no reconstruction layer between the top layer of SiC and the bottom layer of graphite. II) One  $6\sqrt{3}\times 6\sqrt{3}$  R30° layer of silicon atoms exist between graphite films and the Si-face of SiC. III) One layer  $6\sqrt{3}\times 6\sqrt{3}$  R30° carbon atoms exist between graphite films and the Si-face of SiC.

For case I, we suppose there are still  $n$  graphite ML layers growth on the surface and the carbon Auger electron current from top graphite (1st) layer is still  $I_{G,1}$ . Therefore the silicon Auger electron current from top silicon (1st) layer in SiC is

$$I_{Si,1} = I_{G,1} \times \exp[(-n)(\alpha_{3kV,G} + \alpha_{92,G})] \frac{I_{Si}^0}{I_C^0} \frac{x_{Si}}{x_G} \frac{1}{F_{Si,G}^{Si}} \quad (3.4)$$

where the mole fraction ratio between one layer Si in SiC bulk and one layer graphite is 1:3.1 and the sensitivity factor ratio between Si and C is  $I_{Si}^0/I_C^0 = 3.5/2$ . The factor  $F_{Si,G}^{Si}$  is  $(1 + r_{Si})/(1 + r_C) \approx 1.2$ , where  $r_{Si}$  and  $r_C$  are the backscattering terms [45]. we know that the Auger current from the “ $m$ th” Si layer in SiC is

$$I_{Si,m} = I_{Si,1} \times \exp[(1 - m)(\alpha_{3kV,Si} + \alpha_{92eV,Si} + \alpha_{3kV,C} + \alpha_{92eV,C})] \quad (3.5)$$

therefore the overall Si Auger current from SiC bulk is as follows:

$$I_{SiC}^{silicon} = \sum_{m=1}^{\infty} I_{Si,m} = I_{Si,1} \times \frac{1}{1 - \exp[(-1) \times (\alpha_{3kV,Si} + \alpha_{3kV,C} + \alpha_{92V,Si} + \alpha_{92V,C})]} \quad (3.6)$$

Likewise, the Auger electron current from the first carbon layer in SiC is

$$I_{C,1} = I_{G,1} \times \exp[(-n)(\alpha_{3kV,G} + \alpha_{92,G}) - \alpha_{3kV,Si} - \alpha_{272eV,C}] \frac{I_C^0}{I_C^0} \frac{x_C}{x_G} \frac{1}{F_{C,G}^C} \quad (3.7)$$

where the mole fraction ratio between one layer of C in SiC bulk and one graphene is 1:3.1. The sensitivity ratio and the factor  $F_{C,G}^C$  are both 1. Therefore we know that the Auger current from the “ $m$ th” C layer in SiC is

$$I_{C,m} = I_{C,1} \times \exp[(1 - m)(\alpha_{3kV,Si} + \alpha_{272eV,Si} + \alpha_{3kV,C} + \alpha_{272eV,C})] \quad (3.8)$$

therefore the overall C auger current from SiC bulk is as follows:

$$I_{SiC}^{carbon} = \sum_{m=1}^{\infty} I_{C,m} = I_{C,1} \times \frac{1}{1 - \exp[(-1) \times (\alpha_{3kV,Si} + \alpha_{3kV,C} + \alpha_{92V,Si} + \alpha_{92V,C})]} \quad (3.9)$$

The final Si:C Auger peak-to-peak ratio we obtained in the Auger spectroscopy is

$$Si : C = \frac{I_{SiC}^{silicon}}{I_{graphite}^{carbon} + I_{SiC}^{carbon}} \quad (3.10)$$

For case II, the situation in graphite layers does not change. The atom density of the interface layer is about 1/3 of that one SiC atom layer, since the atom density of the interfacial layer is close to the atom density of one SiC  $\sqrt{3} \times \sqrt{3}$  R30° layer. So the IMFP of this interfacial layer is 3 times of that of one layer Si atoms in SiC.

We still suppose there are  $n$  layer graphite on top and the carbon Auger electron current from top graphite (1st) layer is still  $I_{G,1}$ . Therefore, the contribution from one layer  $6\sqrt{3} \times 6\sqrt{3}$  R30° interface layer with only Si atoms is,

$$I_{interface}^{silicon} = \frac{1}{3} \times I_{G,1} \times \exp[(-n)(\alpha_{3kV,G} + \alpha_{92,G})] \frac{I_{Si}^0}{I_C^0} \frac{x_{Si}}{x_G} \frac{1}{F_{Si,G}^{Si}} \quad (3.11)$$

Considering attenuation of this reconstruction layer, the Auger current contribution from top silicon layer of SiC bulk is modified as follow,

$$I_{Si,1} = I_{G,1} \times \exp[(-n)(\alpha_{3kV,G} + \alpha_{92,G}) - \alpha_{3kV,Si}/3 - \alpha_{92,Si}/3] \frac{I_{Si}^0}{I_C^0} \frac{x_{Si}}{x_G} \frac{1}{F_{Si,G}^{Si}} \quad (3.12)$$

Likewise, the Auger electron current from the first carbon layer is

$$I_{C,1} = I_{G,1} \times \exp[(-n)(\alpha_{3kV,G} + \alpha_{92,G}) - \frac{4}{3} \times (\alpha_{3kV,Si} + \alpha_{272eV,Si})] \frac{I_C^0}{I_C^0} \frac{x_C}{x_G} \frac{1}{F_{C,G}^C} \quad (3.13)$$

The Auger current equations from all the Si layers and the carbon layers in SiC bulk still follows Equ. 3.6 and Equ. 3.9.

The final Si:C Auger peak-to-peak ratio we obtained in the Auger spectroscopy is

$$Si : C = \frac{I_{SiC}^{silicon} + I_{interface}^{silicon}}{I_{graphite}^{carbon} + I_{SiC}^{carbon}} \quad (3.14)$$

In case III, we only need to replace the attenuation factor of Si for the interface layer in case II with the corresponding attenuation factor of C for the interface layer, then we can get the Si and C Auger peak intensity ratio as in Case II.

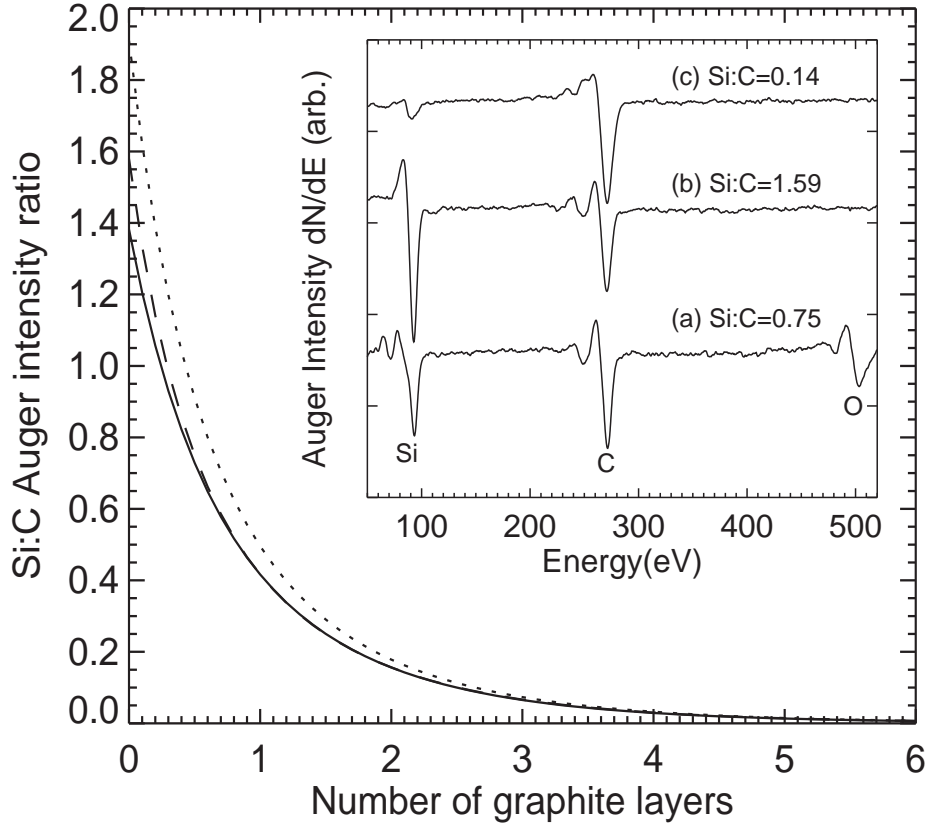


Figure 3.6: Graphite film thickness estimation and Auger evolution of annealing SiC(0001) in UHV. The solid line represents the estimation with the model that one layer carbon  $6\sqrt{3} \times 6\sqrt{3}$  R30° atoms exist between graphite films and the Si-face of SiC (note: the attenuation of the  $6\sqrt{3} \times 6\sqrt{3}$  R30° layer is the same to a  $\sqrt{3} \times \sqrt{3}$  R30° layer). The dash line represents the estimation with the model that the graphite films are grown directly on the Si-face of SiC, i.e. no reconstruction layer between the top layer of SiC and the bottom layer of graphite. The dotted line represents the estimation with the model that one layer silicon  $6\sqrt{3} \times 6\sqrt{3}$  R30° atoms exist between graphite films and the Si-face of SiC. The solid line represents the estimation with the model that one layer carbon  $6\sqrt{3} \times 6\sqrt{3}$  R30° atoms exist between graphite films and the Si-face of SiC. The inset figure show Auger curves corresponding to different SiC(0001) surface reconstructions when annealing SiC in UHV. (a) SiC(0001) surface after  $H_2$  etching. (b) SiC(0001) surface annealed up to 1150° C with SiC  $\sqrt{3} \times \sqrt{3}$  R30° reconstruction on surface. (c) Graphitized SiC(0001) surface annealed up to 1350° C with SiC  $6\sqrt{3} \times 6\sqrt{3}$  R30° reconstruction on surface.



The calculation following the formulas above was conducted with Matlab. Corresponding to the three cases, three curves with relative Auger intensities versus the number of graphene layers are shown in Fig. 3.6. The Auger curves evolution taken from  $H_2$  etched SiC(0001) surface to the graphitized SiC surfaces is included in the inset of Fig. 3.6, from which we can see the growth of graphitic Auger peaks and decreasing of the Si Auger peaks with increasing annealing temperature.

We assume the thickness of the graphite films on surface is uniform in this calculation. However, STM images show that the thickness varies from domain to domain on the graphitized surface (Fig. 3.11a). According to the simulation, we can not track films thicker than 6 layers, since the relative Auger peak height ratio is less than 1% in that case, so it is hard to estimate the thickness of graphite films on the C-face of SiC, which often involves  $8 \sim 30$  graphene layers.

### 3.4 *On-axis SiC Samples*

#### 3.4.1 LEED Results and Discussion

The evolution of the LEED patterns in the graphitization process was studied by increasing annealing temperature from  $1000^\circ\text{C}$  gradually to  $1450^\circ\text{C}$  through 27 annealing cycles on a NASA sample. Auger electron spectra (AES) and LEED patterns were recorded for each annealing cycle. Numerous LEED experiments carried out with other sets of SiC samples proved that every LEED pattern phase evolution from SiC  $1 \times 1$  to graphite  $1 \times 1$  can be reproduced. The temperature is the dominant factor determining the thickness of graphite films. The exact LEED pattern can be reproduced on the (0001) faces of any SiC sample by monitoring the annealing temperature and time.

When the sample is annealed at  $1100^\circ\text{C}$  for 3 minutes, the first LEED patterns on the NASA sample transit from disordered oxidized surface to SiC  $\sqrt{3} \times \sqrt{3} \text{R}30^\circ$  reconstruction. At this phase, oxygen on surface is totally removed. For other  $H_2$  etched samples, the surface transition at this temperature is from a SiC  $\sqrt{3} \times \sqrt{3} \text{R}30^\circ$  pattern with strong diffuse (Fig. 3.2) to sharp SiC  $\sqrt{3} \times \sqrt{3} \text{R}30^\circ$  spots (Fig. 3.7a) without diffuse. As described in previous text, the  $\sqrt{3} \times \sqrt{3} \text{R}30^\circ$  pattern after  $H_2$  etching is from the silicate layer, which

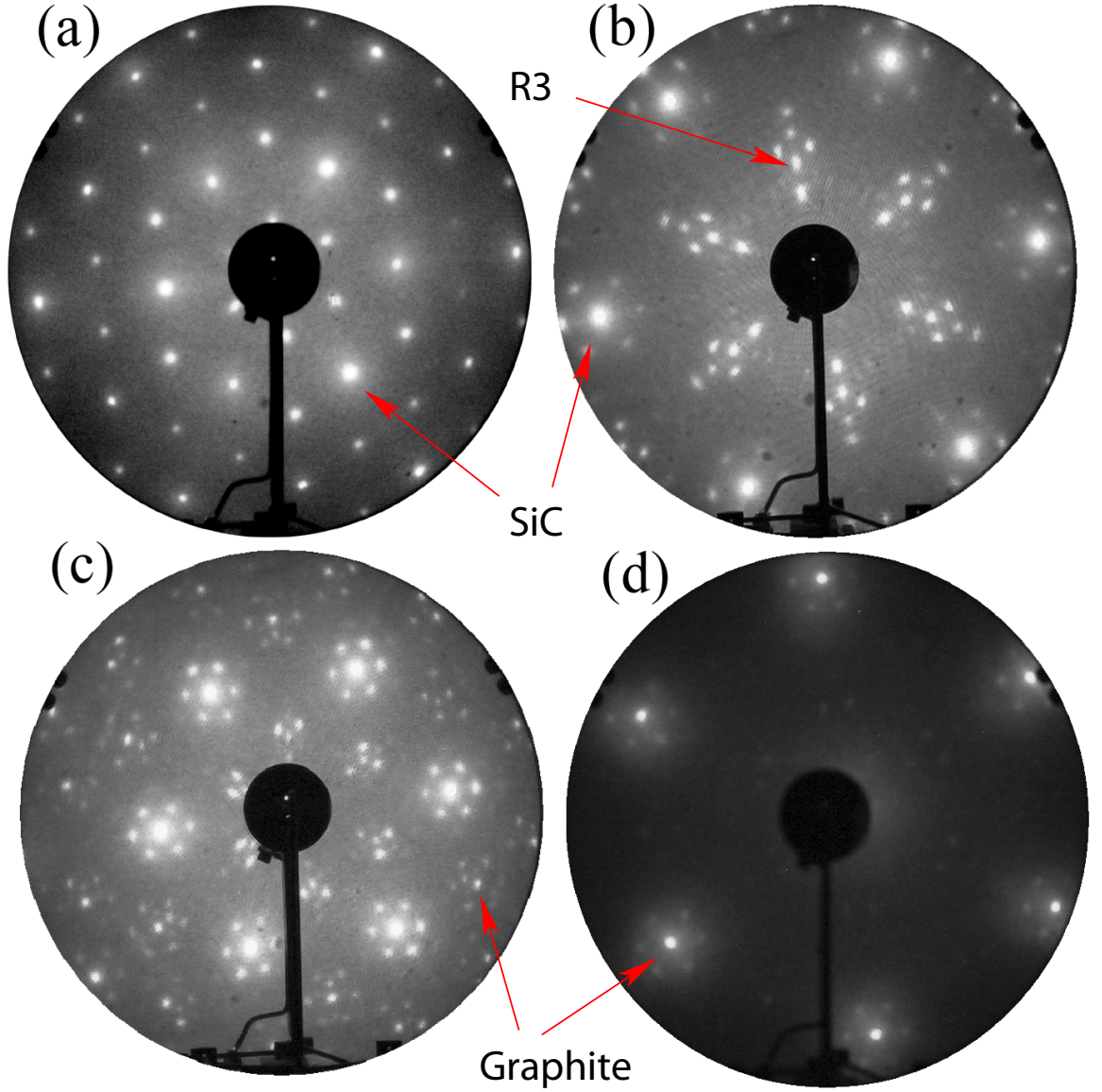


Figure 3.7: The evolution of the LEED patterns on SiC(0001) surface. (a) SiC  $\sqrt{3} \times \sqrt{3} R30^\circ$   $E_p=180$  eV. The first phase acquired after annealing in UHV above  $1100^\circ\text{C}$ . (b) Monolayer graphite on SiC(0001),  $6\sqrt{3} \times 6\sqrt{3} R30^\circ$ ,  $E_p=49$  eV. The  $\sqrt{3} \times \sqrt{3} R30^\circ$  spots are labeled with R3 in the figure and coexist with the  $6\sqrt{3} \times 6\sqrt{3} R30^\circ$  spots at this phase. (c) Monolayer graphite on SiC(0001),  $6\sqrt{3} \times 6\sqrt{3} R30^\circ$ ,  $E_p=109$  eV. The diffraction spots show that the graphene sheets register epitaxially with the underlying SiC(0001) surface and have  $30^\circ$  rotation. (d) Thick graphite on SiC(0001), graphite  $1 \times 1$ . Graphite spots with their satellites are observable. SiC spots are very weak.  $E_p=78$  eV.

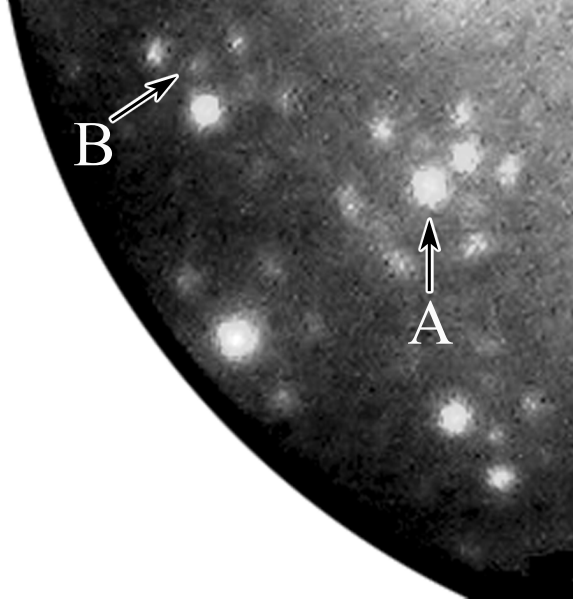


Figure 3.8: Expanded view of the lower-left corner of Fig. 3.7d. Arrow A points to the graphite diffraction spot and arrow B points at a  $\sqrt{3}\times\sqrt{3}$  R30° spot. The fine diffraction pattern around the 4th-order  $\sqrt{3}\times\sqrt{3}$  R30° is visible.

will presents an oxygen Auger peak, while the  $\sqrt{3}\times\sqrt{3}$  R30° pattern after annealing is from Si adatoms on  $T_4$  or  $H_3$  sites and has no associated oxygen Auger peak (Fig. 3.6). This  $\sqrt{3}\times\sqrt{3}$  R30° pattern turns into a SiC  $1\times 1$  pattern after the sample is kept in the UHV chamber for more than 16 hours. The Si-rich  $3\times 3$  phase was not observed in this work, since no external Si deposition source was employed. When the sample was annealed to 1200°C, the graphite integer-order LEED spots developed, as well as many other spots falling on the  $6\sqrt{3}\times 6\sqrt{3}$  R30° reciprocal mesh. The well-defined LEED patterns in Figs. 3.7b and 3.7c provide a good overview of the  $6\sqrt{3}\times 6\sqrt{3}$  R30° diffraction spots (see also Fig. 3.9). At the stage where  $\sqrt{3}\times\sqrt{3}$  R30° and  $6\sqrt{3}\times 6\sqrt{3}$  R30° diffraction spots coexist, many fine LEED structures are useful for finding the origins of these diffraction spots (Fig. 3.8). When the sample was annealed up to 1450°C, we observed LEED patterns dominated by graphite  $1\times 1$  spots which are still surrounded by weak  $6\times 6$  satellites, as shown in Fig. 3.7d.

Another on-axis sample prepared with the typical  $H_2$  etching method was annealed in the UHV chamber at 1250°C for 3 mins (Fig. 3.9). A  $6\sqrt{3}\times 6\sqrt{3}$  R30° LEED pattern with

maximum number of diffraction spots are obtained at this phase. The Auger Si and C peak-to-peak ratio is about the 1:3, which means that on average one monolayer graphene develop on the surface according our Auger model. At this phase, the  $\sqrt{3} \times \sqrt{3} \text{R}30^\circ$  diffractions spots are already extinguished, comparing with Fig. 3.7b, in which figure  $\sqrt{3} \times \sqrt{3} \text{R}30^\circ$  spots coexist with  $6\sqrt{3} \times 6\sqrt{3} \text{R}30^\circ$  spots. A distinct feature of the LEED pattern is three bright  $6\sqrt{3} \times 6\sqrt{3} \text{R}30^\circ$  spots around the first-order  $\sqrt{3} \times \sqrt{3} \text{R}30^\circ$  position. These spots exist until the graphite thickness exceeds 5 layers, at essentially the same thickness, the SiC primary spots also extinguish. We believe this  $6\sqrt{3} \times 6\sqrt{3} \text{R}30^\circ$  LEED pattern is due to the kinematic scattering from a reconstructed layer between graphite and the SiC substrate. These  $6\sqrt{3} \times 6\sqrt{3} \text{R}30^\circ$  diffraction spots never appear in the C-face graphene growth. The evidence for a  $6\sqrt{3} \times 6\sqrt{3} \text{R}30^\circ$  reconstructed interfacial layer will be discussed thoroughly in Sec. 3.5.

### 3.4.2 STM Results and Discussion

As mentioned in Chap. 1, most STM images of graphite do not have honeycomb structures but hexagon structures with unit cell length of  $2.46 \text{ \AA}$ . Differences in the local density of states (LDOS) occur as a consequence of the carbon site asymmetry for A, B atoms and the interlayer interactions [29]. Tomanek et al. observed the asymmetry of graphite with STM and found that the STM tunneling current on B atoms is relatively much larger when the tip bias is low. This A, B asymmetry decreases when the bias increases [77]. Both Honeycomb (Fig. 5.5b) and hexagon structures (Fig. 3.11b) are observed in our STM on graphitized SiC, which will be presented in the following text.

Another significant feature of STM images on HOPG is that “giant” graphite hexagonal symmetry with different lattice constants is always observable [29, 78]. Xhie et.al attribute the giant hexagonal structures to the Moire patterns due to the misorientation of the graphite top layer [78]. Tersoff attributes the large corrugations to linear E-k dispersion and Dirac points of the top graphene layer [79]. Another theory indicates that interaction between STM tip and soft graphite surface affects the graphite giant superstructures [80]. Graphite films grown on SiC always present SiC  $6 \times 6$  corrugation, but not other

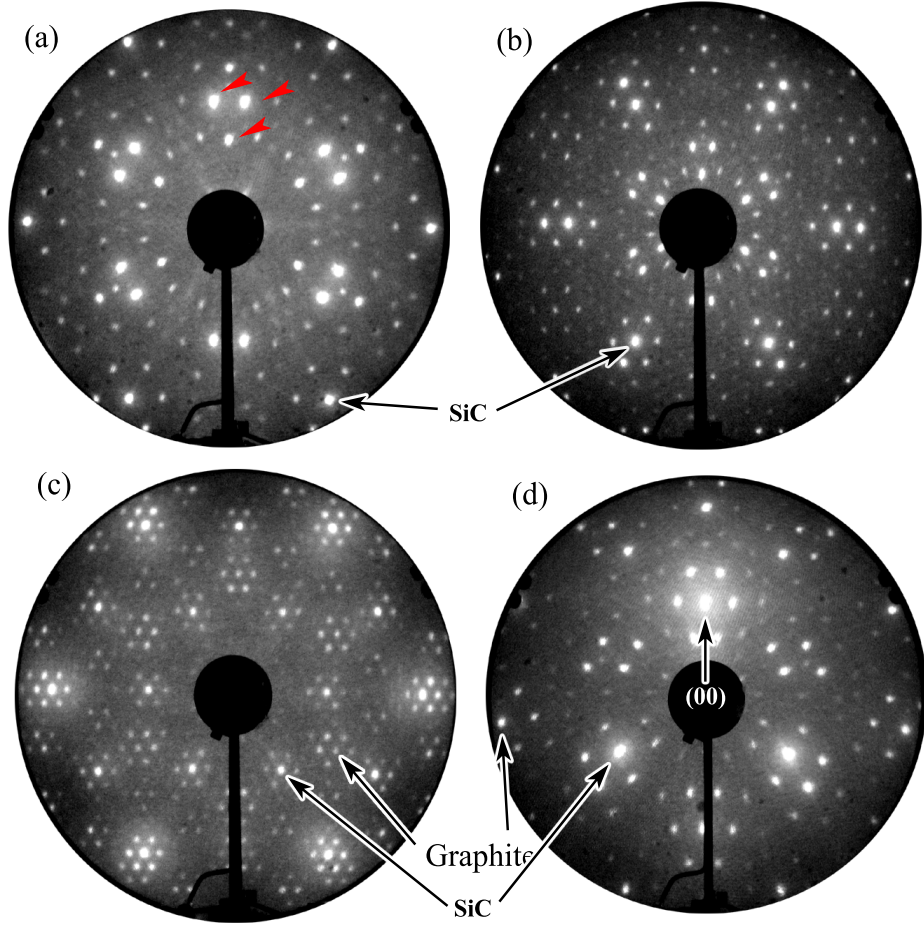


Figure 3.9: The SiC  $6\sqrt{3} \times 6\sqrt{3} R30^\circ$  reconstruction LEED patterns of monolayer graphene growth on the SiC(0001) surface. At this phase, the LEED pattern exhibits maximum number diffraction spots, which was traditionally regarded as the consequence of double scattering. However our results show that it is more related to a  $6\sqrt{3} \times 6\sqrt{3} R30^\circ$  reconstruction layer between graphite and SiC. Additionally,  $\sqrt{3} \times \sqrt{3} R30^\circ$  spots are already extinguished, which is a sign we often assume as the beginning of the initial graphene layer growth. (a) The pattern around  $\sqrt{3} \times \sqrt{3} R30^\circ \{01\}$  diffraction spots. Graphite diffraction spots are out of LEED phosphor scree at this E-beam energy. Three red arrows point at 3 “A3” spots, which are obvious much brighter than other non-primary SiC spots,  $E_p=41$  eV. (b) A higher energy photo for the pattern around SiC  $\{01\}$  and graphite  $\{01\}$ . A spot outside SiC almost has the equivalent intensity of SiC spots. The origin of this spot is not clear and we tend to think it is a also  $6\sqrt{3} \times 6\sqrt{3} R30^\circ$  structure factor effect,  $E_p=95$  eV. (c) Higher order diffraction spots, many of which can be reproduced by the kinematic scattering model,  $E_p=212$  eV. (d) LEED pattern around (00) spots obtained by titled sample  $12^\circ$ ,  $E_p=49$  eV.

size superstructure, therefore the mechanism of the corrugation is different from the above interpretations for HOPG samples. Tsai et. al proposed the disturbance of silicon dangling-bond states model in 1992 [70]. However, further STM studies show that the graphene is not constructed over SiC directly, but over reconstruction layers [61]. Our STM results also prove the existence of the reconstruction layers, but should be explained with different reconstruction structure. The STM on graphite films grown on the C-face of SiC do not have any ordered “giant” corrugation, in either thin or thick graphite film phases.

#### 3.4.2.1 *Moiré Pattern*

Graphite films grown on the SiC(0001) surface always show a constant SiC  $6\times 6$  corrugation (Fig. 3.13b & 3.11a) instead of “giant” superstructures in different sizes on HOPG [78]. One explanation of this SiC  $6\times 6$  corrugation is the Moiré pattern theory. Figure 3.10 is a schematic SiC  $6\times 6$  Moiré pattern by overlapping one layer atoms of graphene (red) over one layer of Si atoms of the SiC substrate (blue). Since the graphene layer has higher atom density, the SiC atoms are plotted on top for clarity. Although the unit cell of the lattices should still be defined to be  $6\sqrt{3}\times 6\sqrt{3}$  R $30^\circ$  as the large black rhombus indicates in Fig. 3.10, the periodicity of the lattice coincidence is SiC  $6\times 6$ . Since we have known the graphite films are constructed on a SiC  $6\sqrt{3}\times 6\sqrt{3}$  R $30^\circ$  layer with SiC  $6\times 6$  periodic corrugation, we believe the graphite corrugation is due to its interaction with this reconstruction layer. The satellites of graphite and STM/STS results (Sec. 3.5) prove that the corrugation of graphite substantially exists by not completely from the dangling bonds of silicon underneath as Tsai et. al proposed [70].

#### 3.4.2.2 *STM Results on Thick Graphite Films*

Corresponding to the LEED pattern of Fig, 3.7d, a STM image from the NASA sample is acquired in Fig. 3.11a. The image was taken after the sample was annealed for the first 24 cycles as described in Sec. 3.4.1. The parameters used for the final annealing before STM was a 8 mins E-beam heating at  $1400^\circ\text{C}$  in UHV. The Auger ratio shows that the thickness of graphite is 3 to 4 layers. In contrast to the monolayer graphene growth on SiC, we call graphite films with more than 3 layers “thick” films. The image reveals a distinct  $6\times 6$



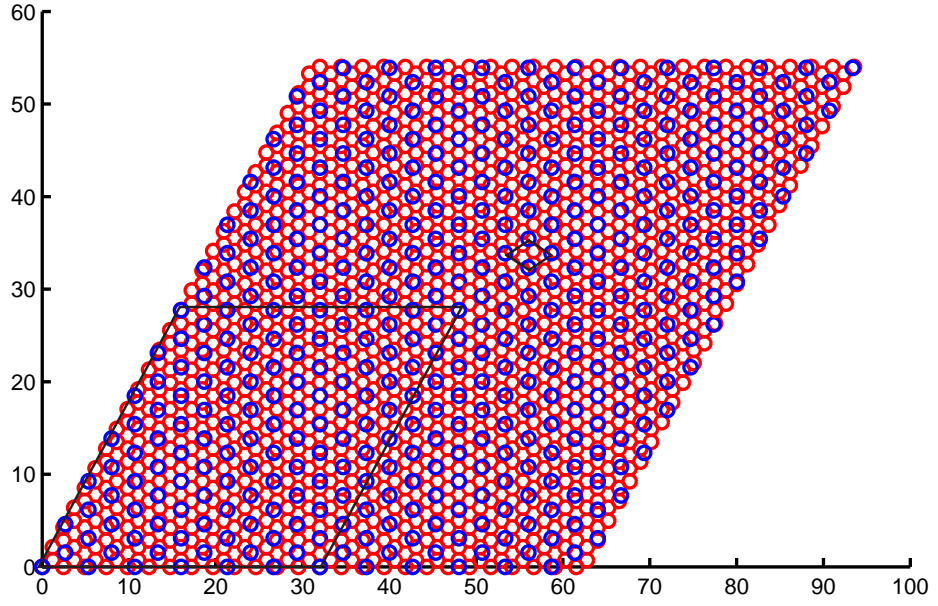


Figure 3.10: The SiC  $6 \times 6$  Moiré pattern formed by putting one layer of graphene atoms (in red) on one layer of SiC atoms (in blue). The axis units are angstroms. The periodicity follows SiC  $6\sqrt{3} \times 6\sqrt{3} \text{ R}30^\circ$  reconstruction due to the geometric relationship between the lattice constants of SiC and graphite that  $6\sqrt{3}\vec{a}_{\text{SiC}} = 13\vec{a}_{\text{Graphite}}$ . The unit cell of graphite rotates  $30^\circ$  relative to the SiC substrate unit cell. The  $6\sqrt{3} \times 6\sqrt{3} \text{ R}30^\circ$  unit cell is depicted as the big black rhombus and the SiC unitcell is presented by the small black rhombus.

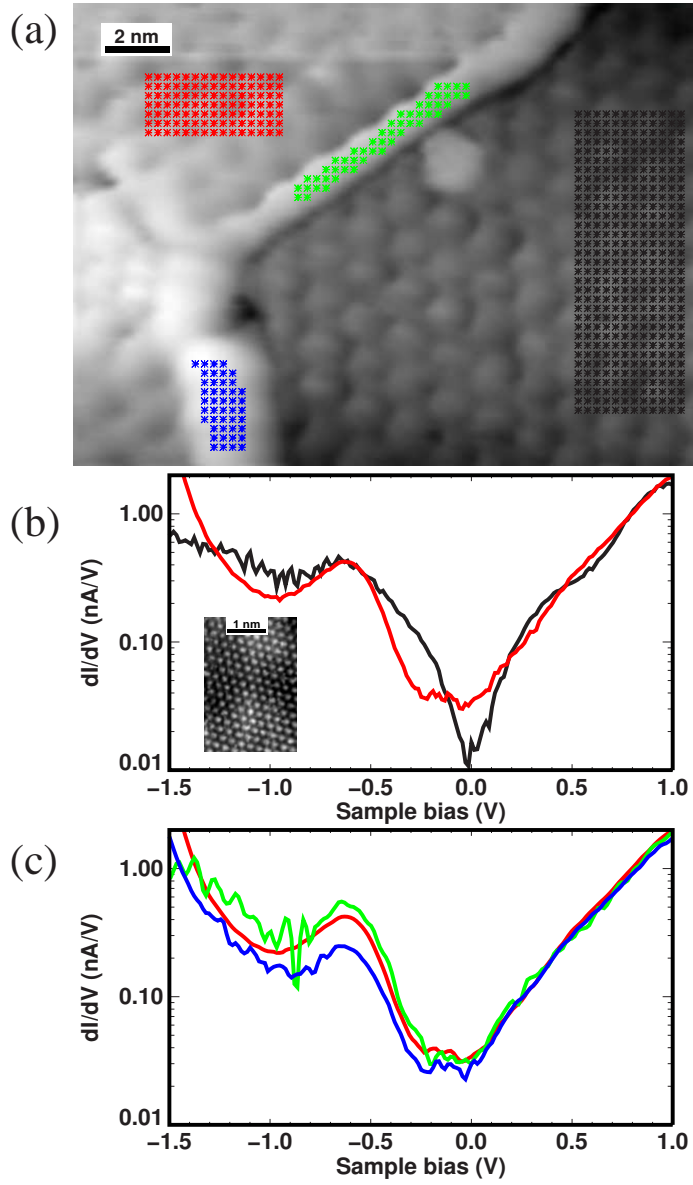


Figure 3.11: A STM image and its STS spectra of more than three graphene layers on SiC(0001) surface of a NASA sample. (a) STM image of a surface region of the graphitized SiC(0001) surface. Three domains in the figure all show SiC  $6 \times 6$  corrugation. The tip voltages was  $-0.6$  V. The constant tunneling current was  $100$  pA (b)  $dI/dV$  spectra (log scale) acquired from upper and lower regions marked with corresponding color line in the image at top. The black line is an average of 396 spectra at different positions, the red line an average of 105. With a few “glitchy” exceptions, individual spectra in each region showed negligible variation from the average  $dI/dV$  shown. Inset: Atomically resolved region (different sample, similar preparation). (c)  $dI/dV$  spectra comparison between the upper region and its boundary. Almost overlapping curves indicate that the graphite is continuous over the domain boundaries.



corrugation of the overlayer and a raised region along a step on the surface. Thick graphite corrugation will be further discussed in Sec. 3.5. LEED results confirm that the graphene sheets register epitaxially with the underlying SiC, as shown in Fig. 3.7. The mean height difference between terraces (0.25 nm), indicates that the step in Fig. 3.11a is a bilayer step in the SiC substrate. Terrace sizes (corresponding to a single  $6 \times 6$  domain) are found by STM to be up to several hundred nanometers in extent. Preliminary high resolution LEED studies indicate that the graphene layers are strained in-plane by 0.3-0.5%, with a mean structural coherence length of greater than 20 nm [11].

Also shown in Fig. 3.11b are derivative tunneling spectra ( $dI/dV$  vs  $V$ ) acquired within the respective dotted regions with different colors. The  $dI/dV$  spectrum obtained from the lower terrace (black line) is similar to that of a zero-gap semiconductor, as found typically for bulk graphite. On the upper terrace, the  $6 \times 6$  domain images somewhat differently, and the  $dI/dV$  spectrum (red line) displays a region of constant, finite conductance around the Fermi energy (zero bias). Spectral shapes are very uniform within each  $6 \times 6$  domain. The  $dI/dV$  curves show that the electronic properties of the films are not entirely homogeneous. This may relate to differing lateral registry (i.e., not orientational) of the graphite on the SiC substrate, or electron confinement within  $6 \times 6$  domains.  $dI/dV$  spectra acquired over the buckled region at the step edge are nearly identical to those found on the upper terrace (Figure 3.11c), suggesting that the graphite layer remains continuous over the step [11]. Some surfaces on this NASA sample have vacancy defects on ordered SiC  $6 \times 6$  corrugation (Fig. 3.12). It is still not clear whether graphite films on these defects are completed or not.

#### 3.4.2.3 STM on Monolayer Graphene

Another 6H-SiC on-axis sample was prepared with typical  $H_2$  etching method and annealed in the UHV chamber at 1250° C for 3 mins. The corresponding LEED is in Fig. 3.9 and the Si and C Auger peak-to-peak ratio show that the graphite thickness is about one monolayer. Corresponding STM images are presented in Figs. 3.13, 3.14a, 3.15a & b, and 3.16a. At this phase, the surface exhibits several sorts of topographies (Fig. 3.13a). From Fig. 3.13b, we

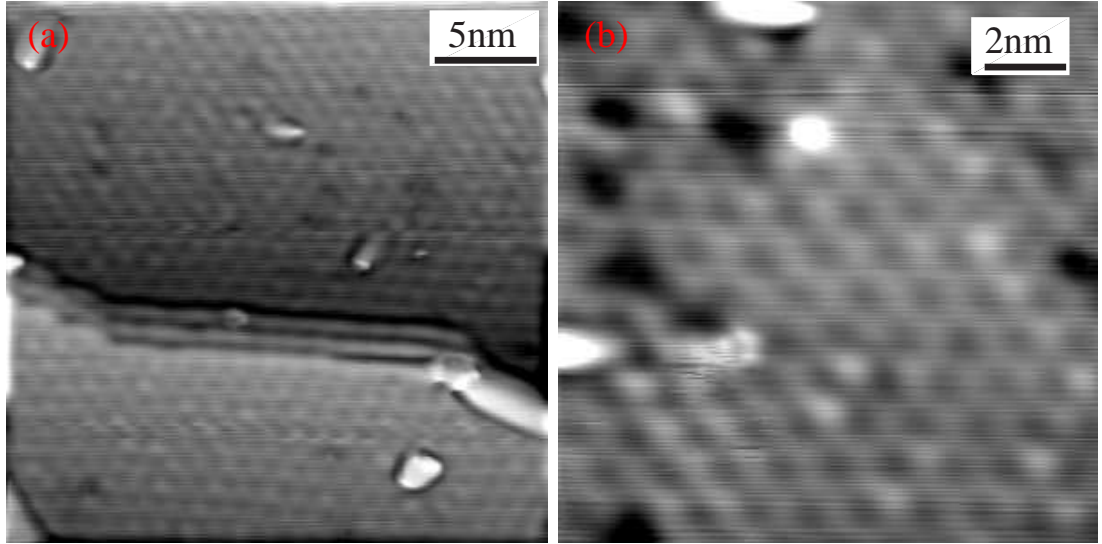


Figure 3.12: STM images of some graphitized area on the same NASA sample show vacancy defects of  $6 \times 6$  structure. It is still not clear whether graphite films on these defects are completed or not. The tip voltages of both figures were  $-2.0$  V. The constant tunneling current was  $200$  pA.

can see most of the surface is occupied by ordered SiC  $6 \times 6$  ( $18.5\text{\AA} \times 18.5\text{\AA}$ ) structure. Other disordered regions might relate to the growth of a new graphene layer or other graphene patches in the same layer (Fig. 3.13b). The atomic resolved image of Fig. 3.14a is a zoom in from the ordered  $6 \times 6$  corrugation region in Fig. 3.13b. Fourier transform analysis of this image gives evidence of the  $6\sqrt{3} \times 6\sqrt{3}$  R $30^\circ$  reconstruction and will be further discussed in Sec. 3.5.

Figure 3.15 are dual-bias images that were also taken from a region of the ordered  $6 \times 6$  region in Fig. 3.13b. The filled states and empty states are obviously different on the triangle shaped protrusion as pointed out by arrow A in Fig. 3.15, which might relate to the dangling bonds of the atoms on top. The Fourier-filtered image (Fig. 3.15c) of the negative bias scanning and its complementary Fourier-filtered image (Fig. 3.15d) reveals the origin of the features on the interfacial layer. Figure 3.15c is obtained by selecting the Fourier mask of Fig. 3.15f and displays a  $6\sqrt{3} \times 6\sqrt{3}$  R $30^\circ$  structure similar to the one in figure 3.14b. The Fourier filtered image with the anti-mask exhibits features on the surface other than  $6\sqrt{3} \times 6\sqrt{3}$  R $30^\circ$  periodicity, such as corner-hole defects as pointed by arrow B.

Figure 3.16b displays derivative tunneling spectra ( $dI/dV$  vs  $V$ ) acquired within the

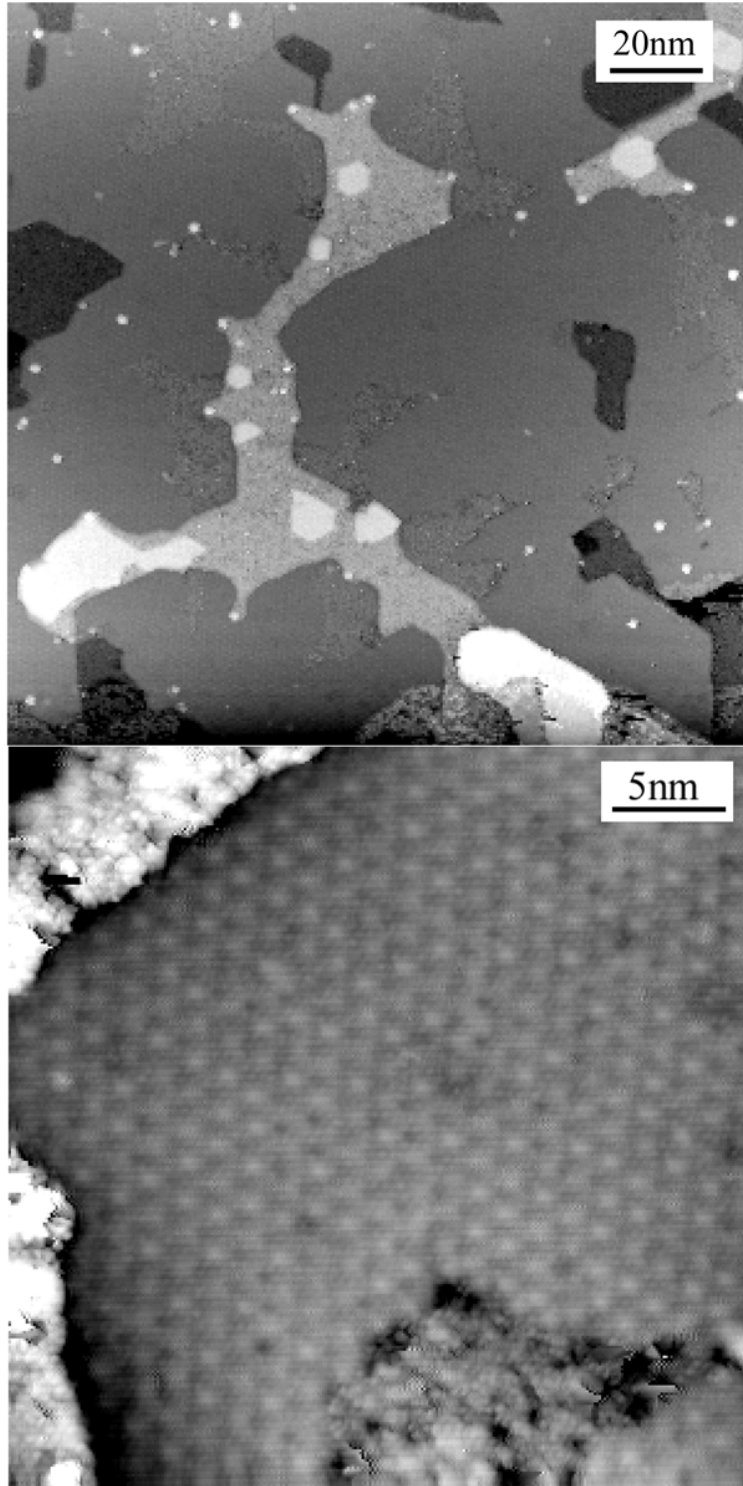


Figure 3.13: STM images of monolayer graphene on SiC(0001). The tip voltage were  $-1.0\text{ V}$  for the top image and  $-0.8\text{ V}$  for the bottom image. The constant tunneling current for both scanning was  $100\text{ pA}$ . The  $6\times 6$  corrugation is clear in the bottom figure. Disordered domains, which might be related to the growth of new graphite layer, are also visible in both figures.

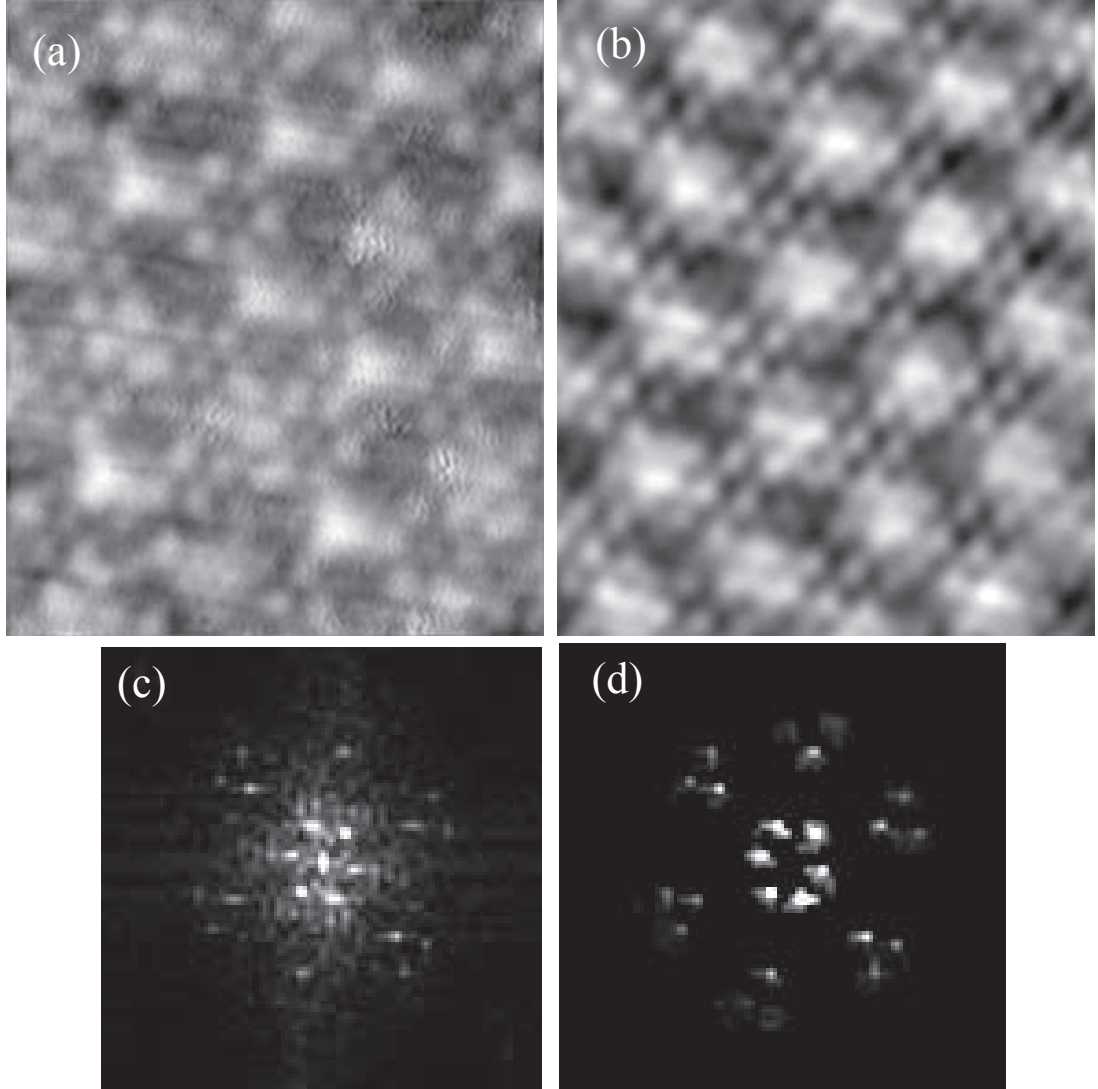


Figure 3.14: Fourier analysis on a STM image of monolayer graphene on SiC(0001) surface. The STM image and the inverse Fourier transform is on the top and the corresponding Fourier transforms on the bottom (a) The original STM image obtained from the center  $6 \times 6$  ordered region of Fig. 3.13b. The tip voltage was  $-0.8$  V and the constant tunneling current was  $100$  pA. (b) Inverse Fourier transform with selecting the region around  $\sqrt{3} \times \sqrt{3} R 30^\circ$  spots and the region around  $6 \times 6$  spots the Fourier transform spectrum of the STM image.

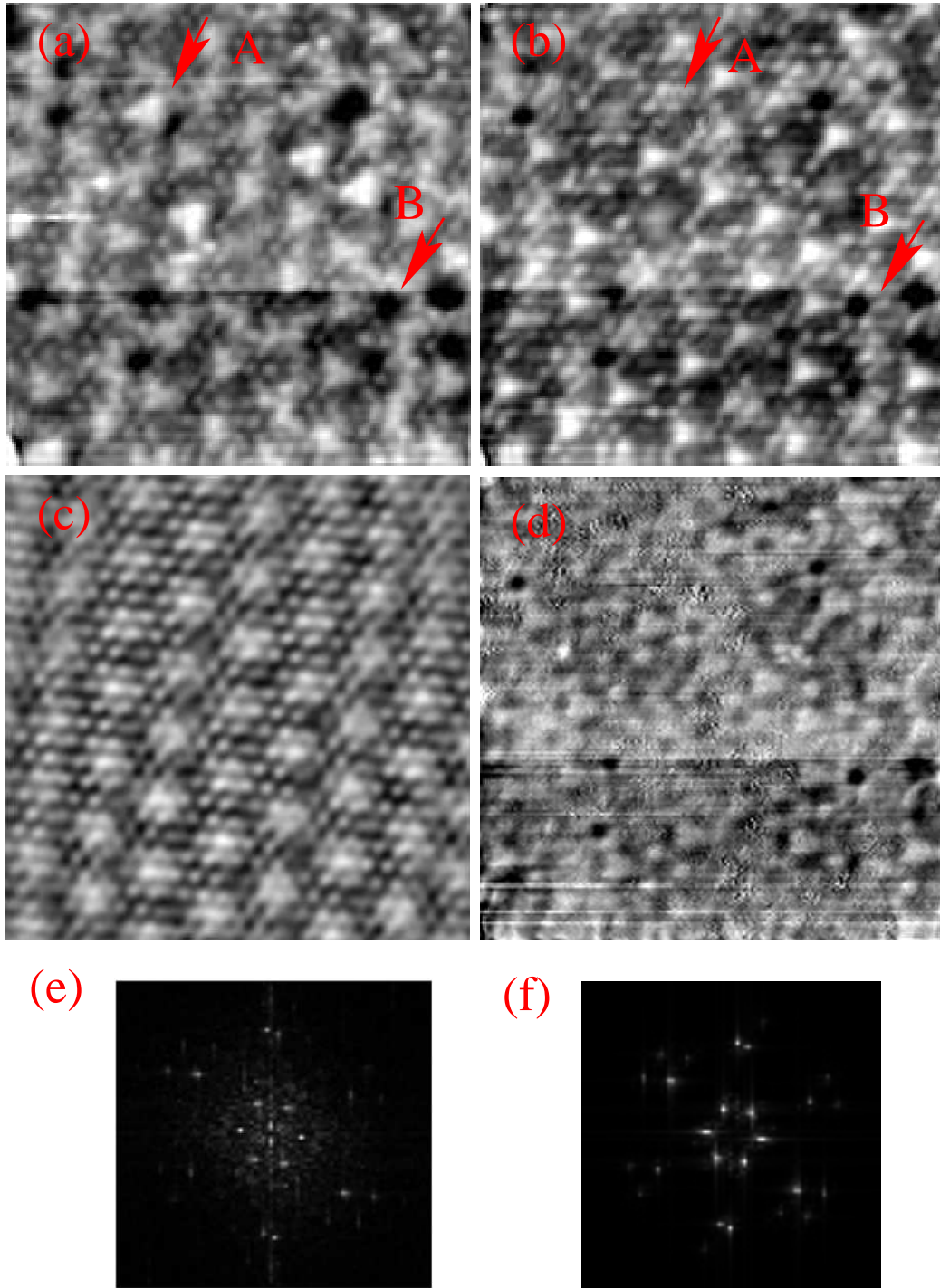


Figure 3.15: STM images of monolayer graphene film on SiC(0001) with different tip bias taken simultaneously. The sample was annealed in UHV at  $1250^{\circ}\text{C}$  for 3 mins. (a) Fill states image. The tip voltage was 0.6 V. (b) Empty state image. The tip bias is  $-0.6$  V. The constant tunneling current was both 100pA. (c) Fourier filtered image of the negative bias STM image by selecting the mask used in (f). (d) Fourier filtered image of the negative bias STM image by selecting the complementary mask of (f). (e) Fourier transform of the original STM image. (f) Fourier transform with a Fourier filter to suppress the spectrum not related to the feature LEED pattern.

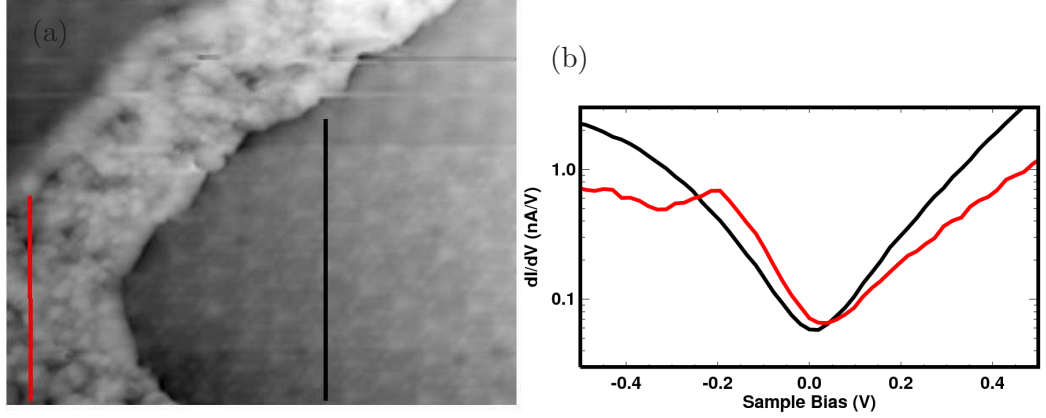


Figure 3.16: A STM image and its STS spectra of of monolayer graphene on the SiC(0001) surface. (a) STM image of a surface region of the graphitized SiC(0001) surface, which is also from the center part of Fig. 3.13b. Two major domains are clear on this image. The higher domain is a disordered region, which could be the initial growth layer of the next graphene film, since the height between the two terrace is about  $3.3\text{\AA}$ , about the distance between two adjacent graphite layers. the lower domain on the right is the ordered  $6\sqrt{3}\times 6\sqrt{3}\text{R}30^\circ$  region. (b)  $dI/dV$  spectra (log scale) acquired from disordered and ordered regions marked with corresponding color line in the image at top. Individual spectra in each region showed negligible variation from the average  $dI/dV$  shown. On the right ordered region, the  $dI/dV$  spectrum (black solid line) indicates a zero-gap semiconductor feature spectrum, which is from a graphene layer on top of the  $6\sqrt{3}\times 6\sqrt{3}\text{R}30^\circ$  interface layer. On the left disordered terrace, the  $dI/dV$  spectrum (red solid line) also displays a zero-gap semiconductor feature spectrum but with a 30 meV around shift to the filled state energies. The bump at the  $-0.2\text{ V}$  sample bias probably indicates some dangling bond states in the disordered region.



respectively-colored lines in Fig. 3.16a. The  $dI/dV$  spectrum obtained from the lower ordered  $6\sqrt{3} \times 6\sqrt{3} R30^\circ$  terrace (black solid line) is similar to that of bulk graphite with minimum at almost zero bias. On the upper terrace, the  $dI/dV$  spectrum (red solid line) of an higher disordered region also displays a zero-gap semiconductor feature spectrum but with a 30 meV around shift to the filled state energies. This disordered region could be the initial growth layer of the next graphene film, since the height between the two terrace is about  $3.3\text{\AA}$ , about the distance between two adjacent graphite layers. The bump on the negative -0.2 eV sample bias of the spectrum probably indicates some local empty states in the disordered region.

### 3.5 Interpretation of LEED Patterns and STM Images

#### 3.5.1 SiC, Graphite & Double Scattering Spots

The unit cell edge length of graphite  $a_{\text{graphite}} = 2.46\text{\AA}$  and the SiC lattice constant  $a_{\text{SiC}} = 3.08\text{\AA}$  have the relation of  $13a_{\text{graphite}} = 6\sqrt{3}a_{\text{SiC}}$ , so when the graphite basis vectors rotate  $30^\circ$  with respect to the SiC substrate basis vectors, a superlattice with a period of  $6\sqrt{3}a_{\text{SiC}}$  forms between the graphite layer and the SiC substrate (Fig. 3.10). This is the  $6\sqrt{3} \times 6\sqrt{3} R30^\circ$  reconstruction on the SiC(0001) surface [37, 81]. Accordingly, the double-scattering model became the first explanation of  $6\sqrt{3} \times 6\sqrt{3} R30^\circ$  LEED pattern [37] and was accepted widely. Following the double scattering theory [82], all the 2-D LEED double scattering spots fall on the  $6\sqrt{3} \times 6\sqrt{3} R30^\circ$  reciprocal mesh and can be expressed by the sum of SiC and graphite reciprocal primitive vectors, i.e.  $\vec{G} = k\vec{S}_1 + l\vec{S}_2 + m\vec{C}_1 + n\vec{C}_2$  ( $k, l, m, n$  all integers). The higher the index numbers are, the weaker the diffracted intensity is. However, some features of the observed  $6\sqrt{3} \times 6\sqrt{3} R30^\circ$  LEED pattern conflict with the double scattering model. Several  $6\sqrt{3} \times 6\sqrt{3} R30^\circ$  diffraction spots can be seen earlier than the graphite diffraction spots during an escalating heating process. Some high-index double-scattering spots are much brighter than should be expected. Another fact that should be noted is that no double-scattering spots are observed during the graphitization process on C-face of SiC, even for very thin graphite layer when both graphite LEED diffraction rings and SiC diffraction spots coexist.

### 3.5.2 $6\sqrt{3}\times 6\sqrt{3}$ R30° Reconstruction Layer

The major visible diffraction spots in SiC  $6\sqrt{3}\times 6\sqrt{3}$  R30° LEED pattern are all illustrated in a schematic plot (Fig. 3.17). Different sorts of diffraction spots are denoted by different symbols (Fig. 3.17). Symbol sizes roughly illustrate relative intensities. The LEED patterns of all these spots are clearly observed in the mono-graphene phase (Fig. 3.7 b & c and Fig. 3.9). For our LEED system, the zero order diffraction pattern (00) can be observed by tilting the sample at more than 10° (Fig. 3.9d).

In our LEED experiments,  $\sqrt{3}\times\sqrt{3}$  R30° spots are observed when the SiC samples were heated up to 1100° C (Fig. 3.7b) and disappeared after annealing over 1250° C (Fig. 3.9). The  $\sqrt{3}\times\sqrt{3}$  R30° and  $6\sqrt{3}\times 6\sqrt{3}$  R30° coexist at the early formation of  $6\sqrt{3}\times 6\sqrt{3}$  R30° (Fig. 3.7 b & c). The LEED pattern around first-order  $\sqrt{3}\times\sqrt{3}$  R30° diffraction spots at this phase is a key to understanding the LEED pattern. The traditional double scattering model [37] and the mixed reconstruction model [61] give different explanations for these spots. For the double scattering model, one set of three spots closest to the first order  $\sqrt{3}\times\sqrt{3}$  R30° are regarded as double scattering spots with low index values. These spots are labeled as “A3” spots in Fig. 3.17. Owman et al. attributed the source of the A3 LEED spots to a mixture of  $6.2\times 6.2$  and  $2.1\times 2.1$  R30° reconstructions. In our escalating temperature annealing experiments, we found that the A3 spots appear before the formation of any graphite diffraction spots, therefore they are not from double scattering initially. We did not see  $6.2\times 6.2$  and  $2.1\times 2.1$  R30° reconstructions from our STM images. We did not see any other LEED spots than A3 following these two reconstructions proposed by Owman et al. either. Therefore we think these reconstructions are not dominant features of the surface and are not the origin of the “A3” diffraction spots. In our LEED pattern, A3 spots are usually brightest among other  $6\sqrt{3}\times 6\sqrt{3}$  R30° spots for most E-beam energies (Fig. 3.9) and even visible when graphite films are thick (Fig. 3.7d), which means that the A3 spots are very likely from a persistent reconstruction layer. The corresponding STM images provide strong support to this conclusion, and indicate that the reconstructed layer exist at the interface between SiC and graphite.

Annealing the sample in UHV at 1250° C for 3 min. produces monolayer graphite on



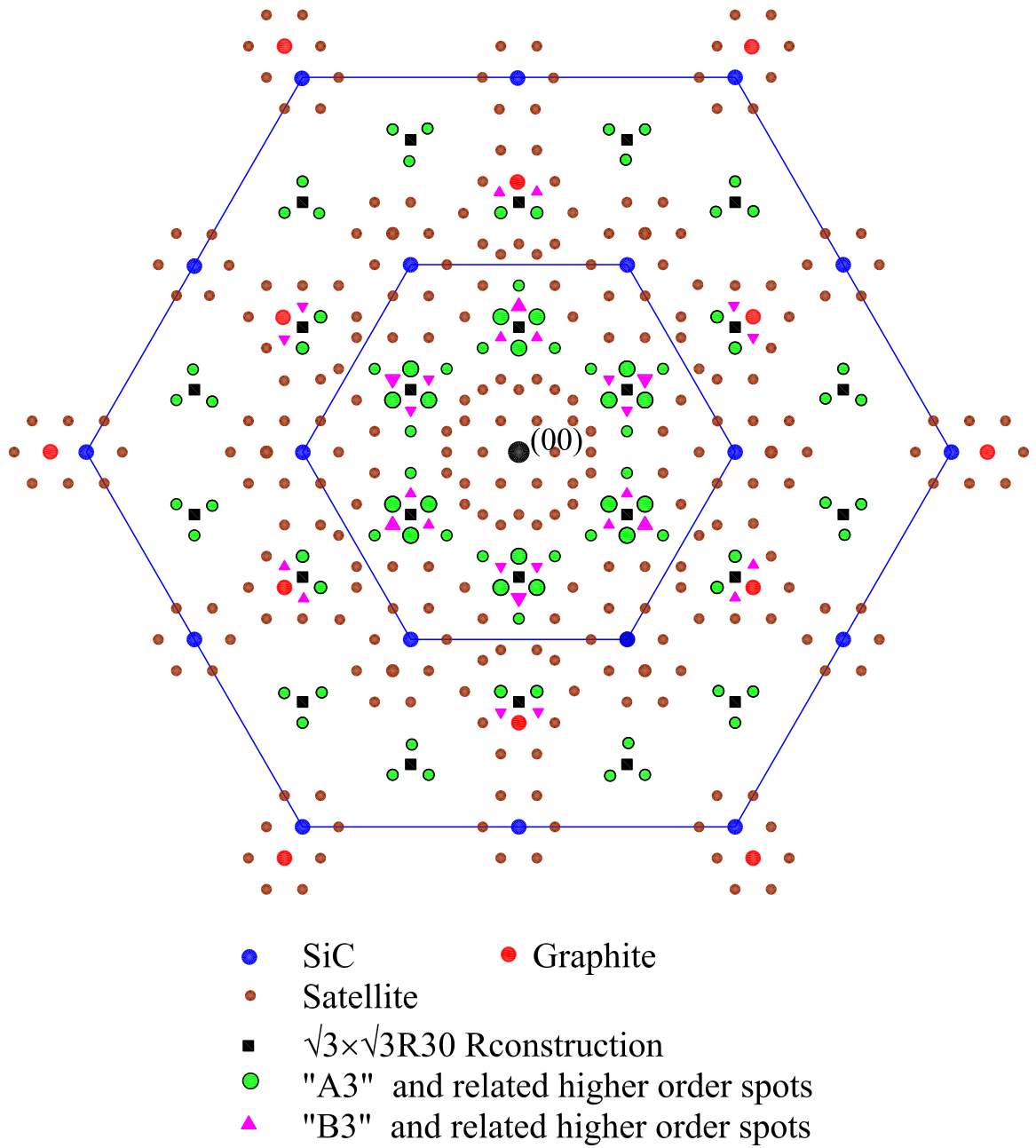


Figure 3.17: Schematic plot of the LEED pattern that thin graphite growth on the SiC(0001) surface. Diffraction spots are categorized according to their sources. The sizes of the spots are drawn according to their LEED intensities.

SiC substrate as estimated via Auger intensities. Although the large scans (Fig. 3.13b) show the ordered surface corrugation following SiC  $6\times 6$  geometry, the real reconstruction should still be defined as  $6\sqrt{3}\times 6\sqrt{3}$  R30° reconstruction (Fig. 3.18b) according to the atomic resolution STM image (Fig. 3.14a) obtained on the center ordered region of (Fig. 3.13b). The distinct graphite LEED diffraction spots also support the existence of a graphite film. Recent low temperature STM results from NIST on the sample that was prepared in our UHV chamber under the same condition resolved both interfacial layer and the graphene layer on top [56]. We believe that instead of resolving the top graphene layer, at the bias voltages typically chosen, the STM images features due to atoms at the interface between the first graphene layer and the SiC substrate. The situation that STM current tunneling through one graphene layer and resolving the interface was also found by Charrier et al. [71]. STM images with atomic resolution of graphite atoms over SiC  $6\times 6$  corrugation were obtained by other STM experiments [11, 38, 83].

Since all the LEED diffraction spots follow SiC  $6\sqrt{3}\times 6\sqrt{3}$  R30° reciprocal mesh, according to the kinematic scattering model, the interfacial layer should have a SiC  $6\sqrt{3}\times 6\sqrt{3}$  R30° unit cell. However, it is extremely difficult to determine the exact unit cell of such a large reconstruction. Using Fourier transform on LEED patterns to reproduce the atom reconstructions leads to “phase” problem, since no phase information is recorded by LEED patterns and they only reflect the integral results of all the diffractions. Thus, we applied Fourier transform on the atom-resolved STM image of the interfacial layer (Fig. 3.14a). Comparing the Fourier transform image with LEED patterns, we find the distinct spots in the Fourier transform image (Fig. 3.14c) coincides with the A3 diffraction spots position in LEED pattern (Fig. 3.9a). Therefore we applied a Fourier filter on the Fourier transform image and obtained a filtered Fourier transform image related to the A3 LEED spots and  $6\times 6$  surface corrugation (Fig. 3.9d). Since this filtered Fourier transform image includes the phase information, we can make inverse Fourier transform and obtain a filtered STM image in real space (Fig. 3.14b).

In order to further identify the SiC  $6\sqrt{3}\times 6\sqrt{3}$  R30° interfacial layer structure, we developed a Matlab program to calculate the intensities of kinematic scattering with different

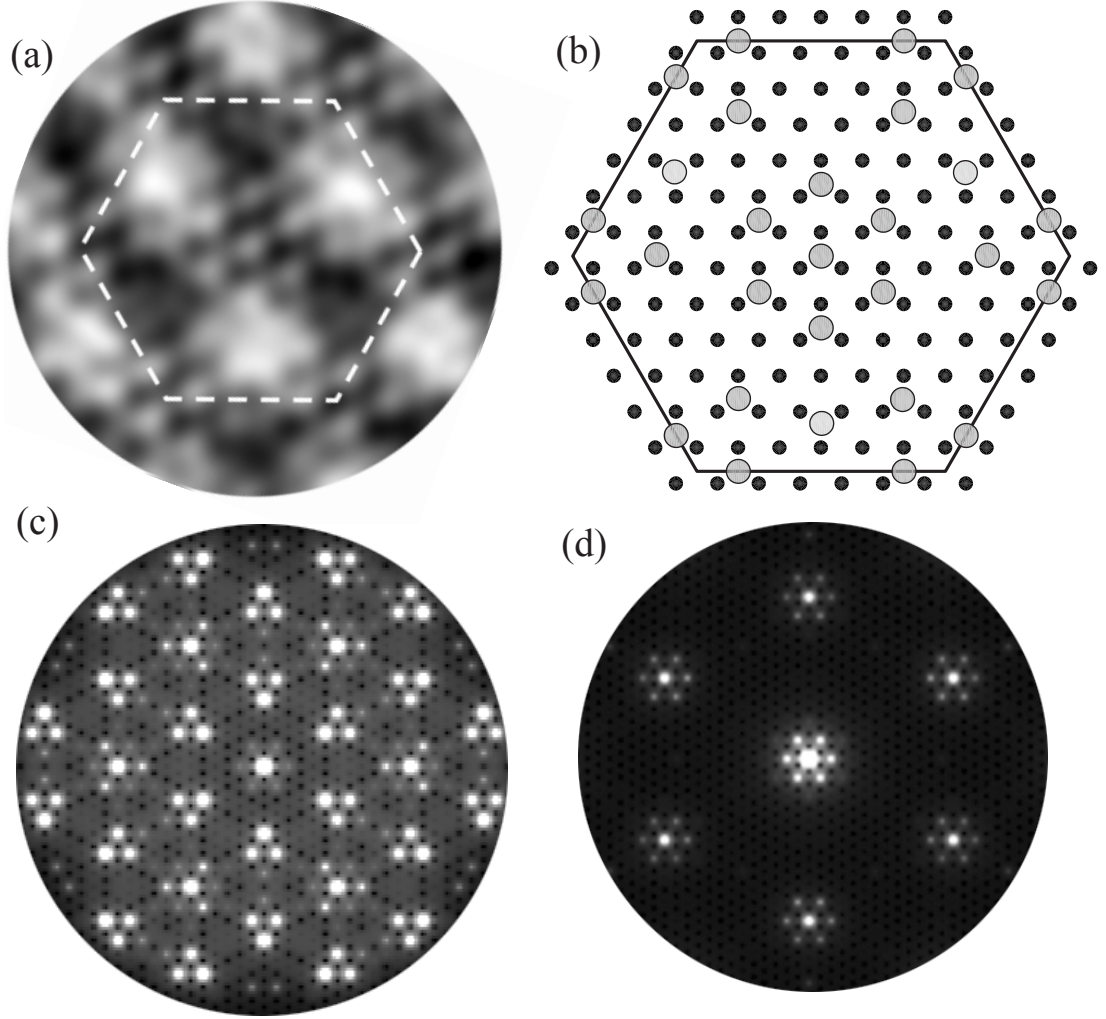


Figure 3.18: Simulation with kinematical scattering LEED pattern of SiC(0001) surface on a plane grid. The incident electron beam energy is set to be 60 eV. (a) one  $6\sqrt{3} \times 6\sqrt{3}$  R30° unit cell cut from the Fourier-filtered STM image of Fig. 3.14b (white dashed line). (b) Schematic drawing of one unit cell of the  $6\sqrt{3} \times 6\sqrt{3}$  R30° layer (grey shaded circles) sitting on SiC  $1 \times 1$  substrate (filled black circle) used in the simulation. (c) Simulated LEED pattern from the  $6\sqrt{3} \times 6\sqrt{3}$  R30° reconstruction. (d) Simulated LEED pattern of four layers of graphene with 0.08 Å surface corrugation.

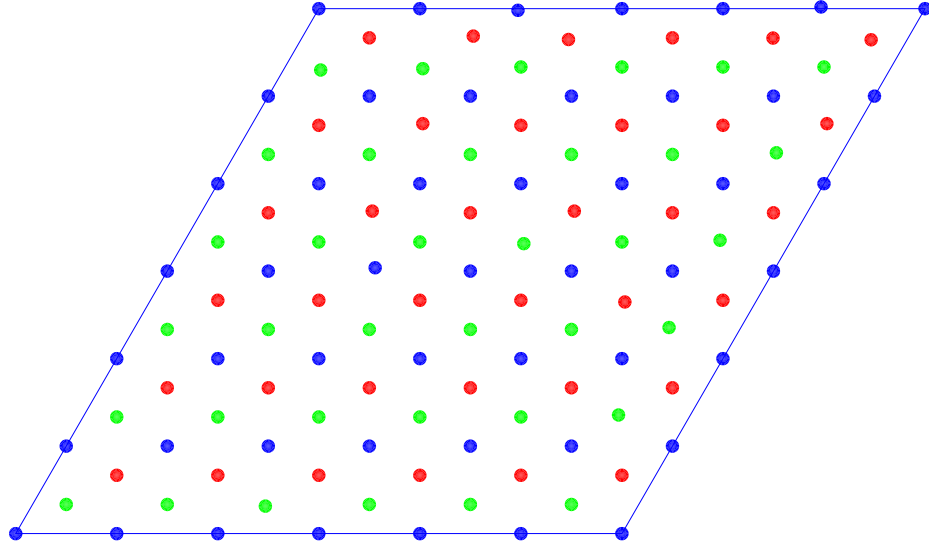


Figure 3.19: Schematic plot of the three SiC  $\sqrt{3}\times\sqrt{3}$  R30° reconstruction sublattices in one SiC  $6\sqrt{3}\times 6\sqrt{3}$  R30° unit cell. The three sublattices are plotted with three different colors: blue, red and green. Superposing these 3 sublattices yields a SiC  $1\times 1$  lattice.

SiC  $6\sqrt{3}\times 6\sqrt{3}$  R30° unit cells. We used the 2-D grating function in IDL software to plot the simulated diffraction pattern through importing the Matlab output data of the LEED intensity on each diffraction spot (Fig. 3.18c & d).

On each atom layer, a SiC  $6\sqrt{3}\times 6\sqrt{3}$  R30° unit cell involves in 108 Si or C atoms of SiC, or  $169\times 2$  graphite carbon atoms (Fig. 3.10), or 36 SiC  $\sqrt{3}\times\sqrt{3}$  R30° adatoms. The schematic drawing of the cross section of top five stacking layers on a graphitized SiC(0001) surface is plotted in Fig. 3.5. Simulations with single-layer atoms and multi-layer atoms were all conducted. The SiC  $6\sqrt{3}\times 6\sqrt{3}$  R30° unit cell construction is proposed in Fig. 3.18b. The construction of the SiC  $6\sqrt{3}\times 6\sqrt{3}$  R30° unit cell must be compatible with an important fact that the extinction of the SiC  $\sqrt{3}\times\sqrt{3}$  R30° spots in corresponding LEED patterns (Fig. 3.9). A SiC  $1\times 1$  lattices can be regarded as the superposing of 3 sets of  $\sqrt{3}\times\sqrt{3}$  R30° sublattices (Fig. 3.19). The  $\sqrt{3}\times\sqrt{3}$  R30° LEED spots extinction can be achieved by the equal or almost equal occupation of the three  $\sqrt{3}\times\sqrt{3}$  R30° sublattices in the SiC  $6\sqrt{3}\times 6\sqrt{3}$  R30° unit cell (Fig. 3.18b). Changing the atom arrange within the  $6\sqrt{3}\times 6\sqrt{3}$  R30° unit cell, we can demonstrate all sorts of diffraction patterns. Our proposed  $6\sqrt{3}\times 6\sqrt{3}$  R30° unit cell is based on the  $\sqrt{3}\times\sqrt{3}$  R30° extinction consideration and the actual atom locations in the

Fourier filtered STM image (Fig. 3.18a).

A single layer simulation according to the proposed SiC  $6\sqrt{3} \times 6\sqrt{3} R30^\circ$  unit cell is plotted in Fig. 3.18c. The simulation reproduces the A3 diffraction spots very well. It also generates the 3-fold symmetry satellites around SiC first-order diffraction spots. Although these satellites in most LEED patterns show 6-fold symmetry, 3-fold symmetry is also observed on some LEED patterns (Fig. 3.9c).

The other set of three spots closest to the first order  $\sqrt{3} \times \sqrt{3} R30^\circ$  are also visible (Fig. 3.9), which are represented as “B3” in Fig. 3.17. Owman. et al. attributed B3 spots to a  $5.3 \times 5.3$  reconstruction. In our LEED pattern, we did not see any other diffraction spots from this proposed  $5.3 \times 5.3$  reconstruction. Our STM results do not show any  $5.3 \times 5.3$  structure either. Actually, B3 spots can also be reproduced with kinematic scattering method by placing the atoms at the different positions of the defined  $6\sqrt{3} \times 6\sqrt{3} R30^\circ$  unit cell hexagon (Fig. 3.18b). However we have not found a unit cell that yields B3 spots and satisfies other LEED features at the same time. One spot of B3 spots is obviously much more stronger than the other two in all the LEED patterns (Fig. 3.9). The structure factor related to B3 spots needs to be further identified. A3 spots are generally much stronger than B3 spots, therefore the  $6\sqrt{3} \times 6\sqrt{3} R30^\circ$  layer related to A3 spots should be the dominant feature of ordered interfacial layer.

In the kinematic scattering simulation, we supposed the atoms forming the reconstruction layer are uniform, i.e. either all Si atoms or all C atoms. The real reconstruction layer might have mixed character, which could change the diffraction significantly. Since the real LEED patterns are very reproducible, we can conclude that the composition of the reconstruction should be fixed. The reconstruction layer between graphite and SiC could be more than one layer and very complicated. This needs to be further investigated in order to give a complete explanation of the  $6\sqrt{3} \times 6\sqrt{3} R30^\circ$  LEED pattern with only kinematic scattering.

### 3.5.3 Satellite Spots

Another salient feature of the  $6\sqrt{3}\times 6\sqrt{3}$  R30° LEED pattern is that a hexagon of satellites corresponding to a SiC  $6\times 6$  always appears around the primary diffraction spots of SiC and graphite, as well as the most intense  $6\sqrt{3}\times 6\sqrt{3}$  R30° spots, such as A3 group (Fig. 3.7 and Fig. 3.9). All the satellite hexagons have the same size and the orientation as the  $6\times 6$  reconstruction hexagon around (00) spot (Fig. 3.9d). We can not develop all the satellite hexagons with a SiC  $6\times 6$  reconstruction starting from origin spot (00), such as satellites around graphite spots (Fig. 3.17), therefore these satellites can not be attributed to  $6\times 6$  reconstruction, although they must reflect some six-fold symmetry on the surface. The simulation of  $6\sqrt{3}\times 6\sqrt{3}$  R30° layer reproduces some satellites (Fig. 3.18c), therefore we tend to think the origin of the satellites could also be explained from the kinematic scattering of the  $6\sqrt{3}\times 6\sqrt{3}$  R30° layers. The reconstruction between graphite and SiC is probably more than one layer, so the construction of this interfacial layer and the corresponding simulation need to be further investigated.

The origin of satellites around SiC and major  $6\sqrt{3}\times 6\sqrt{3}$  R30° spots could be attributed to a more complicated  $6\sqrt{3}\times 6\sqrt{3}$  R30° interface reconstruction or to higher-order double scattering as proposed by other groups [37, 39]. However, when graphite films are thick, the origin of satellites around graphite integral-order spots (Fig. 3.7d) can't be explained by either way above. The SiC and reconstruction LEED spots are almost invisible at this time, therefore these satellite spots are unlikely to be due to double scattering or the interface reconstruction.

Our STM experiments show that the graphitized surface have less than 0.5 Å vertical corrugation with a  $6a_{SiC} \times 6a_{SiC}$  period. The true corrugation amplitude is difficult to determine due to the unknown distribution of electron density and the finite distance from the tip to the surface. Recent low-temperature STM results suggest that the corrugation could be as large as 1 Å [56]. This surface corrugation appears to be the origin of the  $6\times 6$  satellites. The nonplanar graphite layers with a  $6\times 6$  vertical corrugation plays the role of a two-dimensional phase grating [82, 84] that generates satellite spots around graphite spots.

We simulated the LEED pattern with kinematic scattering theory by adding SiC  $6 \times 6$  corrugation on 4 layers of graphene atoms with vertical amplitude of  $0.08 \text{ \AA}$ . The simulation results (Fig. 3.18d) show that the satellites around graphite LEED spots can be generated from this graphite corrugation. The  $6 \times 6$  corrugation of graphite films could be due to the perturbation of the  $6\sqrt{3} \times 6\sqrt{3} \text{ R}30^\circ$  interface layer underneath the lowest graphite layer.

We believe our  $6\sqrt{3} \times 6\sqrt{3} \text{ R}30^\circ$  unit cell interpretation of the LEED pattern is approaching the real situation on graphitized SiC(0001) surface, although it seems still a long run to reproduce the complete LEED patterns in Fig. 3.9 with the kinematic scattering simulation. Perhaps, double scattering should not be ignored completely.

Further considerations could be added into the current Matlab code includes,

- 1) Construct more than one interfacial layers between graphite and SiC, which is probably the real situation.
- 2) Consider more vertical atom displacements for the interfacial layer rather than a totally flat atoms sheet as current calculation. We have successfully developed the SiC  $6 \times 6$  corrugation for graphite films. However, further adjustment of the vertical displacement of each atom on the interfacial layer is a time consuming task for the current Matlab code.
- 3) Put mixed Si and C atoms into each interfacial layer rather than using mono-type atoms for each layer.
- 4) Develop calculation methods to optimize the atom arrangement on surface automatically.

## CHAPTER IV

# CHARACTERISTICS OF GRAPHITE RIBBONS ON SiC (0001) SURFACE

### 4.1 Vicinal Cut SiC Samples

The vicinal samples have much narrower terraces than on-axis samples after  $H_2$  etching, since the formation of the terrace is due to the vicinal angle of  $3.5^\circ$  between the basal plane and the SiC(0001) plane [75]. Supposing the height between adjacent terraces is half a unit cell height of 6H-SiC, i.e.  $7.5 \text{ \AA}$ , then the terrace width should be  $0.75 \text{ nm} / \tan(3.5^\circ) = 12.2 \text{ nm}$ , which is close to what we measure in Fig. 4.1. It appears possible that ribbons of controlled width and crystallographic orientation can be growth on these narrow SiC terraces, as shown schematically in Fig. 4.1c. Should this prove to be possible, it would be a tremendous advance in graphite nano-ribbon synthesis, since the electronic properties of a graphene ribbon are determined entirely by its width and edge topology [16, 17, 85]. Ideally the graphite on such narrow terraces forms ribbons with an edge confinement, which can be determined from the orientation of SiC substrate and the relative  $30^\circ$  rotation of epitaxial graphite. For the SiC samples studied, the miscut was  $3.5^\circ$  toward the  $[10\bar{1}0]$  direction, which should result in step edges that run along the the edges  $[11\bar{2}0]$  direction. This would result in “zig-zag” edges on the epitaxial graphite ribbons. However, current preparation procedure still can’t make such ordered ribbons. The real terrace edges are not exactly parallel, and often have triangle shapes (Fig. 4.1a), therefore the edge states are still uncontrolled. Clear  $6 \times 6$  related corrugation can been seen on all the terraces. Graphite films appear to be continuous over the terrace edges (Fig. 4.1b), as proposed by Seyller et al. [86]. Since isolated the ribbons are preferable, further preparing techniques should be developed to break the graphite over terraces.



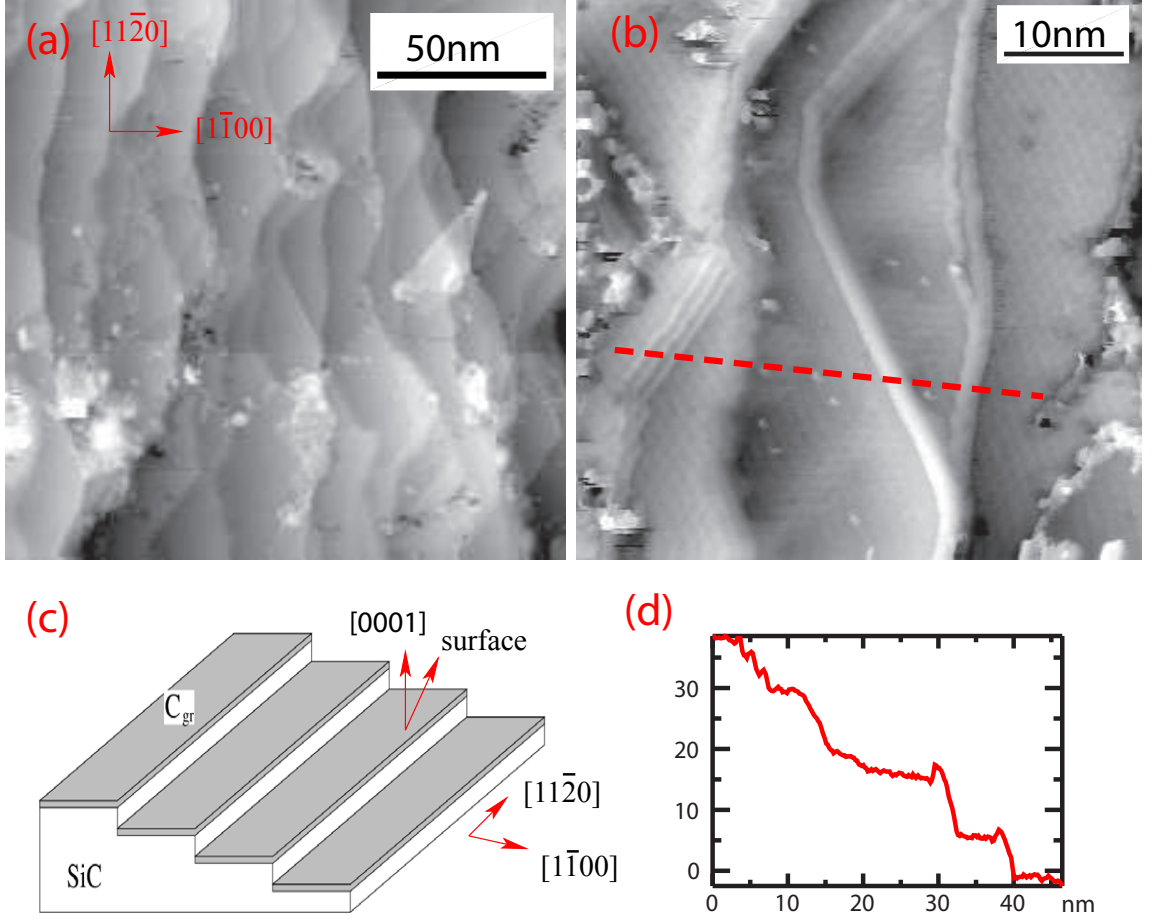


Figure 4.1: STM images on graphitized  $3.5^\circ$  vicinal SiC(0001) surface. (a) The large scale STM image shows the terraces on graphitized surface. Step edges run along  $[11\bar{2}0]$  on average. Two pieces of peeled off graphite flakes are visible on the surface. The tip voltage was  $-1.0$  V and the constant tunneling current was 100 pA. (b) Typical graphitized surface with  $6\times 6$  corrugation are visible on each terrace. A three bilayer step is also resolved. The tip voltage was  $-1.0$  V and the constant tunneling current was 100 pA. (c). A schematic drawing of the ideal graphite ribbons growth on each terraces with parallel ribbon edge running along  $[11\bar{2}0]$  direction. (d) The profile of terraces shows the the step height between two adjacent major terraces is 0.75 nm, which is the height of three Si-C bilayer.

## 4.2 *Patterned Samples & Graphite Ribbons*

In order to investigate graphene/graphene 1D interfaces, it will be necessary to perform STM/STS studies of nanopatterned samples. We applied a typical E-beam lithography process to pattern the graphitized SiC sample with the facilities at Georgia Tech. The thorough description of E-beam lithography work can be found in our collaborator Zhimin Song's thesis [87].

### 4.2.1 E-beam Lithography Process for Graphite/SiC(0001)

I just give a outline of the whole lithography process (Fig. 4.2), since my work does not emphasize on this part.

1. Deposit metal pads. The metal is gold and palladium alloy and the equipment used is E-beam metal evaporator. Since metal has very high contrast to the graphitized surface in a SEM view, those metal pads are used for locating the pattern in the following lithography process.
2. Spin coating. The whole surface was rather uniformly covered by Hydrogen silsesquioxane (HSQ) E-beam resist [88, 89] through standard spin coating method.
3. E-beam lithography. The lithography was done in MiRC of Georgia Tech with JOEL JBX 9300, which has a resolution as high as 20nm. The dose of the E-beam was very carefully calibrated by the several experiments on dummy samples.
4. Development. This step includes baking the sample to 250° C for 2 mins and developing in solvent TMAH and rinsing in DI water to remove the HSQ exposed to the E-beam.
5. Plasma etching. Standard  $O_2$  plasma RIE process. Oxygen will remove graphite films without HSQ protection and then oxidize the SiC substrate.
6. HSQ removal. The HSQ resist over pattern graphite part is removed by HF solvent, which also gets rid of oxidized SiC surface due to the  $O_2$  RIE process. The SiC surface is passivated by hydrogen after the HF rinse and the graphite surface should be exposed to air.

Because locating such small structures within the few-micron scan range of a UHV STM

## Flow of Graphene Ribbon Prepare Procedure

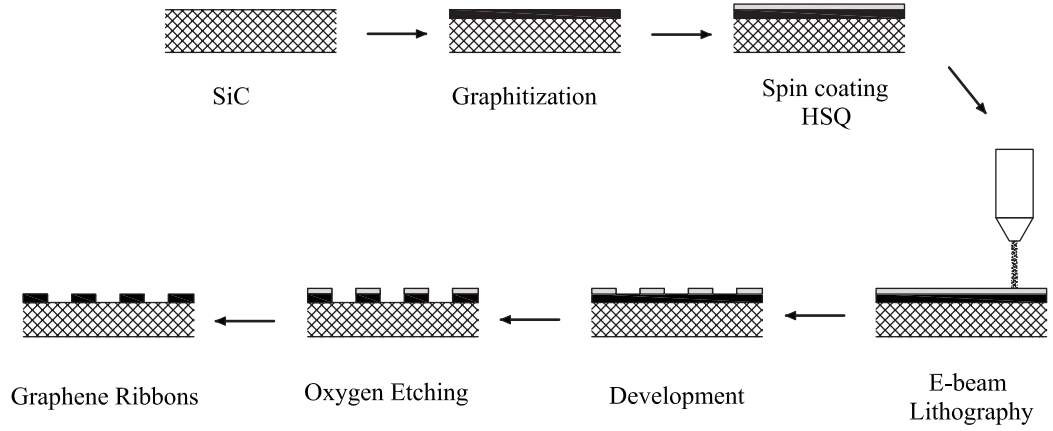


Figure 4.2: Schematic flow of the E-beam lithography process for fabricating graphene ribbons.

is not easy, we opted to fabricate samples with a repetitive pattern across a 1 mm area. The repetitive patterns are  $4 \times 4 \mu\text{m}$  size, consisting of several ribbons with 80nm to 400nm width.

### 4.2.2 STM on the Patterned Sample

A 6H-SiC sample was  $H_2$ -etched in the RF furnace and graphitized in our UHV chamber at  $1395^\circ\text{C}$  for 8 min. (note that the 6H-SiC sample is conductive). The Auger peaks intensity show the thickness of graphite film is about 3 layers. The sample was subjected to the patterning process described above. After removing the HSQ on graphite and mounting the sample into the UHV chamber, we observed a LEED pattern with both graphite and SiC diffraction spots on the center of the sample and only SiC diffraction spots out of center, which is a proof of successful graphite removal outside the patterned region. Figure 4.3d shows a  $6 \mu\text{m}$  STM image taken after removing HSQ resist. The pattern observed is similar to those founded by optical microscopy, SEM, and AFM images before HSQ removal, except for some glitches due to the interaction between the tip and the HSQ residue. The STM profile on the surface show that the height between graphite (higher region) and SiC (lower region) is around 20 nm. This is obviously against the results from AFM measurement

when HSQ exist, which show only 10 nm around height difference between the SiC surface and the HSQ surface. This abnormal STM height is very likely due to the HSQ residue on graphene ribbon region. The non-conductive HSQ led to a large tip vertical adjustment by the STM servo.

When the sample was heated to successively 500° C, much better STM tunneling current was obtained and higher resolution STM images were acquired (Fig. 4.4). In this proof-of-principal attempt, residual contamination from the e-beam resist(HSQ) was detected, but the graphite was intact beneath the contamination layer, as shown in Fig. 4.4. The 1  $\mu$ m STM image (Fig. 4.4a) indicate that only several angstrom height between the graphene ribbon region and SiC region. However the “nanocaps” from HSQ spread all over the surface during heating, so we cannot know original height between graphene ribbons and adjacent SiC region. The boundary between graphite and SiC is not obscure due to the nanocaps. The HSQ nanocap particles appearing on surface are around 2 nm size. The STM image on the flat graphite beneath the nanocaps show SiC  $6\sqrt{3} \times 6\sqrt{3}$  R30° interfacial structures (Fig. 4.4b & c). On another flat graphene ribbon region (Fig. 4.4d), STM resolved the typical  $6 \times 6$  corrugation surface. The profile indicates that the height between domains on the surface beneath nanocaps still maintain one SiC bilayer height or 1/2 SiC unit cell height, similar to the surface before the lithography process.

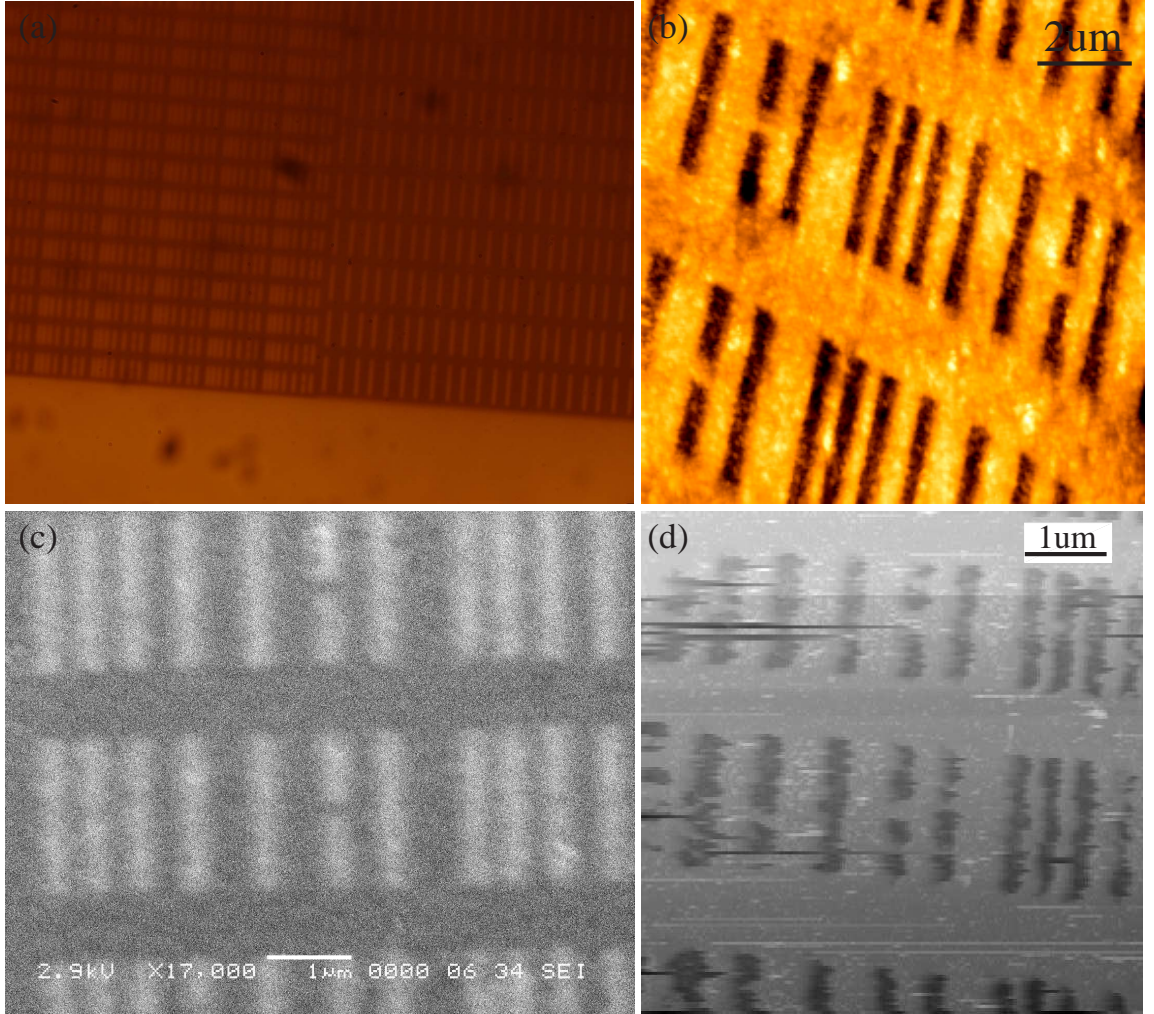


Figure 4.3: Patterned graphite ribbons after E-beam lithography process. (a) Optical microscopy image. The photo was taken under 150 times amplification mode. (b) AFM image before removing HSQ resist. (c) SEM image before removing HSQ resist. The AFM result indicate that the height between the HSQ surface (high region) and SiC surface (low region) is around 10 nm. (d) STM image after removing HSQ resist with HF solvent. The tip voltage was  $-4.0$  V and the constant tunneling current was 100 pA. The image was taken under big scan mode. The profile on the surface show that the height between graphite (higher region) and SiC (lower region) is around 20 nm. This is obviously against the result from AFM measurement when HSQ exist. This abnormal STM height different is due to the HSQ residue on graphene ribbon region.



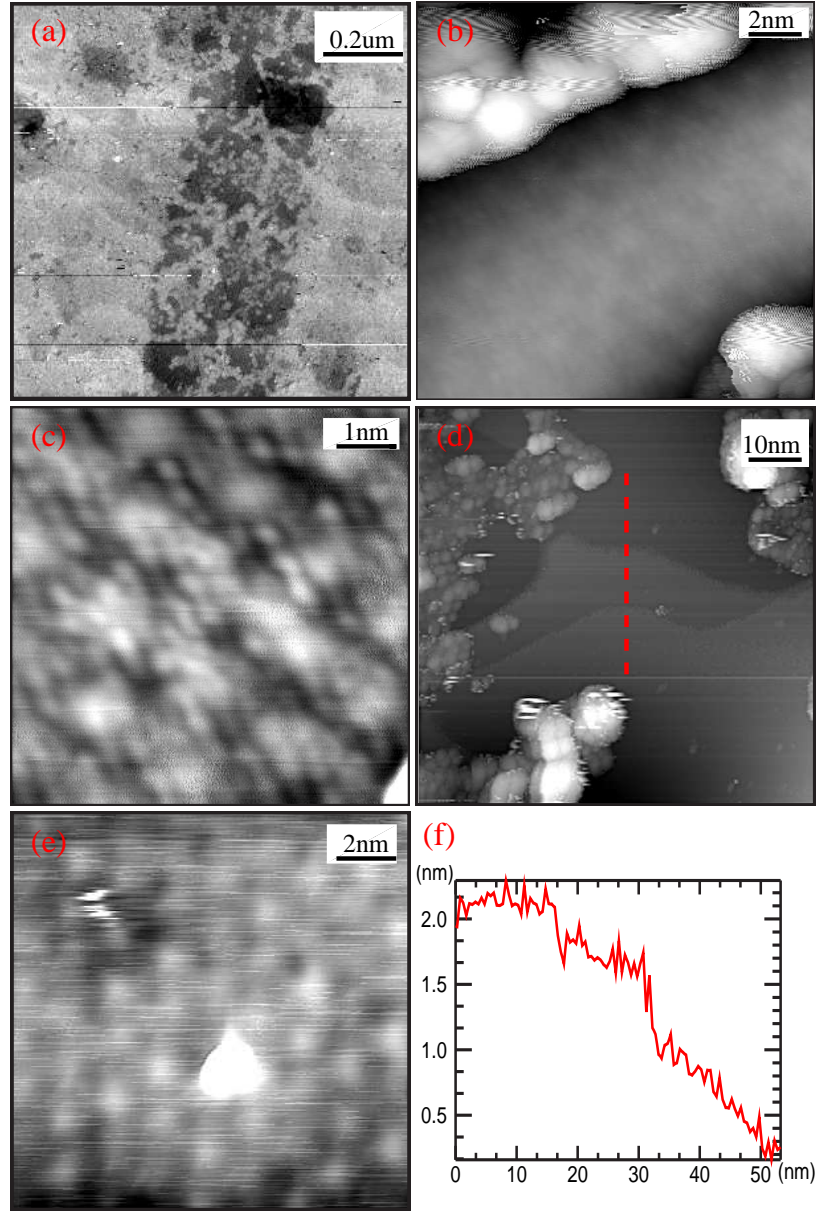


Figure 4.4: STM images over patterned graphite ribbons after E-beam lithography process. The surface was subsequently heated to 500° C in the UHV chamber. (a) STM over both graphite and SiC regions. The higher region is graphite ribbon region and the lower region is the SiC region with graphite removal in the lithography process. “Nanocaps” from HSQ resist cover much of the surface. The tip voltage was  $-4.0$  V and the constant tunneling current was 100 pA. (b) A flat region not covered by HSQ shows SiC  $6\times 6$  corrugation. The tip voltage was  $-0.9$  V and the constant tunneling current was 1 nA. (c) Atomic resolution STM image on the center flat region of (b). SiC  $6\sqrt{3}\times 6\sqrt{3}$  R30° interfacial layer is resolved. The tip voltage was  $-0.5$  V and the constant tunneling current was 1 nA. (d) Another flat region show terraces remaining  $H_2$  etching features. The height between adjacent terraces are the SiC bilayer height or 6H-SiC half unit cell height. The tip voltage was  $-2.5$  V and the constant tunneling current was 100 pA. (e) SiC  $6\times 6$  corrugation obtained on the flat region in (d). The tip voltage was  $-0.4$  V and the constant tunneling current was 100 pA. (f) The profile along the red line in (d).

## CHAPTER V

### CHARACTERISTICS OF GRAPHENE FILMS ON SiC C-FACE

The Si-face and C-face of SiC have significantly different chemical and physical properties. The C-face of SiC is more active for oxidation, 10 times the rate of Si-face [90], and graphitization. SiC oxidation process is critical for fabricating high power MOSFETs and has been studied many years, however the poor quality of the interface between SiC bulk and the oxide dielectrics film is still the barrier for the development of SiC high power devices [20].

The topologies on graphitized C-face of SiC are significantly different from those on Si-face [40, 41]. Graphitized C-face surface generally has larger size domains and terraces than Si-face according to AFM and X-ray experiments [91]. STM images on C-face samples graphitized around 1400° C often show nanocaps [43] and nanotubes [42] on surface. Further annealing to higher temperature can yield different products. Kusunoki et al. got carbon nanotube growth perpendicular to the SiC(000 $\bar{1}$ ) face at 1700° C [41], however An et al. obtained a flat surface covered by graphite films on the same surface [40]. An et al. observed that the nanocaps disappear when the sample is heated over 1450° C [40]. However, we did not see the disappearance of carbon nanocaps in our graphitization experiments. According to the KRIPES spectra, Forbeaux et al. concluded that the graphitization on the C-face of SiC results in a hybridization between the anti-bonding  $\pi^*$  states and the occupied states of the SiC bulk or a 2 $\times$ 2 reconstruction layer. The hybridization leads to a strong interaction between the first graphite layer and the layer underneath. This strong bounding limits the free motion of small graphite patches and is thought to lead to azimuthally disordered patches on the surface [92].

## 5.1 *Sample Preparation*

The preparation of C-face samples is similar to that of Si-face samples described in Chap. 3. The first process is still  $H_2$  etching. The etched SiC(000 $\bar{1}$ ) surfaces also have the ordered terraces with one or 1/2 of unit cell height steps between. The C-face graphite films were graphitized either in the UHV chamber or in the home-built high vacuum RF furnace. Graphitization in the furnace yields higher quality graphite films with flatter surfaces and larger terraces, thus the surface analysis results presented in this chapter are all on the furnace graphitized samples. In the RF furnace, samples were graphitized from 1300° C to 1500° C around 10 to 20 min. for different thicknesses. Graphitized surfaces are often checked by ambient AFM first and then the sample is mounted into the UHV chamber for LEED, AES and STM experiments. The samples are not ultrasonically cleaned steps before mounting in the chamber, since the graphite films could be degraded by the cleaning process.

In our UHV chamber, the C-face graphitization starts at 1200° C and the graphite film has faster growth rate than on the Si-face. When annealing temperature is over 1350° C in UHV, there is no SiC LEED pattern and no Si peak in AES. The LEED pattern evolution on the C-face is also totally different from that on the Si-face (Fig. 5.1 & Fig. 3.7). Without a Si evaporator source, the 3×3 reconstruction LEED pattern can be seen at a temperature of 1100° C. The biggest difference on the two faces is that the C-face shows graphite diffraction rings or arcs, while diffraction spots are observed on Si-face. Graphite rings begin to develop when the annealing temperature is above 1200° C.

## 5.2 *LEED Results*

In order to have minimal influence from the doping of the SiC substrate, the magnetoresistance and other transport measurements were all conducted on undoped 4H-SiC samples. My graphitization study on C-face of SiC was also on these nonconductive 4H-SiC samples. Another reason for selecting 4H-SiC is that 4H-SiC has a lower defect density than 6H-SiC under current wafer fabrication technology [58]. Nonconductive 4H-SiC samples display charging effects on LEED and Auger before graphitization.  $H_2$  etching leaves a



non-conducting silicate layer on both Si-face and C-face surfaces [1] and the 4H-SiC bulk is nonconducting, therefore no LEED pattern can be observed on the 4H-SiC surfaces when the electron beam energy is below 100 eV. Once the E-beam energy is over a certain threshold value of approximately 110 eV, SiC  $\sqrt{3}\times\sqrt{3}$  R30° patterns similar to those on the Si-face can be observed. The threshold voltage depends on sample preparation and the LEED electron beam adjustments. The absence of charging effect at higher E-beam energies is probably a consequence of the secondary electron output balancing the incident electron current, which eliminates the charging effects [93]. Graphitized 4H-SiC samples do not show any charging effect, since the graphite film is conductive.

Without any further treatment in UHV, the furnace-graphitized C-face samples were studied at different graphite thicknesses (Fig. 5.1). The  $H_2$ -etched surface shows a SiC  $\sqrt{3}\times\sqrt{3}$  R30° LEED pattern (Fig. 5.1a). Similar to the Si-face samples, C-face samples also have 3-fold symmetry and diffuse background LEED features before graphitization, so we believe that after  $H_2$  etching, the surface of C-face SiC is also covered by a silicate monolayer, as proposed by Starke et al. [2]. For samples annealed in the furnace around 1250° C, graphite diffraction appears (Fig. 5.1b). Instead of graphite spots, the graphite diffraction on C-face generally shows graphite rings, which means that the graphite growth on C-face is azimuthally disordered [92]. However, the graphite film apparently has some preferential orientations, since the intensity of the graphite rings is not uniform and they are split at certain azimuths (Fig. 5.1). With the growth of thicker graphite films, the intensity of graphite diffraction rings become stronger and the intensity distribution around the ring also changes (Fig. 5.1c & d).

Another interesting phenomenon observed in these LEED patterns is that the SiC reconstruction patterns change from SiC  $\sqrt{3}\times\sqrt{3}$  R30° to SiC  $1\times 1$ , and then disappear when graphite films grow thick. Neither SiC  $6\sqrt{3}\times 6\sqrt{3}$  R30° reconstruction nor any double scattering LEED patterns appear at any phase. Therefore, either no interfacial layer exists between graphite and the SiC substrate or the interfacial layer is thin and disordered.

A SiC  $3\times 3$  reconstruction was observed in LEED after the UHV annealing of SiC C-face at 1150° C. A SiC  $3\times 3$  LEED pattern was also obtained on a RF furnace prepared

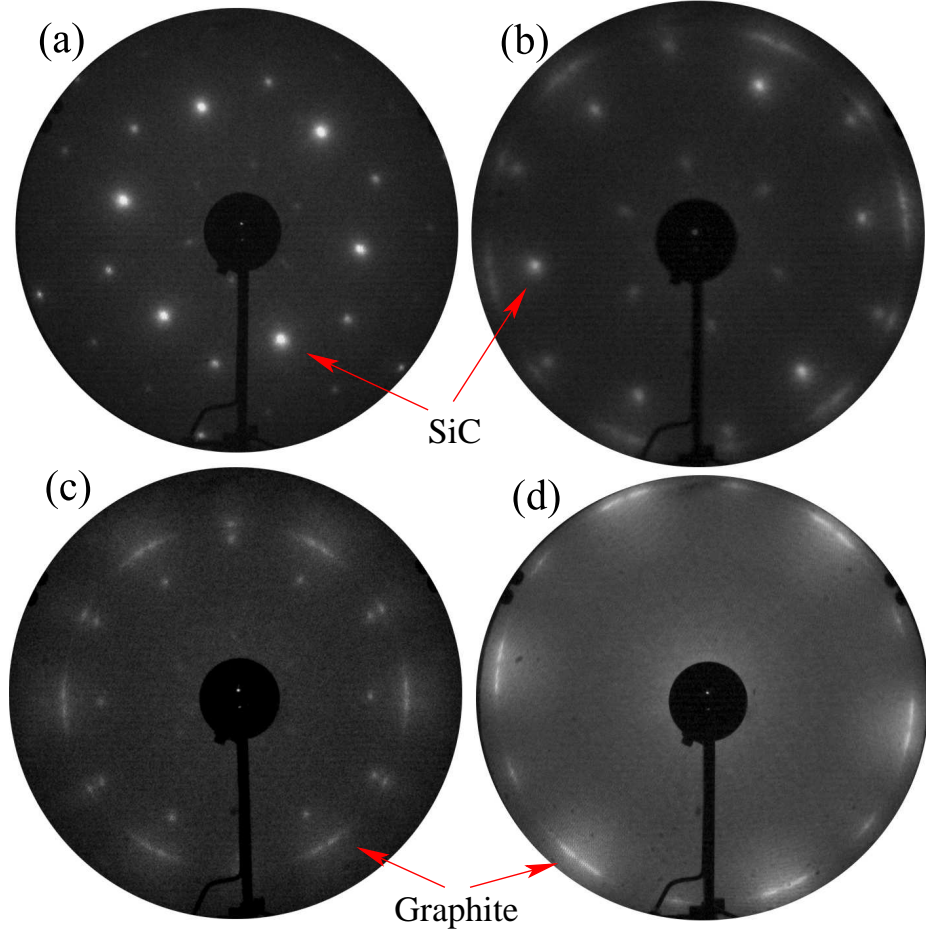


Figure 5.1: The evolution of the LEED patterns on SiC(000 $\bar{1}$ ) surface. (a) The LEED pattern after  $H_2$  etching shows SiC  $\sqrt{3}\times\sqrt{3}$  R30° reconstruction,  $E_p=118$  eV. Some LEED patterns before graphitization also show 3-fold symmetry and diffuse background on C-face. Charge effects are observed, when the electron beam energy is below a threshold value of 110 eV. (b) 1 to 2 graphene layers on SiC(000 $\bar{1}$ ) surface. Both graphite arcs and SiC  $\sqrt{3}\times\sqrt{3}$  R30° reconstruction spots are visible,  $E_p=73$  eV. Graphite arcs indicate that the initial growth of graphite is azimuthally disordered. (c) 3 to 4 layers of graphene on SiC (000 $\bar{1}$ ) surface. Only graphite rings with stronger intensity and SiC  $1\times 1$  spots are visible,  $E_p=103$  eV. (d) Thicker graphite films with more than 6 layers on SiC (000 $\bar{1}$ ) surface. Only graphite rings visible at this phase. The graphite ring is continuous but not uniform intensity. Bright arcs appears at certain azimuths along the graphite ring,  $E_p=69$  eV.

sample after peeling off thick graphite films on the C-face and heating it to 1150° C in UHV. Therefore, SiC  $3\times 3$  is a reconstruction forming on C-face when the annealing temperature is below the graphitization temperature.

### 5.3 *STM Results*

Graphite growth on C-face SiC has significant differences between samples prepared in UHV and those in the RF furnace. STM results show that the graphitization in UHV leaves a surface almost 100% covered by nanocaps. In contrast, the nanocap coverage on the C-face of SiC prepared in the RF furnace is less than 40%, and the remaining areas are very flat graphite films (Fig. 5.3b). The LEED patterns of UHV samples are broad weak graphite rings in contrast to the sharp LEED arcs from the RF furnace samples.

C-face STM images presented here are all taken on the two samples graphitized in the RF graphitization furnace. These two samples have different graphite film thicknesses. The same surface analysis procedures were conducted in the room temperature UHV STM system.

#### 5.3.1 **On Thick Graphite Films**

Auger spectroscopy shows no Si peak on the thick graphite film and the corresponding LEED patterns have no other diffraction pattern but graphite rings, which means that the graphite thickness is more than 6 layers. High resolution TEM experiments on another sample prepared under the same conditions show more than 15 graphite layers on the surface (Fig. 5.4) [10]. The interface structure between graphite and SiC in the TEM image seems disordered, however the TEM wafering process can change the interfacial layer. Graphite film were completely detached from the SiC substrate in TEM images taken on other cross-sections of the same sample. This TEM result shows a different growth mechanism than that found in the TEM results from Kusunoki et al.. Their TEM showed profile of nanocaps growth on the interface between graphite and SiC substrates [41].

Both AFM and STM images indicate that domains in micron size exist on the SiC(000 $\bar{1}$ ) surface after graphitization (Fig. 5.3a). The heights between domains vary from 2 nm to 5 nm, which is higher than the original height difference between terraces after  $H_2$  etching

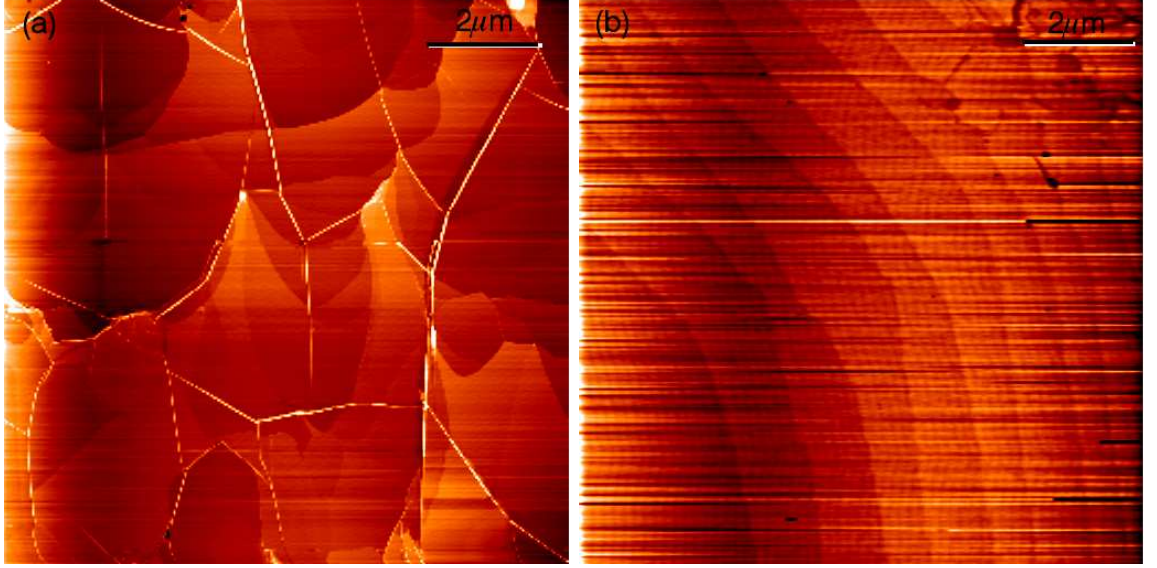


Figure 5.2: AFM images on graphite films growth on the C-face of SiC prepared in the RF furnace by Xuebin Li. (a) AFM on thick graphite films growth on SiC C-face. The surface has big domains in several micron size. The height between big domains vary from 2 nm to 5 nm. Big nanotubes are across the surface. (b) AFM on  $H_2$  etched surface the C-face of SiC. The height between adjacent terraces is around one unit cell height of 4H-SiC. The surface maintain the terraces after a thin graphite film growth process.

(Fig. 5.2). Large carbon nanotubes or scrolls, with diameters of up to 30 nm, are always formed on graphitized surfaces of C-face SiC. These carbon nanotubes occur either along step boundaries of the domains, or even nearly perpendicular to steps. In contrast, nanotubes are very rare on graphitized Si-face sample. We saw much smaller nanotubes only once on the Si-face of a 6H-SiC sample pre-prepared with the oxidation procedure same to the oxidation procedure for the NASA sample. The oxidation solution was used to flatten the surface before we developed the  $H_2$  etching method.

Smaller-scale STM scanning on the surface shows that the “flat” domains found by AFM are 40% covered by nanocaps (Fig. 5.3b). Nanocaps, as perhaps carbon onions, gather forming islands that scatter all over the surface. The remainder of the surface is very flat. Further atomic resolution scanning indicates that these flat regions are graphite (Fig. 5.5b). Under the nanocap islands, one often finds a 3 Å high layer (Fig. 5.5d), which is possibly a graphene sheet growing from underneath the nanocaps (however, we do not believe that this plays a dominant role in the growth of the graphite film).

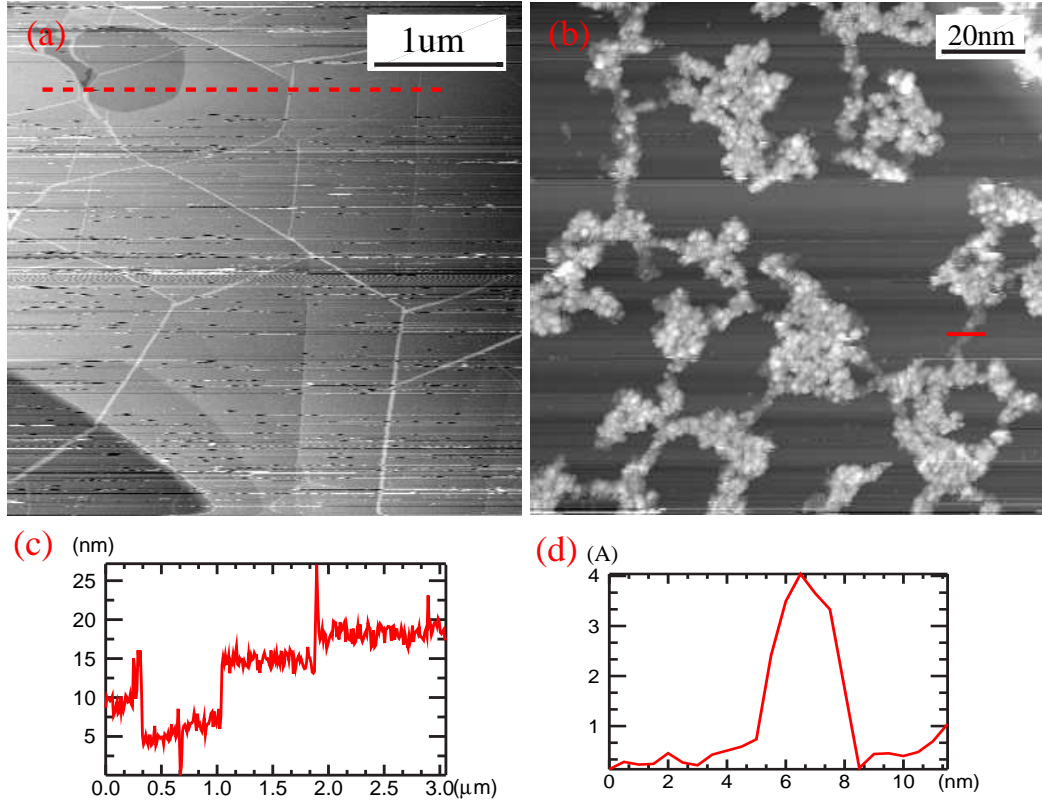


Figure 5.3: STM images on thick graphite films grown on the C-face of SiC. (a)  $4\ \mu\text{m}$  scan presents an overview on the surface showing domains of micron size. Large nanotubes cross the surface often forming the boundaries between domains. The tip voltage was  $-2.5\ \text{V}$  and the constant tunneling current was  $100\ \text{pA}$ . (b) Nanocaps and flat areas between nanocaps on a flat domain. The nanocaps coverage is less than 40%. The profile over the lowest part of the nanocaps show that they sit on graphene islands over the uniform flat graphite films underneath. The tip voltage was  $-3.0\ \text{V}$  and the constant tunneling current was  $100\ \text{pA}$ . (c) Profile over several domains (dashed line in (a)). (d) Profile across the lowest region of nanocaps show that the height is about one layer of graphene, which means nanocaps probably grow on graphene islands beneath nanocaps.



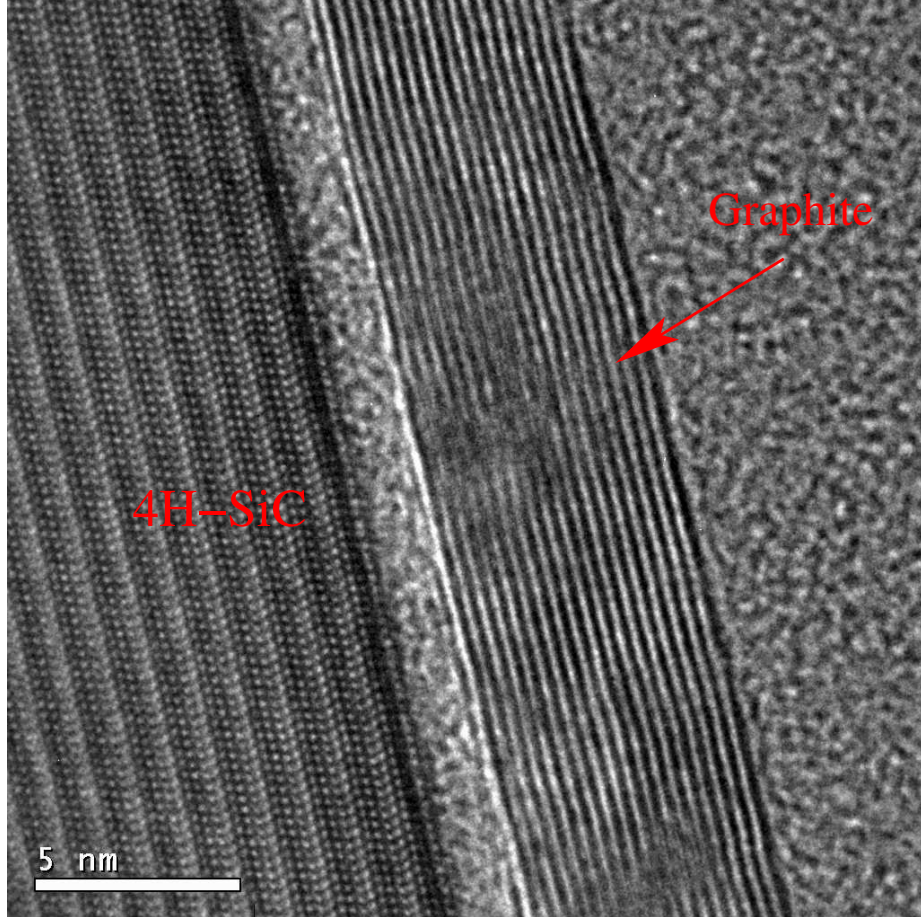


Figure 5.4: High resolution TEM cross-sectional on C-face graphitized 4H-SiC. Along the (0001) direction, the periodicities of 1 nm unit cell and 0.25 nm SiC bilayers are both discerned within the 4H-SiC. The graphite films in this picture have uniform thickness of around 20 sheets. However, the thickness is not uniform on the same sample, varying from 5 to 25 monolayers. The gap between the SiC substrate and graphite films is probably due to peeling during sample wafering, since the gap changes in different TEM scans. This figure is after Ref. [10]

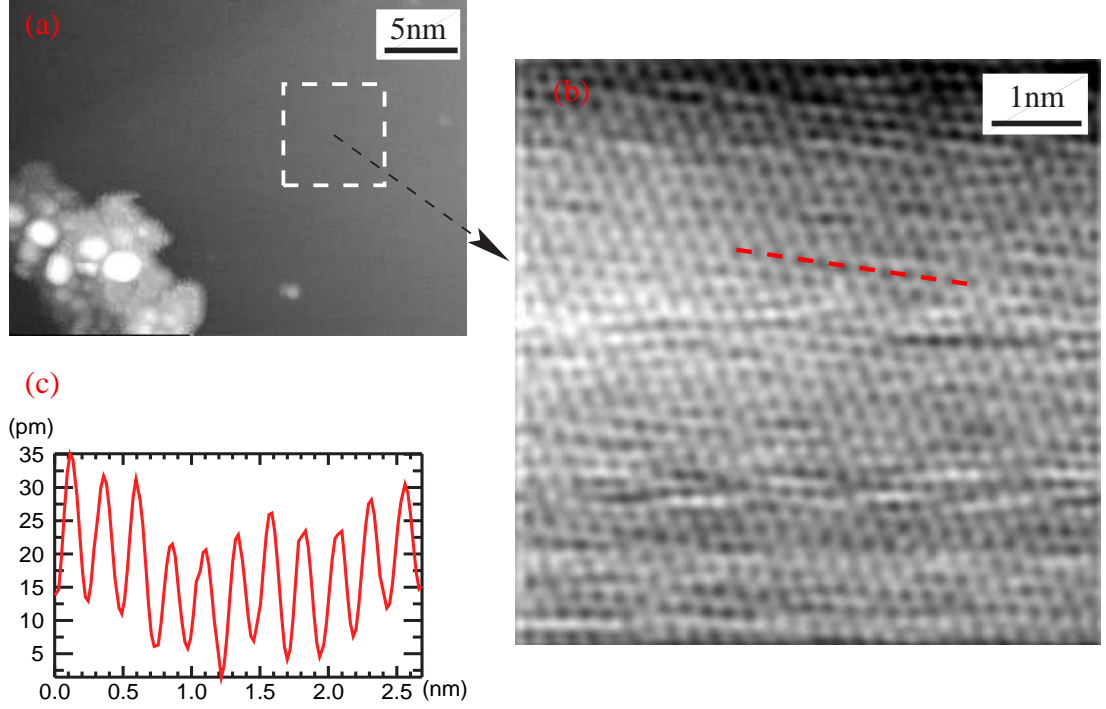


Figure 5.5: The flat region on SiC C-face surface is terminated with graphite films. (a) The STM image on a flat region with nanocaps on surface. The tip voltage was  $-3.0$  V and the constant tunneling current was  $100$  pA. (b) Atomic resolution scanning within the dashed square of the flat region. Graphite with honeycomb structure is discerned. The tip voltage was  $-1.6$  V and the constant tunneling current was  $100$  pA. The graphite films in one domain show ordered crystal structure, which means the azimuthal disorder seen in LEED should come from different domains or different graphite layers. (c) Profile on graphene films shows surface corrugation is only  $15$ - $20$  picometers.

Further atom-resolved STM images (Fig. 5.5) on a flat region between nanocap islands demonstrates that the flat regions are graphite films. At the high impedance used for this image, the STM resolves full honeycomb structure of the graphite. The top layer of the graphite film in one domain has ordered crystal structure, thus the azimuthal disorder observed in LEED should come from different domains or different graphite layers. It is more likely from different domains, since the azimuthal disorder also exists on thin graphite films (Fig. 5.1b).

### 5.3.2 On Thin Graphite Films

The thin graphite film was prepared in the RF furnace at  $1350^{\circ}\text{C}$ . The Si and C Auger peak ratio for the thin graphite film sample is  $1:12$ , which means the film is  $2$ - $3$  graphene

layers. The large-scale STM scan demonstrates similar results to AFM images on  $H_2$  etched surfaces. The graphitization mostly maintains the ordered terrace topology obtained from the  $H_2$  etching process (Fig. 5.6a). Comparing with the thick graphite film surface, this thin film graphitization has less modification of the original surface topology. The surface is also covered by nanocaps (Fig. 5.6b) and the coverage is similar to the thick graphitized sample. However, the number density of carbon nanotubes on surface is much smaller than the sample with the thick graphite film. Small-scale STM scans over flat regions between nanocaps resolved a disordered corrugation of graphite (Fig. 5.7a). The lateral scale of this surface undulation is 2–5 nm.



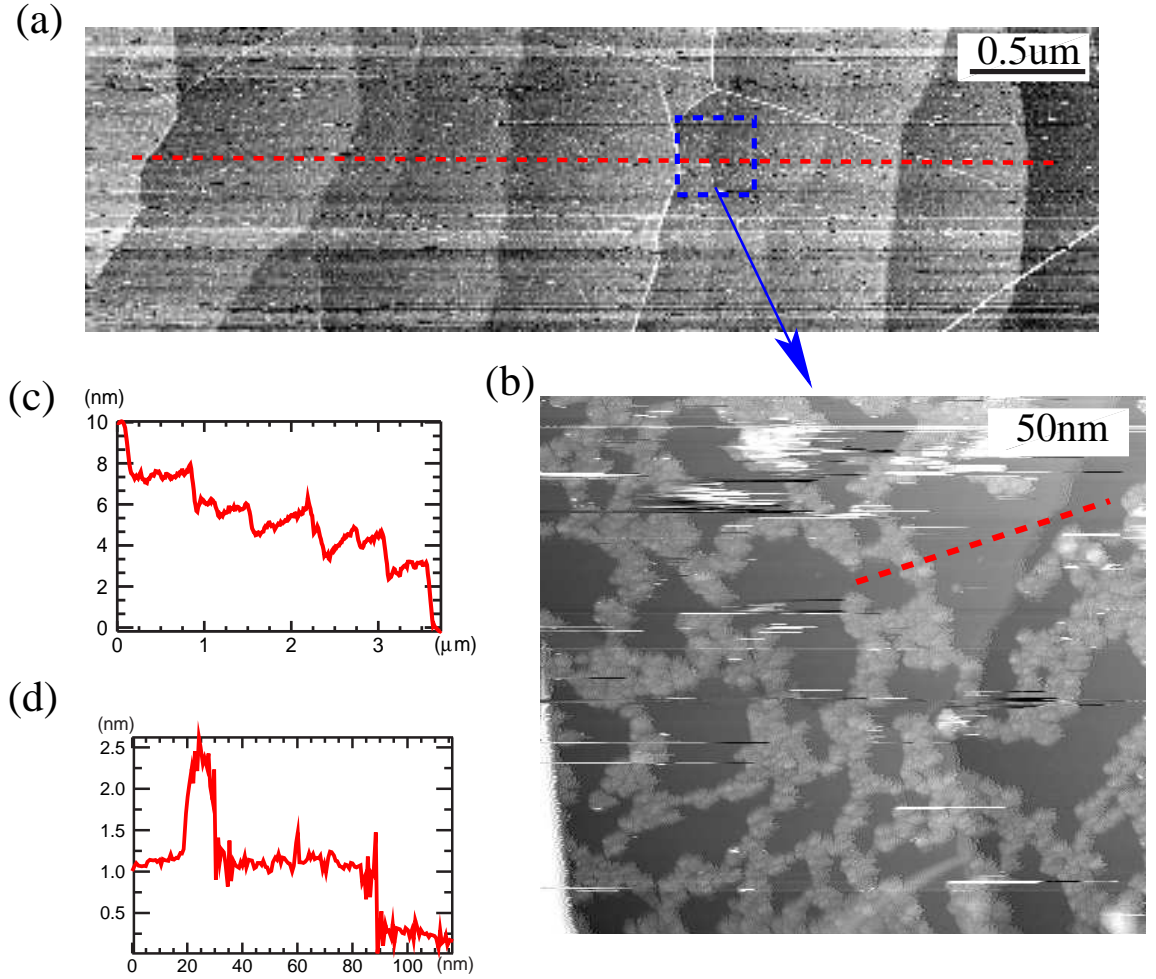


Figure 5.6: STM images on thin graphite films grown on SiC C-face. (a) An overview of the surface shows that after the thin film graphitization process, the surface maintains the oriented terraces forming in the  $H_2$  etching process. Big nanotubes also appear on the surface, but the number density of nanotubes is much smaller than the thicker films. The tip voltage was  $-4.0$  V and the constant tunneling current was 50 pA. (b) The surface is also covered by nanocap islands. The nanocap coverage is nearly the same to the thick graphitized surface. The tip voltage was  $-4.5$  V and the constant tunneling current was 100 pA. (c) Profile from (a) shows that the terrace height is 1 nm or 2 nm. (d) Profile from (b) indicate that the height of nanocaps is around 1–1.5 nm and the terrace height is 1 nm.

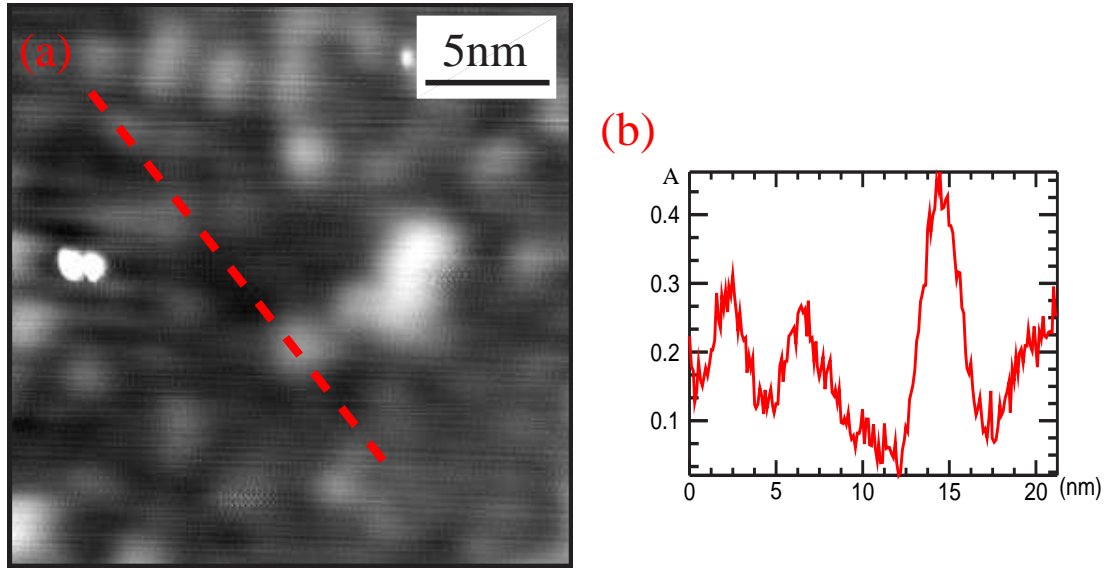


Figure 5.7: STM image and its profile on the thin graphite film grown on the C-face of SiC. (a) STM scan on the flat region between the nanocaps. The structure is either a disordered structure underneath graphite film or the corrugation of graphite film itself. The tip voltage was  $-2.5$  V and the constant tunneling current was 50 pA. (b) The profile shows that the surface vertical undulation is within half an angstrom and the lateral spacing is from 2 nm to 5 nm.

## CHAPTER VI

### CONCLUSION

#### *6.1 Summary of Results*

This thesis presented my research on the graphite/SiC system with the ultra high vacuum surface analysis techniques. Ultrathin graphite films were grown epitaxially on the silicon-terminated faces of 6H-SiC and 4H-SiC samples via thermal desorption of silicon at annealing temperature from 1200° C to 1550° C in the UHV chamber. The thickness of graphite was controlled through monitoring annealing temperature and time in UHV. The thickness of graphite films was measured by quantitatively modeling the ratio of Si and C Auger peaks.

The evolution of LEED patterns and AES spectra provide sufficient evidences that ultrathin graphite films grow epitaxially on the SiC(0001) surface. The sharp graphite LEED diffraction spots indicate that the graphite films registry on SiC(0001) surface have a 30° rotation relative to the substrate lattice. The clear SiC  $6\sqrt{3}\times 6\sqrt{3}$  R30° LEED patterns obtained during the surface evolution provide thorough records for analyzing the mechanism of the initial graphene layer growth of on the SiC(0001) surface.

STM results for 3-4 ML graphite films on the SiC(0001) surface indicate that the graphite films on the surface are divided into domains around 50 nm<sup>2</sup> size. The heights between adjacent domains vary from 0.5 Å up to 3.5 Å. These heights correspond to the distance between Si and C layers within one SiC bilayer and the distance between two adjacent graphene layers. STM resolved both hexagon and honeycomb atomic structures on graphite films. The graphite films have surface corrugation that follow  $6a_{SiC} \times 6a_{SiC}$  lateral period and 0.2 Å to 0.3 Å vertical amplitudes. The corresponding STS spectra and recent LT-STM results from NIST prove that graphite films are often continuous over steps on the surface.

STM on mono-layer graphene on the SiC(0001) surface resolves the interfacial structure between the SiC substrate and the first graphene layer, with tunneling dominated by states

originating on the layer beneath the graphene. According to the  $\sqrt{3}\times\sqrt{3}\text{R}30^\circ$  extinction phenomenon due to the equal occupation of the 3  $\sqrt{3}\times\sqrt{3}\text{R}30^\circ$  sublattices and the actual atom locations in the Fourier filtered STM image, we construct a possible SiC  $6\sqrt{3}\times 6\sqrt{3}\text{R}30^\circ$  unit cell to explain the major ordered features of the interfacial layer. The structure factor of this proposed unit cell explains the extinction of the  $\sqrt{3}\times\sqrt{3}\text{R}30^\circ$  LEED spots and partially solves the controversy regarding interpretations of the SiC  $6\sqrt{3}\times 6\sqrt{3}\text{R}30^\circ$  LEED patterns. We also propose the model of  $6\times 6$  surface corrugation of graphite according to the simulated kinematic scattering results. We conclude that the  $6\sqrt{3}\times 6\sqrt{3}\text{R}30^\circ$  LEED pattern can be explained predominantly by kinematic scattering from the  $6\sqrt{3}\times 6\sqrt{3}\text{R}30^\circ$  reconstruction, the slightly corrugated graphene, and the SiC substrate. The SiC  $6\times 6$  satellite LEED spots around primary graphite spots when graphite films are thick should be only due to the SiC  $6\times 6$  corrugation of the graphite films.

STM on the graphitized vicinal samples demonstrates that the graphite film with  $6\times 6$  corrugation can be obtained on terraces by the typical graphitization process in UHV. However, the terrace edges are not parallel, so the edge direction of graphite ribbons has not been controlled. The graphite appears to be continuous over the terrace edges.

LEED results give evidence of the successful removal of graphite film by the electron-beam lithography method. STM on patterned graphite ribbons shows that the designed graphite ribbon pattern is present even after removing the HSQ resist. Nanocaps from HSQ residue spread to cover most of the surface after the sample was heated to  $500^\circ\text{C}$ . STM on a flat ribbon area underneath the HSQ shows graphite-featured  $6\times 6$  corrugation and STM resolved SiC  $6\sqrt{3}\times 6\sqrt{3}\text{R}30^\circ$  interfacial layer structure on another flat area.

UHV graphitization on C-face SiC results in carbon nanocap growth on all surfaces. While the nanocap coverage on C-face SiC samples prepared in the RF furnace is around 40% on both thick (over 6 graphene layer) and thin (2-3 graphene layer) graphite films, for the thick graphite film sample, the remaining area consists of very flat graphite films with only 15-20 picometers atomic corrugation. The surfaces have micron size domains and the height between adjacent domains are around 2 nm to 5 nm. Many large nanotubes or scrolls appear on the surface forming the boundaries of domains or lying within the large

domain. For the thin graphite film sample, STM on the flat area showed disordered surface structure with vertical undulation of less than 1/2 angstrom and lateral spacing from 2 nm to 5 nm. Compared with the thick graphite film surface, the thin graphite film growth has less modification to the original SiC surface topology, mostly maintaining the ordered terrace topology obtained from the  $H_2$  etching process.

## ***6.2 Suggested Future Work***

In order to improve graphite film quality growth on SiC surfaces, more graphite growth methods should be attempted on both faces of SiC. The first improvement should be mounting a Si evaporator to deposit Si on the surface so that the Si loss rate during the graphitization process can be better controlled.

More  $H_2$  etching and graphitization experiments need to be conducted on the vicinal SiC samples to produce more ordered terrace edges. A method of isolating graphite films on the edges of vicinal samples into independent graphite ribbons needs to be developed.

The HSQ resist left after E-beam lithography needs to be removed more carefully with the HF solvent so that no HSQ residue remains on top of the graphite ribbons. The optical part and the coarse motion of the sample in the room temperature UHV STM system need to be improved so that micron size lithographically-defined features on sample surfaces can be easily discerned and approached and positioned under the STM tips.

As proposed in Chapter 3, the kinematic scattering simulation can be improved by adding more considerations to the Matlab code to reproduce more diffraction spots appearing on the SiC  $6\sqrt{3} \times 6\sqrt{3}$  R30° LEED pattern.

## Bibliography

- [1] U. Starke, J. Bernhardt, J. Schardt, K. Heinz, SiC surface reconstruction: Relevancy of atomic structure for growth technology, *Surface Review and Letters* 6 (6) (1999) 1129–1141.
- [2] U. Starke, J. Schardt, J. Bernhardt, M. Franke, K. Reuter, H. Wedler, K. Heinz, J. Furthmüller, P. Käckell, F. Bechstedt, Novel reconstruction mechanism for dangling-bond minimization: Combined method surface structure determination of SiC(111)-(3 × 3), *Phys. Rev. Lett.* 80 (4) (1998) 758–761.
- [3] Image from internet.  
URL <http://www.inovacaotecnologica.com.br/>.
- [4] K. S. Novoselov, A. K. Geim, S. V. Morozov, D. Jiang, M. I. Katsnelson, I. V. Grigorieva, S. V. Dubonos, A. A. Firsov, Two-dimensional gas of massless dirac fermions in graphene, *Nature* 438 (7065) (2005) 197–200.  
URL <http://dx.doi.org/10.1038/nature04233>
- [5] Princeton research instruments, <http://www.prileeduhv.com/leed.html> (2006).
- [6] M. P. Seah, W. A. Dench, This is a compliation of experiemntal data determined for a large variety of materials and electron energies, *Surf. Interf. Anal.* 1.
- [7] A. M. Ezpeleta, Electronic Structure of Low-Dimentional System Analyzed by Angle-Resolved Photoemission Spectroscopy, Ph.D. thesis, Donostia (2002).
- [8] W. Ranke, Auger Electron Spectroscopy (AES) and Modulation Techniques.  
URL <http://w3.rz-berlin.mpg.de/~jentoft/lehre>
- [9] X. Xie, N. Yakolev, K. Loh, Distinguishing the H3 and T4 silicon adatom model on 6H-SiC(0001)  $\sqrt{3} \times \sqrt{3}R30^\circ$  reconstruction by dynamic rocking beam approach, *J. Chem. Phys.* 330 (2003) L639–L645.
- [10] D. Ugarte, J. Benitti, (to be published).
- [11] C. Berger, Z. Song, T. B. Li, X. Li, A. Y. Ogbazghi, R. Feng, Z. Dai, A. N. Marchenkov, E. H. Conrad, P. N. First, W. A. de Heer., Ultrathin epitaxial graphite: 2D electron gas properties and a route toward graphene-based nanoelectronics, *J. Phys. Chem. B* 108 (2004) 19912–19916.
- [12] S. Tans, R. Verschueren, C. Dekker, Room temperature transistor based on a single carbon nanotube, *Nature* 393 (6680) (1998) 49–52.
- [13] R. Martel, T. Schmidt, H. R. Shea, T. Hertel, P. Avouris, Single- and multi-wall carbon nanotube field-effect transistors, *Appl. Phys. Lett.* 73 (17) (1998) 2447–2449.
- [14] K. S. Novoselov, A. K. Geim, S. V. Morozov, D. Jiang, Y. Zhang, S. V. Dubonos, I. V. Grigorieva, A. A. Firsov, Electric field effect in atomically thin carbon films, *Science* 306 (5696) (2004) 666–669.  
URL <http://www.sciencemag.org/cgi/content/abstract/306/5696/666>

- [15] Y. Zhang, J. P. Small, W. V. Pontius, P. Kim, Fabrication and electric-field-dependent transport measurements of mesoscopic graphite devices, *Appl. Phys. Lett.* 86 (7) (2005) 073104.  
URL <http://link.aip.org/link/?APL/86/073104/1>
- [16] K. Nakada, M. Fujita, G. Dresselhaus, M. S. Dresselhaus, Edge state in graphene ribbons: Nanometer size effect and edge shape dependence, *Phys. Rev. B* 54 (24) (1996) 17954–17961.
- [17] K. Wakabayashi, Electronic transport properties of nanographite ribbon junctions, *Phys. Rev. B* 64 (2001) 125428.
- [18] Y. Zhang, Y.-W. Tan, H. L. Stormer, P. Kim, Experimental observation of the quantum hall effect and berry’s phase in graphene, *Nature* 438 (7065) (2005) 201–204.  
URL <http://dx.doi.org/10.1038/nature04235>
- [19] C. Berger, Z. Song, X. Li, X. Wu, N. Brown, C. Naud, D. Mayou, T. Li, J. Hass, A. N. Marchenkov, E. H. Conrad, P. N. First, W. A. de Heer, Electronic confinement and coherence in patterned epitaxial graphene, *Science* 312 (5777) (2006) 1191–1196.  
URL <http://www.sciencemag.org/cgi/content/abstract/312/5777/1191>
- [20] A. A. Stephen E. Saddow, *Advances in Silicon Carbide Processing and Applications*, Artech House, Inc., 2004.
- [21] Sakurai, *Advances in Scanning Probe Microscopy*, Springer, 2000.
- [22] Y. M. Tairov, V. F. Tsvetkov, Investigation of growth processes of ingots of silicon-carbide single-crystals, *Journal of Crystal Growth* 43 (2) (1978) 209–212.
- [23] Cree Inc., [www.cree.com](http://www.cree.com) (2004).
- [24] A. Ellison, J. Zhang, W. Magnusson, A. Henry, Q. Wahab, J. P. Bergman, C. Hemmingsson, N. T. Son, E. Janzen, Fast SiC epitaxial growth in a chimney CVD reactor and HTCVD crystal growth developments, *Silicon Carbide and Related Material* 1999, Pts. 1 & 2 338-3 (2000) 131–136.
- [25] Y. Taniyasu, M. Kasu, T. Makimoto, An aluminium nitride light-emitting diode with a wavelength of 210 nanometres, *Nature* 441 (7091) (2006) 325–328.
- [26] M. Bhatnagar, B. J. Baliga, Comparison of 6H-SiC, 3C-SiC, and Si for power devices, *IEEE Transactions on Electron Devices* 40 (3) (1993) 645–655.
- [27] H. O. Pierson, *Handbook of Carbon, Graphite, Diamond, and Fullerenes*, Noyes, 1993.
- [28] D. D. L. Chung, Review graphite, *Journal of Material Science* 37 (8) (2002) 1475–1489.
- [29] F. Atamny, A. Baiker, Investigation of carbon-based catalysts by scanning tunneling microscopy: Opportunities and limitations, *Applied Catalysis A-General* 173 (2) (1998) 201–230.
- [30] P. R. Wallace, The band theory of graphite, *Physical Review* 71 (9) (1947) 622–634.

- [31] B. Partoens, F. M. Peeters, From graphene to graphite: Electronic structure around the k point, *Phys. Rev. B* 74 (7) (2006) 075404.  
URL <http://link.aps.org/abstract/PRB/v74/e075404>
- [32] K. S. Novoselov, A. K. Geim, S. V. Morozov, D. Jiang, Y. Zhang, S. V. Dubonos, I. V. Grigorieva, A. A. Firsov, Electric field effect in atomically thin carbon films, *Science* 306 (2004) 666–669.
- [33] Y. B. Zhang, Y. Tan, H. Stormer, P. Kim, Experimental observation of quantum hall effect and Berry’s phase in graphene, *Nature* 438 (2005) 201–204.
- [34] K. S. Novoselov, A. Geim, S. Morozov, D. Jiang, M. I. Katsnelson, S. V. Dubonos, A. A. Firsov, Two-dimensional gas of massless Dirac fermions in graphene, *Nature* 438 (2005) 197–200.
- [35] N. W. Ashcroft, N. D. Mermin, *Solid State Physics*, Thomson Learning, Inc., 1976.
- [36] P. L. Taylor, O. Heinonen, *A Quantum Approach to Condensed Matter Physics*, Cambridge, 2002.
- [37] A. Van Bommel, J. Crombeen, A. Van Tooren, LEED and Auger electron observations of the SiC(0001) surface, *Surf. Sci.* 48 (1975) 463–472.
- [38] F. Owman, P. Martensson, STM study of the SiC(0001)  $\sqrt{3} \times \sqrt{3}$  surface, *Surf. Sci.* 330 (1995) L639–L645.
- [39] I. Forbeaux, J. M. Themlin, J. M. Debever, Heteroepitaxial graphite on 6H-SiC(0001): Interface formation through conduction-band electronic structure, *Phys. Rev. B* 58 (24) (1998) 16396–16406.
- [40] B. An, S. Fukuyama, K. Yokogawa, Graphitization of 6H-SiC(000 $\bar{1}$ ) surface by scanning tunneling microscopy, *Japanese Journal of Applied Physics part 1-regular papers short note & review papers* 41 (7B) (2002) 4890–4893.
- [41] M. Kusunoki, T. Suzuki, T. Hirayama, N. Shibata, K. Kaneko, A formation mechanism of carbon nanotube films on SiC(0001), *Appl. Phys. Lett.* 77 (4) (2000) 531–533.
- [42] V. Derycke, R. Martel, M. Radosavljevic, F. M. R. Ross, P. Avouris, Catalyst-free growth of ordered single-walled carbon nanotube networks, *Nano Letters* 2 (10) (2002) 1043–1046.
- [43] T. Maruyama, H. J. Bang, Y. Kawamura, N. Fujita, K. Tanioku, T. Shiraiwa, Y. Hozumi, S. Naritsuka, M. Kusunoki, Scanning-tunneling-microscopy of the formation of carbon nanocaps on SiC(000 $\bar{1}$ ), *Chemical Physics Letters* 423 (4-6) (2006) 317–320.
- [44] P. E. Quesenberry, P. N. First, Statistics of 3D island growth for a reactive interface: Ni/GaAs(110), *Phys. Rev. B* 54 (1996) 8218–8230.
- [45] G. Ertl, J. Kupperts, *Low Energy Electrons and Surface Chemistry*, VCH Publishers, 1985.
- [46] A. Zangwill, *Physics at Surfaces*, Cambridge, 1988.



- [47] L. V. D. Leemput, H. V. Kempen, Scanning tunnelling microscopy, Report of Progress Physics 55 (1992) 1165–1240.
- [48] J. G. Simmons, Generalized formula for electric tunnel effect between similar electrodes separated by a thin insulating film, J. Appl. Phys. 34 (6) (1963) 1793–1803.
- [49] J. Tersoff, D. R. Hamann, Theory of the scanning tunneling microscope, Phys. Rev. B 31 (2) (1985) 805–813.
- [50] N. D. Lang, Spectroscopy of single atoms in the scanning tunneling microscope, Phys. Rev. B 34 (8) (1986) 5947–5950.
- [51] R. Celotta, T. Lucatorto, Scanning Tunneling Microscopy, Academic Press, INC., 1994.
- [52] P. E. Quesenberry, Scanning tunneling microscopy studies of a reactive interface: Ni/GaAs, Ph.D. thesis, Georgia Institute of Technology (1996).
- [53] OPA128LM from Burr-Brown, Inc., Tucson, AZ, 85706. 100 M $\Omega$  feedback resistor from Dale, Inc., Bradford, PA.
- [54] Burleigh Instruments, Inc., Fishers, NY 14453.
- [55] C. Bai, Scanning Tunneling Microscopy and Its Applications, Springer, 2000.
- [56] G. Rutter, et al. (unpublished).
- [57] NASA Glenn Research Center. <http://www.grc.nasa.gov/www/sic/index.html> (2006).
- [58] Z. C. Feng, SiC Power Materials, Springer, 2004.
- [59] J. A. Powell, P. G. Neudeck, A. J. Trunek, G. M. Beheim, L. G. Matus, R. W. Hoffman, L. J. Keys, Growth of step-free surfaces on device-size (0001)SiC mesas, Appl. Phys. Lett. 77 (10) (2000) 1449–1451.
- [60] P. G. Neudeck, J. A. Powell, G. M. Beheim, E. L. Benavage, P. B. Abel, A. J. Trunek, D. J. Spry, M. Dudley, W. M. Vetter, Enlargement of step-free SiC surfaces by homoepitaxial web growth of thin SiC cantilevers, J. Appl. Phys. 92 (5) (2002) 2391–2400.
- [61] F. Owman, P. Martensson, The SiC  $6\sqrt{3} \times 6\sqrt{3}$  reconstruction studied with STM and LEED, Surf. Sci. 369 (1-3) (1996) 126–136.
- [62] X. N. Xie, H. Q. Wang, A. T. S. Wee, K. P. Loh, The evolution of  $3 \times 3$ ,  $6 \times 6$ ,  $\sqrt{3} \times \sqrt{3}R30^\circ$  and  $6\sqrt{3} \times 6\sqrt{3}R30^\circ$  superstructures on 6H-SiC(0001) surfaces studied by reflection high energy electron diffraction, Surf. Sci. 478 (1-2) (2001) 57–71.
- [63] R. Kaplan, Surface-structure and composition of  $\beta$  - SiC and 6H-SiC, Surf. Sci. 215 (1-2) (1989) 111–134.
- [64] L. Li, I. S. T. Tsong, Atomic structures of 6H-SiC(0001) and (000 $\bar{1}$ ) surfaces, Surf. Sci. 351 (1-3) (1996) 141–148.

- [65] M. Naitoh, J. Takami, S. Nishigaki, N. Toyama, A  $(2\sqrt{3} \times 2\sqrt{13})$  surface phase in the 6H-SiC(0001) surface studied by scanning tunneling microscopy, Appl. Phys. Lett. 75 (17) (1999) 2692–2692.
- [66] M. A. Kulakov, G. Henn, B. Bullemer, SiC(0001)  $3 \times 3$ -Si surface reconstruction - A new insight with a STM, Surf. Sci. 346 (1-3) (1996) 49–54.
- [67] J. E. Northrup, J. Neugebauer, Theory of the adatom-induced reconstruction of the SiC(0001) $\sqrt{3} \times \sqrt{3}$  surface, Phys. Rev. B 52 (24) (1995) 17001–17004.
- [68] A. Coati, M. Sauvage-Simkin, Y. Garreau, R. Pinchaux, T. Argunova, K. Aid,  $(\sqrt{3} \times \sqrt{3}R30^\circ)$  reconstruction of the 6H-SiC(0001) surface: A simple T4 Si adatom structure solved by grazing-incidence x-ray diffraction, Phys. Rev. B 59 (19) (1999) 12224–12227.
- [69] V. Ramachandran, R. M. Feenstra, Scanning tunneling spectroscopy of Mott-Hubbard states on the 6H-SiC(0001)  $\sqrt{3} \times \sqrt{3}$  surface, Phys. Rev. Lett. 82 (5) (1999) 1000–1003.
- [70] M. H. Tsai, C. S. Chang, J. D. Dow, I. S. T. Tsong, Electronic contributions to scanning-tunneling-microscopy images of an annealed  $\beta$ -SiC(111) surface, Phys. Rev. B 45 (3) (1992) 1327–1332.
- [71] A. Charrier, A. Coati, T. Argunova, F. Thibaudau, Y. Garreau, R. Pinchaux, I. Forbeaux, J. M. Debever, M. Sauvage-Simkin, J. M. Themlin, Solid-state decomposition of silicon carbide for growing ultra-thin heteroepitaxial graphite films, J. Appl. Phys. 92 (5) (2002) 2479–2484.
- [72] W. Chen, H. Xu, L. Liu, X. Y. Gao, D. C. Qi, G. W. Peng, S. C. Tan, Y. P. Feng, K. P. Loh, A. T. S. Wee, Atomic structure of the 6H-SiC(0001) nanomesh, Surf. Sci. 596 (1-3) (2005) 176–186.
- [73] L. Simon, J. L. Bischoff, L. Kubler, X-ray photoelectron characterization of 6H-SiC (0001), Phys. Rev. B 60 (16) (1999) 11653–11660.
- [74] S. Tanuma, C. Powell, D. Penn, Calculation of electron inelastic mean free paths ii. data for 27 elements over the 50-2000 eV range, Surf. Interface Anal. 17 (1991) 911–926.
- [75] S. Tanuma, C. Powell, D. Penn, Calculations of electron inelastic mean free paths iii. data for 15 inorganic compounds over the 50-2000eV range, Surf. Interface Anal. 17 (1991) 927–939.
- [76] C. Powell, A. Jablonskib, I. Tilinin, S. Tanuma, D. R. Penn, Surface sensitivity of Auger-electron spectroscopy and X-ray photoelectron spectroscopy, Journal of Electron Spectroscopy and Related Phenomena 98-99 (1999) 1–15.
- [77] D. Tomanek, S. G. Louie, H. J. Mamin, D. W. Abraham, R. E. Thomson, E. Ganz, J. Clarke, Theory and observation of highly asymmetric atomic-structure in scanning-tunneling-microscopy images of graphite, Phys. Rev. B 35 (14) (1987) 7790–7793.
- [78] J. Xhie, K. Sattler, M. Ge, N. Venkateswaran, Giant and supergiant lattices on graphite, Phys. Rev. B 47 (23) (1993) 15835–15841.

- [79] J. Tersoff, Anomalous corrugations in scanning tunneling microscopy imaging of individual states, *Phys. Rev. Lett.* 57 (4) (1986) 440–443.
- [80] M. Enachescu, D. Schleef, D. F. Ogletree, M. Salmeron, Integration of point-contact microscopy and atomic-force microscopy: Application to characterization of graphite/Pt(111), *Phys. Rev. B* 60 (24) (1999) 16913–16919.
- [81] E. Bauer, Multiple scattering versus superstructures in low energy electron diffraction, *Surf. Sci.* 7 (1967) 351–364.
- [82] M. A. van Hove, W. H. Weinberg, C.-M. Chan, *Low-Energy Electron Diffraction*, Springer, Berlin, 1986.
- [83] C. S. Chang, I. S. T. Tsong, Scanning tunneling microscopy and spectroscopy of cubic  $\beta$ -SiC(111) surfaces, *Science* 306 (2004) 666–669.
- [84] M. Hornvonnhoegen, M. Pook, A. Alfalou, B. Muller, M. Henzler, The interplay of surface morphology and strain relief in surfactant mediated growth of Ge on Si(111), *Surf. Sci.* 284 (1993) 53–66.
- [85] N. M. R. Peres, A. H. C. Neto, F. Guinea, Conductance quantization in mesoscopic graphene, *Physical Review B (Condensed Matter and Materials Physics)* 73 (19) (2006) 195411.  
URL <http://link.aps.org/abstract/PRB/v73/e195411>
- [86] T. Seyller, K. Emtsev, K. Gao, F. Speck, L. Ley, A. Tadich, L. Broekman, J. Riley, R. Leckey, O. Rader, Structural and electronic properties of graphite layers grown on SiC(0001), *Surface Science* In Press, Corrected Proof.  
URL <http://www.sciencedirect.com/science/article/B6TVX-4K0FDMR-1/2/46cc05bf119a80b909e1ce0409a9144a>
- [87] Z. Song, Fabrication and characterization of nanopatterned epitaxial graphene films for carbon based electronics, Ph.D. thesis, Georgia Institute of Technology (2006).
- [88] C. C. Yang, W. C. Chen, The structures and properties of hydrogen silsesquioxane (HSQ) films produced by thermal curing, *Journal of Materials Chemistry* 12 (4) (2002) 1138–1141.
- [89] H. Namatsu, Y. Takahashi, K. Yamazaki, T. Yamaguchi, M. Nagase, K. Kurihara, Three-dimensional siloxane resist for the formation of nanopatterns with minimum linewidth fluctuations, *Journal of Vacuum Science & Technology B* 16 (1) (1998) 69–76.
- [90] A. Golz, G. Horstmann, E. S. von Kamienski, H. Kurz, Oxidation kinetics of 3C, 4H, and 6H silicon carbide, *Silicon Carbide and Related Materials* 1995 142 (1996) 633–636.
- [91] J. Hass, R. Feng, T. Li, X. Li, Z. Zong, W. A. de Heer, P. N. First, E. H. Conrad, C. A. Jeffrey, C. Berger, Highly ordered graphene for two dimensional electronics, *Appl. Phys. Lett.* 89 (14) (2006) 143106.

- [92] I. Forbeaux, J. M. Themlin, A. Charrier, F. Thibaudau, J. M. Debever, Solid-state graphitization mechanisms of silicon carbide 6H-SiC polar faces, *Appl. Surf. Sci.* 162 (2000) 406–412.
- [93] M. Thompson, M. D. Baker, *Auger Electron Spectroscopy*, John Wiley & Sons, 1984.
- [94] T. Aoyama, Y. J. Han, A. Ichimiya, Y. Hisada, S. Mukainakano, Structural analysis of 6H-SiC (0001) surface by RHEED rocking curves, *Surf. Sci.* 493 (1-3) (2001) 246–252.
- [95] T. Aoyama, Y. Hisada, S. Mukainakano, A. Ichimiya, Adsorbate effects of the surface structure of 6H-SiC(0001)  $\sqrt{3} \times \sqrt{3}$ R30° degrees, *Silicon Carbide and Related Materials 2001 Pts. 1 and 2, Proceedings 389-3* (2002) 705–708.
- [96] R. R. Haering, P. R. Wallace, The electric and magnetic properties of graphite, *Journal of Physics and Chemistry of Solid* 3 (3-4) (1957) 253–274.
- [97] Y. J. Han, T. Aoyama, A. Ichimiya, Y. Hisada, S. Mukainakano, The  $(\sqrt{3} \times \sqrt{3})$ R30 degrees reconstruction on hexagonal 6H-SiC(0001) surface with and without a Si flux, *Surf. Sci.* 493 (1-3) (2001) 238–245.
- [98] H. Kempa, P. Esquinazi, Y. Kopelevich, Integer quantum hall effect in graphite, *Solid state communications* 138 (3) (2006) 118–122.
- [99] L. Li, Y. Hasegawa, T. Sakurai, I. S. T. Tsong, Field-ion scanning tunneling microscopy study of the atomic structure of 6H-SiC(0001) surfaces cleaned by in situ Si molecular beam etching, *J. Appl. Phys.* 80 (4) (1996) 2524–2526.
- [100] M. Naitoh, M. Kitada, S. Nishigaki, N. Toyama, F. Shoji, An STM observation of the initial process of graphitization at the 6H-SiC(000 $\bar{1}$ ) surface, *Surface Review and Letters* 10 (2-3) (2003) 473–477.
- [101] L. E. Davis et al., *Handbook of Auger Electron Spectroscopy*, Physical Electronics, Eden Prairie, (2nd Ed.) 1976.

## VITA

Tianbo Li was born on January 21st 1976 in Shanghai, China. He grew up in the city of YinKou of LiaoNing Province in China. He was accepted by Tsinghua University in 1994 as a recommended student due to the excellent records at YinKou High School. He spent his first four years at Tsinghua in completing undergraduate education at School of Physics and obtained his Bachelor's in July 1998. He initialed his experimental physics research at Dr. Bisong Cao's Superconductivity Lab of Tsinghua since the early of 1998 and continued working there for three and half years on the application of YBCO films in microwave microstrip filters until he got his Master's in July 2001. He got married to Haiying Cao on May 8, 2001 in Beijing. He Moved to Atlanta, Georgia and began to pursue his PhD degree in school of physics at Georgia Institute of Technology since August 2001. He joined Dr. Phillip First's Scanning Tunneling Microscopy Lab in January 2002. His PhD research has been focusing on the characterization of ultrathin epitaxial graphite films on silicon carbide. He was awarded Nanoscience and Technology Graduate Fellowship of Georgia Tech in 2005. After graduation, he will take the position of Senior Design Engineer in Device Physics Group at Spansion Inc..